WING PLANFORM OPTIMIZATION VIA AN ADJOINT METHOD

A DISSERTATION
SUBMITTED TO THE DEPARTMENT OF AERONAUTICS AND ASTRONAUTICS
AND THE COMMITTEE ON GRADUATE STUDIES
OF STANFORD UNIVERSITY
IN PARTIAL FULFILLMENT OF THE REQUIREMENTS
FOR THE DEGREE OF
DOCTOR OF PHILOSOPHY

By
Kasidit Leoviriyakit
March 2005

I certify that I have read this dissertation and that, in my opinion, it is fully adequate in scope and quality as a dissertation for the degree of Doctor of Philosophy.

Antony Jameson
(Principal Adviser)

I certify that I have read this dissertation and that, in my opinion, it is fully adequate in scope and quality as a dissertation for the degree of Doctor of Philosophy.

Juan J. Alonso

I certify that I have read this dissertation and that, in my opinion, it is fully adequate in scope and quality as a dissertation for the degree of Doctor of Philosophy.

Ilan M. Kroo

I certify that I have read this dissertation and that, in my opinion, it is fully adequate in scope and quality as a dissertation for the degree of Doctor of Philosophy.

Robert W. MacCormack

Approved for the University Committee on Graduate Studies.

To my parents, Suthipong and Nunta

Abstract

This dissertation focuses on the problem of wing planform optimization for transonic aircraft based on flow simulation using Computational Fluid Dynamics(CFD) combined with an adjoint-gradient based numerical optimization procedure. The adjoint method, traditionally used for wing section design has been extended to cover planform variations and to compute the sensitivities of the structural weight of both the wing section and planform variations. The two relevant disciplines accounted for are the aerodynamics and structural weight. A simplified structural weight model is used for the optimization. Results of a variety of long range transports indicate that significant improvement in both aerodynamics and structures can be achieved simultaneously. The proof-of-concept optimal results indicate large improvements for both drag and structural weight. The work is an "enabling step" towards a realistic automated wing designed by a computer.

Acknowledgments

I consider myself very fortunate to have had Professor Antony Jameson as my adviser. Throughout my stay at Stanford, I have immensely gained from his professional and personal experiences. I have been inspired time and again by him and thank him for his belief in my potential. He has always encouraged me to pursue what I was passionate about. Since my high school years, I have been interested in the fascinating topic of aircraft design and with Antony's guidance and expertise in the adjoint method for aerodynamic shape optimization, I chose planform optimization for my thesis work.

Finishing this dissertation has been a long project. I would like to express my appreciation for the encouragement that I have received during this time from my family, colleagues, and aero/astro staffs. There are endless names to mention here. But some of those include James Thomas Rose who revised this dissertation as thoroughly as it were his own dissertation; Sriram, Arathi Gopinath, Sangho Kim, Ki Hwan Lee, Michael Harbeck, Edwin van der Weide, Georg May, Kaveh Hosseini, Karthik Palaniappan, Vejapong Juttijudata, Pimkhuan Kamnerdsupaphon, and others who I did not mention here for their sincere support.

I would also like to thank Professor Juan Alonso, Professor Robert MacCormack and Professor Ilan Kroo for participating in my dissertation committee and for their valuable remarks. My doctoral research was benefited by the Air Force Office of Science Research under grant No.AF F49620-98-1-2002/2005.

My Professors Vichit Laipradit and Fei-Bin Hsiao during my undergraduate years in Kasetsart University, Thailand and National Cheng Kung University, Taiwan, supported me all through and encouraged me to apply to American universities. I am very grateful to them. Last but not the least, I'd like to thank my father and mother for believing in me and supporting me throughout my studies. I would like to dedicate this dissertation to them.

Contents

List of Tables

List of Figures

Chapter 1

Introduction

1.1 Wing design

The wing is the most important component of an airplane. The wing affects not only its own performance, but also the performance of the entire airplane. From an aerodynamic perspective, the main source of the airplane drag is associated with the wing. As illustrated in figure 1.1, two-thirds of the total drag is related to the wing. Therefore a large emphasis should be placed on the aerodynamic wing-design.

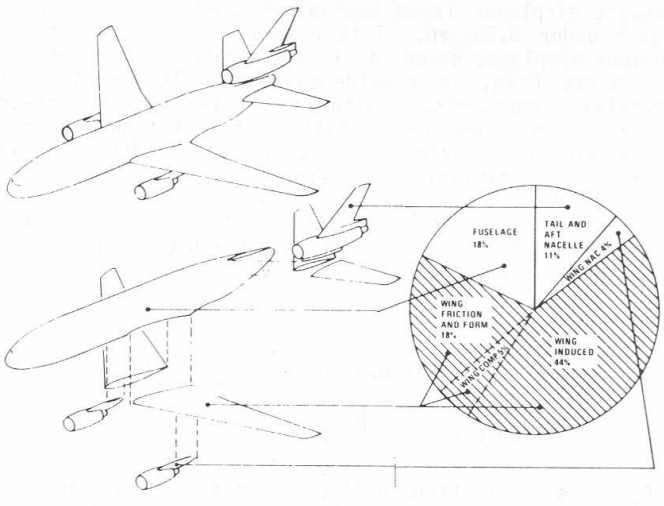

Figure 1.1: Typical drag breakdown by primary airplane components of transport aircraft at cruise conditions [46].

A standard approach used in the past to design a wing involves two main steps. The first step was to establish the general wing shape, airfoil types, approximate thickness ratio, design lift coefficient, and design Mach number from a design optimization study. The second step was to design a minimum weight wing while achieving as much of the two-dimensional airfoil performance as possible, minimizing any parasite or induced drag penalties, and satisfying all of the other general design criteria such as good drag characteristics, sufficient fuel volume, and minimum weight. References [70, 55, 61, 37] provide excellent descriptions for this standard approach.

For modern wing design, the procedure still follows the standard approach, but involving the use of computational fluid dynamics (CFD) codes to systematically study variations of shape, airfoil type, thickness, twist, etc. CFD solves the compressible Euler and Navier-Stokes equations and is mainly used to provide better understanding of the flow over the wing, but not to drive the wing design process. The wing refinement is done based on the intuition and experience of the designer.

Recently, CFD has been receiving attention as a design optimization tool. Numerical optimization has been combined with CFD. While there exist numerous well-developed optimization techniques, such as those described in reference [11], most techniques are not practical to the CFD-based optimization problems due to the different nature of the problems. The standard optimization problems generally assume that the function evaluation of the "figure of merit" (or the "cost function") can be evaluated easily and at low computational cost. The standard gradient-based optimization further expect similar simplicity of the "sensitivity information" (or the "gradient") evaluation. Moreover, they are mainly developed for problems of a small-to-moderate number of design parameters compared to the number of cost functions and constraints. The CFD-based optimization problems, on the other hand, require solving a non-linear system of partial differential equations to calculate the cost function and usually involve a large number of design parameters, especially for a design in transonic flow. Transonic flow is very sensitive to small shape perturbations. In order to achieve "shock-free" wing-sections, it generally requires a large number of parameters $\sim \mathcal{O}(10^3)$ to represent the wing surface. In an extreme case, the wing can be treated as a "free"surface. Therefore, the optimization algorithms that require a

large number of function evaluations are not well suited to the wing design problem.

Early attempts to combine CFD with numerical optimization made use of finite-difference calculations to obtain sensitivity information. This technique can be used to obtain the derivatives of all the flow quantities with existing flow solvers. One problem with this approach is the computational time required. To obtain the design sensitivities for a system involving n design parameters using one sided difference requires a well-converged solution of $n + 1$ flow analysis problems. This becomes prohibitive when n becomes large.

A practical method for CFD-based optimization emerged in 1988 when an adjoint method was first applied to the governing equations of transonic flow by Jameson [20]. The method applied control theory techniques to a system of partial differential equation and reduced the cost of gradient calculations to only two flow analyses, regardless of the number of design parameters n. This breakthrough enabled many more design variables than was previously practical for gradient-based aerodynamic shape optimization problem.

During the last decade, adjoint methods have been extensively developed and proven to be very effective for improving wing section shapes for fixed wing-planform. The framework has been well developed by Jameson[30, 26, 62]. He applied the adjoint method to redesign airfoils and wing sections in transonic flow. By using surface mesh points as the design parameter, the adjoint method to calculate the gradient information, and an iterative method to improve the shape in each iteration, he was able to achieve a shock-free-wing.

1.2 Planform optimization

1.2.1 Motivation to integrate shock-free wing section design with planform design

The capability to produce shock-free airfoils for a given wing planform, such as the method described in section 1.1, is very crucial. When integrating shock-free wing sections with planform design, it can enable planform configurations which would

previously have been restricted by strong compressibility drag.

Conventionally, wings of transonic aircraft require a large sweep or a small thickness-to-chord ratio of the wing section to lower the local Mach number and prevent strong shock wave formation. By implementing the shock-free concept, it is possible to weaken the compressibility drag without requiring as large a sweep or as small a thickness-to-chord ratio as conventionally designed. The sweep reduction and thickness increment will reduce the wing structural weight, as will later be discussed in section 1.2.2. The benefit on weight saving can be used to increase the span to reduce the induced drag. Because the induced drag is the largest component of drag, as illustrated in figure 1.1, the wing planform optimization has the potential to yield large drag savings without any penalty on the structural weight. Therefore, in this dissertation, we exploit the shock-free-wing technology in the combination with planform design to "cheat" the conventional intelligence of the planform design. With the right implementation, it may revolutionize wing design.

As a historical note, although the shock-free-wing method has only been newly developed during the last decade and has yet to be implemented to the real-world airplane, the idea of exploiting the shock-free airfoil to improve wing design is not new. A classic example occurred when Whitcomb [75, 76] introduced his famous supercritical airfoil. Since the airfoil produced the same amount of lift at lower negative pressure peak, compared to those of the conventional airfoil, the shock formation can be delayed. The transonic wings that were designed with the supercritical airfoil generally have less sweep and are structurally lighter compared to those designed with conventional airfoils.

1.2.2 Planform characteristics

Planform optimization can be considered as large scale design, compared to a section shape design. It affects both aerodynamic and structural characteristics of the wing. To formulate the optimization problem properly, it is important to understand how planform parameters affect drag and wing wight. A detailed discussion can also be found in reference [37].

First we define the planform parameters. There are many definitions for wing planform, depending on the design process. In some literature, the term "planform" is used interchangeably with "wing shape". In this dissertation, we use the term "planform" to collectively represent span, chord distribution, thickness-to-chord ratio, aspect ratio, and sweepback[55]. Next we discuss how these parameters affect the wing.

Span effects

Span generally affects drag and weight in the following ways:

- When the span is increased, it reduces the induced drag, regardless of wing area changes. If the increased span enlarges the wing area, the skin friction drag will be increased.
- The wing weight will be increase when we increase the span, both by the longer span and the increased bending load.

In general, the induced drag varies quadratically with the inverse of span, as illustrated here. Consider the induced drag coefficient

$$C_{D_i} = \frac{C_L^2}{\pi e \mathrm{AR}}$$

The induced drag can be written as

$$\begin{aligned} D_i &= C_{D_i} q_\infty S_{\mathrm{ref}} \\ &= \frac{\mathrm{Lift}^2}{\pi e b^2} \end{aligned}$$

where b is span length and e is span efficiency.

Because the induced drag is the largest portion of airplane drag as shown in figure 1.5, when we make the span longer (keeping the area constant), we can reduce the airplane drag dramatically but we also make the wing heavier. This relationship reveals the trade-off between drag and wing weight. This discussion also implies that pure aerodynamic optimization without span constraints will lead to an excessive

span. On the other hand, if a maximum span length is imposed as a constraint, we can clearly see that this constraint will always be active and there is no need for the optimization. By including the trade-off between drag and wing weight, this problem can be avoided. Therefore we propose an optimization that employs a trade-off between drag and wing weight to minimize a weighted sum of drag and weight.

Sweep effects

Increasing sweep angle influences drag and weight as follows:

- It reduces compressibility drag by reducing the local Mach number.
- It increases the wing weight by increasing the structural span and tip loading. When we sweep the wing more backward, the spanload tends to shift outboard as shown in figure 1.2. This increases the bending load and thus wing weight.

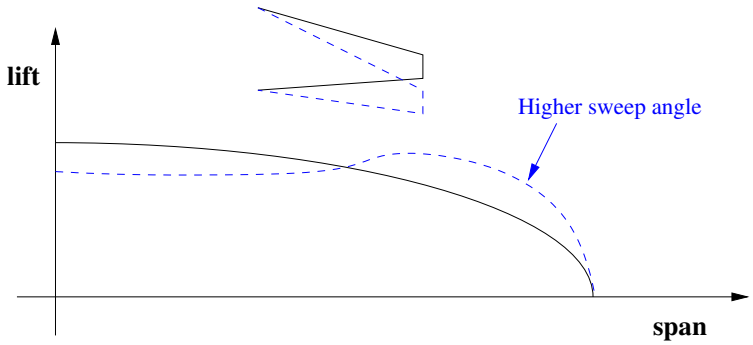

Figure 1.2: Effect of sweep on wing loading

Thickness effects

Thickness is generally described in terms of thickness-to-chord ratio t/c. The effect of t/c changes is as follows:

- Larger t/c increases the drag slightly by increasing the velocities, the adversity of the pressure gradients, and the compressibility drag.

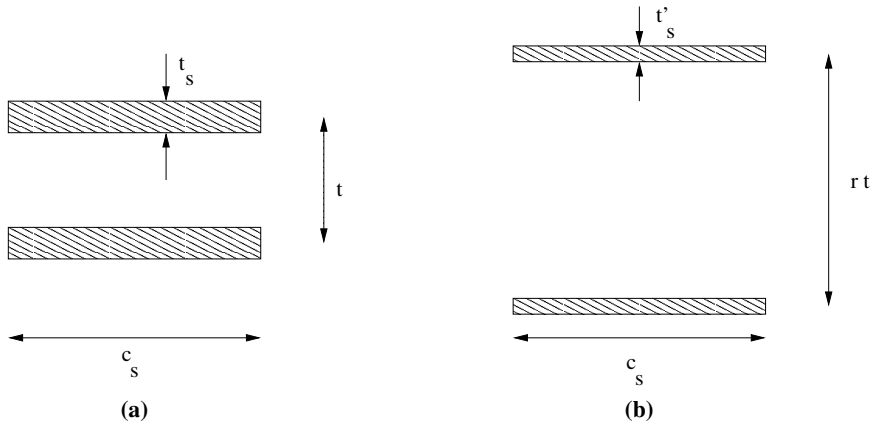

Figure 1.3: Effect of thickness variation on a simplified wing structure.

- Larger t/c also reduces the wing weight.

Figure 1.3 (a) shows a cross-section of a simplified wing structure that carries a wing bending load. The height of this beam is limited by the thickness of the wing (t). For a fully-stressed structure, the upper and low skin thickness t_s satisfies the relation

$$M = \sigma_{\text{allow}} t_s c_s t$$

where M is bending load, c_s is structural chord, and σ_{allow} is the allowable stress. If we increase the wing thickness by a factor of r while keeping the structural chord c_s constant, the new skin thickness t'_s of the thicker wing will be reduced by

$$t'_s = \frac{1}{r} t_s$$

to support the same bending moment at the fully stressed condition. The material cross-sectional area of the thicker wing is reduced by a factor of r from the original area. Therefore, from this simple analysis, the wing will be lighter when we increase the wing thickness.

Chord effects

Increasing the chord length at fixed wing thickness certainly reduces the thickness to chord ratio. However if the thickness to chord ratio is fixed, increasing the chord

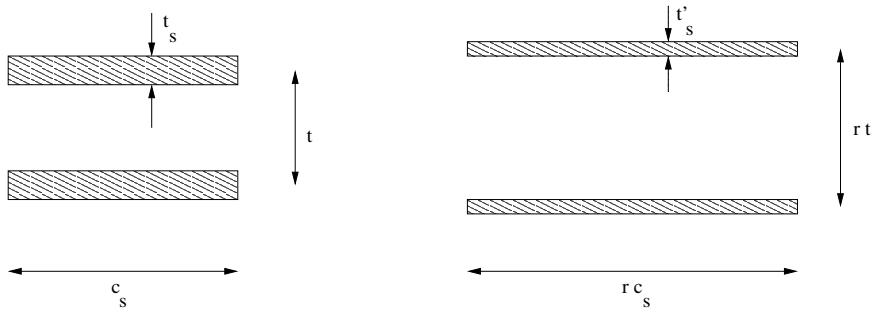

Figure 1.4: Effect of chord variation on a simplified wing structure.

leads to the following:

- It increases the drag by increasing the area. A simple analysis of skin friction [37] indicates that skin friction drag varies linearly with wetted area. Increasing chord length makes the wing area larger, giving higher drag.
- However, it reduces the wing weight.

In figure 1.4 we increase the chord length and the wing thickness by a factor r, keeping the ratio t/c constant. We can perform a simple analysis, similar to the one done earlier, for the effects of chord on the thickness of beam section. This results in a new skin thickness:

$$t'_s = \frac{1}{r^2} t_s$$

and the new material cross-sectional area gets smaller

$$\begin{aligned} \text{Area}_{\text{new}} &= 2t'_s r c_s && (1.1) \\ &= \frac{2t_s c_s}{r} && (1.2) \\ &= \frac{\text{Area}_{\text{old}}}{r}. && (1.3) \end{aligned}$$

For a real wing structure, the analysis is certainly more complicated. However, a good wing structure will follow this trend. The effects of sweep, span, thickness, and chord variation indicate that drag and wing weight are driven in opposite directions. In other words, this shows trade-offs between them. There trends shows that it may be possible to optimize the weighted sum of drag and wing weight.

1.2.3 Early work on planform optimization

There is extensive work on planform optimization, ranging from an analytical approach to high-fidelity numerical optimization. A classic analytical approach includes Prandtl's elliptical planform [59, 60], which minimized the induced drag. McGeer [51] extensively studied planform characteristics for low speed subsonic wings that led to the minimum induced drag for different constraints, using Fourier series and algebraic expressions to govern flow and structure models. McGeer also extended his method to high-speed subsonic planform design where empirical expressions were used to estimate compressibility drag [52]. The analytical approach works quite well when the governing equations can be solved analytically and the number of constraints is small.

When the number of constraints becomes large, various methods to combine a numerical optimization with governing equations have been proposed. Hutchison [15] proposed a method for high-speed civil transport wing design, using algebraic equations to estimate aircraft weight, supersonic drag, friction drag, and drag due to lift. Wakayama's [73, 74] optimizes drag and weight of commercial aircraft wings by combining numerical optimization with simplified flow and structural models. This method handles numerous constraints quite well and became a major optimization tool when Boeing designed the unconventional Blended Wing Body [72, 43].

For transonic flow, there is very limited work that truly employs the full Euler or Navier-Stokes as the flow model to optimize the planform [57, 67]. The main reason is the computational cost which becomes prohibitively expensive for sensitivity calculation as we discussed earlier in section 1.2.1.

It is not until the introduction of the control theory approach to design in the transonic flow by Jameson [20] that Euler and Navier-Stokes based-optimizations became practical [31]. The control theory approach is usually called an adjoint method because it requires us to solve the adjoint equation. Since then the adjoint method has been widely used to optimize airfoils and wings. This breakthrough enables the gradient-based aerodynamic shape optimization to handle many more design variables than was previously practical. This feature is important for shock-free design because transonic flow is very sensitive to small shape changes. To handle subtle geometry changes for shock weakening, it generally requires a large number of parameters for

the control geometry. During the 1990s and 2000s, the adjoint method has been a very active research topic. Numerous researchers have been focusing on the use of adjoint methods in many different areas [1, 10, 35, 49, 53, 63, 66]. However, none clearly exploits the benefit of this shock-free capability to redesign the wing planform. In this dissertation, we extend the adjoint method to cover planform design, and blend in shock-free design to develop a design methodology that has the potential to yield large improvements in aerodynamics without penalizing the structural weight.

1.2.4 Wing planform optimization with simplified structural weight

From the earlier discussion, the two relevant disciplines are aerodynamics and structural weight. Therefore we minimize a combination of drag and wing weight. This optimization not only makes the design more realistic, but we can also eliminate some constraints such as a thickness constraint that is required for pure aerodynamic shape optimization, without which the thickness-to-chord ratio would keep reducing to an extent that would make it impossible to fit a sufficient structure box or have enough volume to store the fuel inside the wing. Thus we mainly target the minimization of

$$I = \alpha_1 C_D + \alpha_2 C_W \tag{1.4}$$

Here α_1 and α_2 are properly chosen weighting constants, and $C_W = \frac{weight}{q_\infty S_{ref}}$ is a non-dimensional weight coefficient. This choice of cost function emphasizes the trade-off between aerodynamics and structures. For design of a long range transport aircraft, equation (1.4) actually centers around the idea of improving the range of the aircraft.

Consider the well known Breguet range equation which provides a good first estimate of the range of the airplane

$$R = \frac{V}{C}\frac{L}{D} ln \frac{W_e + W_f}{W_e} \tag{1.5}$$

where V is the speed, C is the specific fuel consumption of the engine, L/D is the

lift to drag ratio, W_e is the landing weight, and W_f is the weight of the fuel burnt. During the last few decades, the means to improve the efficiency of an airplane has centered around reducing the fuel consumption C of the engine, increasing VL/D, and reducing the airplane weight. The last two methods together imply that the constants α_1 and α_2 in the equation (1.4) can be estimated from the range equation (1.5).

Notice that the range equation also stresses the importance of transonic flight for a long range aircraft. Since airplanes should fly at the condition that maximizes VL/D and the typical drag variation is similar to that in figure 1.5, this means that the

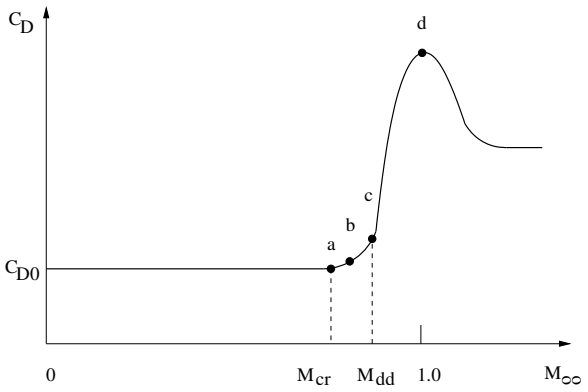

Figure 1.5: Typical variation of airplane drag with Mach number. M_{cr} and M_{dd} represent the critical and drag divergence Mach numbers respectively.

cruising speed should be increased until the onset of drag rise due to the formation of strong shock waves (point b in figure 1.5). Consequently, the best cruise speed is the transonic regime and for any wing design method/tool to be useful, the tool must be able to handle a design that involves the transonic flow.

1.3 Scope and contribution

In this dissertation, we develop a framework of planform design that makes use of the shock-free methodology extensively developed during the last decade. The key idea centers around the capability to weaken the shock and tune the trade-off between drag and structural weight of the design variables to improve the overall design without

leading to any unrealistic result. Because different design parameters affect drag and weight to a different degree, we exploit this hierarchy to gain improvements in drag without a corresponding weight penalty or producing an unrealistic shape.

To accomplish this we employ the wing planform as well as the wing sections as the design parameters and focus on the aerodynamic optimization with a simplified structural weight. During this development we aim to answer whether it is possible to take advantage of the shock-free feature.

Because we are more interested in exploring the benefit of the shock-free wing and to demonstrate how to implement the adjoint method for the weight, a quick implementation is to use an analytical expression to model the structure weight. This low-fidelity structural model serves the proof-of-concept purpose. It also establishes a guideline for higher-fidelity development. Therefore this work is the "enabling step" towards a realistic automated wing designed by a computer.

We follow the framework of aerodynamic shape optimization initially developed for wing section design by Jameson and extend the method to include planform design. To fully exploit the key advantage of the adjoint method on computational cost saving of sensitivity calculation, we extend the adjoint method to handle methods for planform sensitivity.

Along this line of development, we have contributed the following:

- Development of aerodynamic sensitivities to planform changes using the adjoint method. This may be considered as large scale optimization, compared to section optimization.

- Alternative gradient calculation that is less error-prone.

- Adjoint sensitivity of a simplified weight model for both section and planform design.

With the use of an adjoint method for both section and planform design, the computational cost is very low. It is so low that it allows the design to be done on a laptop computer. Actually, most inviscid results demonstrated in chapter 4 were done on the author's laptop (Athlon 3.2 GHz) in less than half an hour.

Finally, it is important discuss criteria that are outside the scope of this dissertation. At this "enabling step", we focus on exploring the benefit of the shock-free wing and to demonstrate how to enable the implementation of the adjoint method, beyond just aerodynamics. As a result, we have limited our study to aerodynamic design with a simplified weight model. Moreover, we use a relatively simple cost function which minimizes drag and weight. No explicit constraints, other than fixed lift, were imposed in this study.

In real airplane design, of course, there are many other criteria: multiple design points, fuel distributions, stability-and-control effects, aero-elastics, etc. A survey by Lynch[46] indicates some of the general design criteria that must be met in the design of any efficient transonic wing. These requirements include:

1. Good drag characteristics (parasite, induced, compressibility) over a range of lift coefficients, i.e. $C_{L_{\text{design}}} \pm 0.1$ at M_{cruise}.
2. No excess penalties for installation of nacelle-pylons, fairing, etc.
3. Buffet boundary high enough ($1.3g$ margin required) to permit cruising at design lift coefficients.
4. No pitch-up tendencies near stall and buffet boundary.
5. Control surface effectiveness must be maintained.
6. No unsatisfactory off-design performance.
7. Sufficient fuel volume for design range.
8. Structurally efficient (to minimize weight)
9. Must provide sufficient space to house main landing gear.
10. Must be compatible with selected high-lift system.
11. Must be consistent with airplane design for relaxed static stability.
12. Must be manufacturable at a reasonable cost.

Of course, it would be next to impossible to take into account all of these criteria to perform an optimization. Nevertheless, the design methodology presented in this work provides the basis for an extension to form a more complete wing design tool.

1.4 Outline

The rest of this dissertation starts with the description of flow and structure models. Chapter 2 describes the mathematical formulation of this dissertation, including formulation of the adjoint equation for a variety of cost functions. Chapter 3 applies the basic idea of the adjoint method to planform design. A technique to determine planform gradient that is independent of the number of planform variables is also described in the same chapter. It also contains gradient comparisons between the finite difference and adjoint methods for validation purpose. Chapter 4 shows results for both inviscid and viscous designs for compressible flow. Case studies to improve airplane performance are also shown, and reveal an important trend to improve many existing wings for long range transport aircraft. Finally, chapter 5 concludes this dissertation.

Chapter 2

Mathematical formulation

2.1 The adjoint approach to wing design

The adjoint method has been proposed for shape design since 1974[58] but it did not have much impact on aerodynamic design until its application to transonic flow[20]. The major impact arose from its capability to effectively handle a design problem that involves a large number of design variables and is governed by a complex mathematical model, such as fluid flow.

Let us consider a wing design problem:

$$\begin{aligned} Minimizing \quad & I(w,S) && (2.1)\\ w.r.t \quad & S && (2.2)\\ subjected\ \ to \quad & R(w,S)=0 && (2.3) \end{aligned}$$

where w is the flow variable, S is the vector of wing design parameters, and $R(w,S) = 0$ is the flow equation.

For instance, for a drag minimization problem we can take $I = C_D$ which is an integral of flow w (pressure and shear force) over the wing S (represented by parameters such as airfoils and planform). We modify S (the airfoils and planform) to reduce the drag. The pressure and shear force are obtained from the flow equation $R = 0$ using CFD. (Later in chapter 3, we will set the cost function I as a combination

of drag, structural weight, and inverse design.)

A change in S results in a change

$$\delta I = \left[\frac{\partial I}{\partial w}\right]^T \delta w + \left[\frac{\partial I}{\partial S}\right]^T \delta S, \tag{2.4}$$

and δw is determined from the equation

$$\delta R = \left[\frac{\partial R}{\partial w}\right] \delta w + \left[\frac{\partial R}{\partial S}\right] \delta S = 0. \tag{2.5}$$

The finite difference approach attempts to solve δw from equation (2.5) and substitute it into equation (2.4) to calculate δI . However, as we discussed in section 1.1, when the dimension of S is large, this approach becomes impractical.

For an adjoint approach, we try to avoid solving for δw. This is done by introducing a Lagrange multiplier ψ, and subtracting the variation δR from the variation δI without changing the result. Thus, equation (2.4) can be replaced by

$$\begin{aligned} \delta I &= \left[\frac{\partial I}{\partial w}\right]^T \delta w + \left[\frac{\partial I}{\partial S}\right]^T \delta S - \psi^T \left(\left[\frac{\partial R}{\partial w}\right] \delta w + \left[\frac{\partial R}{\partial S}\right] \delta S \right) \\ &= \left\{ \left[\frac{\partial I}{\partial w}\right]^T - \psi^T \left[\frac{\partial R}{\partial w}\right] \right\} \delta w + \left\{ \left[\frac{\partial I}{\partial S}\right]^T - \psi^T \left[\frac{\partial R}{\partial S}\right] \right\} \delta S \end{aligned} \tag{2.6}$$

Choosing ψ to satisfy the adjoint equation,

$$\left[\frac{\partial R}{\partial w}\right]^T \psi = \left[\frac{\partial I}{\partial w}\right], \tag{2.7}$$

the first term is eliminated, and we find that

$$\delta I = \mathcal{G}^T \delta S, \tag{2.8}$$

where

$$\mathcal{G}^T = \left[\frac{\partial I}{\partial S}\right]^T - \psi^T \left[\frac{\partial R}{\partial S}\right].$$

The advantage is that equation (2.8) is independent of δw, with the result that the

gradient of I with respect to an arbitrary number of design variables can be determined without the need for additional flow-field evaluations.

Once the gradient vector $\mathcal{G}$ has been established, it may now be used to determine a direction of improvement. The simplest procedure is to make a step in the negative gradient direction (steepest descent method) by setting

$$\delta S = -\lambda \mathcal{G}$$

where λ is positive and small enough that the first variation is an accurate estimate of δI. The variation of the cost function then becomes

$$\begin{aligned} \delta I &= -\lambda \mathcal{G}^T \mathcal{G} \\ &\leq 0 \end{aligned}$$

More sophisticated search procedures may be used such as quasi-Newton methods, which attempt to estimate the second derivative $\frac{\partial^2 I}{\partial S_i \partial S_j}$ of the cost function from changes in the gradient $\frac{\partial I}{\partial S}$ in successive optimization steps. These methods also generally introduce line searches to find the minimum in the search direction which is defined at each step. Reference [11] provides a good description for those techniques. However, not all the techniques are practical for our wing design problem. Line searches, for example, would require extra flow calculations, which we try to avoid.

2.2 Flow equation

In section 2.1, the flow variables and the geometry are related by the governing equation $R(w, S) = 0$. This section discusses the details of these governing equations.

For a computational method to be useful in the design process, it must be based on a mathematical model that represents significant features of the flow such as shock waves, vortices, and boundary layers. Throughout this dissertation, both the Euler and Navier-Strokes equations are used to model the flow. We will use the Navier-Strokes (NS) equations to derive the governing adjoint equations. The Euler equation

can be simply done by dropping the viscous terms of the NS equations.

It proves convenient to denote the Cartesian coordinates and velocity components by x_1, x_2, x_3 and u_1, u_2, u_3, and to use the convention that summation over $i = 1$ to 3 is implied by a repeated index i. Then, the three-dimensional Navier-Stokes equations may be written as

$$\frac{\partial w}{\partial t} + \frac{\partial f_i}{\partial x_i} = \frac{\partial f_{vi}}{\partial x_i} \quad \text{in } \mathcal{D}, \tag{2.9}$$

where the state vector w, inviscid flux vector f and viscous flux vector f_v are described respectively by

$$w = \left\{ \begin{array}{c} \rho \\ \rho u_1 \\ \rho u_2 \\ \rho u_3 \\ \rho E \end{array} \right\}, \quad f_i = \left\{ \begin{array}{c} \rho u_i \\ \rho u_i u_1 + p\delta_{i1} \\ \rho u_i u_2 + p\delta_{i2} \\ \rho u_i u_3 + p\delta_{i3} \\ \rho u_i H \end{array} \right\}, \quad f_{vi} = \left\{ \begin{array}{c} 0 \\ \sigma_{ij}\delta_{j1} \\ \sigma_{ij}\delta_{j2} \\ \sigma_{ij}\delta_{j3} \\ u_j\sigma_{ij} + k\frac{\partial T}{\partial x_i} \end{array} \right\}, \tag{2.10}$$

where δ_{ij} is the Kronecker delta function. Also,

$$p = (\gamma - 1)\,\rho \left\{ E - \frac{1}{2} u_i u_i \right\}, \tag{2.11}$$

and

$$\rho H = \rho E + p \tag{2.12}$$

where γ is the ratio of the specific heats. The viscous stresses may be written as

$$\sigma_{ij} = \mu \left(\frac{\partial u_i}{\partial x_j} + \frac{\partial u_j}{\partial x_i} \right) + \lambda \delta_{ij} \frac{\partial u_k}{\partial x_k}, \tag{2.13}$$

where μ and λ are the first and second coefficients of viscosity. The coefficient of thermal conductivity and the temperature are computed as

$$k = \frac{c_p \mu}{Pr}, \qquad T = \frac{p}{R\rho}, \tag{2.14}$$

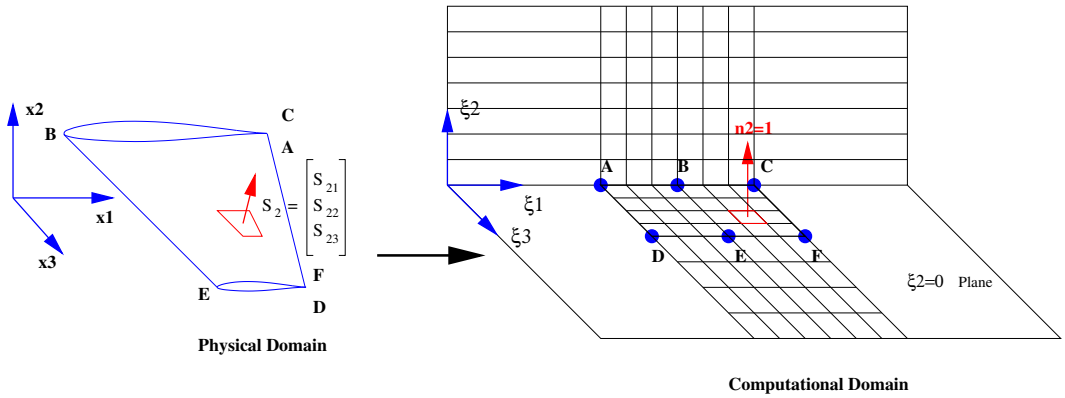

Figure 2.1: Physical and computational domains

where Pr is the Prandtl number, c_p is the specific heat at constant pressure, and R is the gas constant.

Using a transformation to a fixed computational domain as shown in figure 2.1, the Navier-Stokes equations can be written in the transformed coordinates as

$$\frac{\partial (Jw)}{\partial t} + \frac{\partial (F_i - F_{vi})}{\partial \xi_i} = 0 \quad \text{in } \mathcal{D}, \tag{2.15}$$

where the inviscid terms have the form

$$\frac{\partial F_i}{\partial \xi_i} = \frac{\partial}{\partial \xi_i} \left(S_{ij} f_j \right),$$

the viscous terms have the form

$$\frac{\partial F_{vi}}{\partial \xi_i} = \frac{\partial}{\partial \xi_i} \left(S_{ij} f_{vj} \right),$$

and $S_{ij} = JK_{ij}^{-1}$ are the coefficients of the Jacobian matrix of the transformation, which represent the projection of the ξ_i cell face along the x_j axis.

2.3 Structural weight model

Wing weight is directly given by the wing structure, which is sized by aerodynamic load, allowable deflection, and failure criteria such as buckling. Different methods to estimate wing weight have been proposed, ranging from empirical expression to complex Finite Element Analysis. At the detailed design level, once the wing structure has been laid out, structure engineers use finite element analysis to size the interior structure to satisfy various criteria. Then the material weight of each component is added up to calculate the structural weight.

When the detailed structure layout is not known, which is usually the case for conceptual and preliminary design levels, it is very difficult to predict the structural weight correctly. There is much active research [4, 45, 50] focusing on the optimum structural design for a given wing. Most works extensively use finite element analysis and couple high-fidelity flow solutions to capture the aero-elastic effects.

Although the use of high-fidelity methods to estimate the wing weight certainly gives more accurate weight prediction, the focus of this dissertation is mainly on demonstrating the new benefit of using shock-free technology to gain a large improvement in aerodynamic performance without a penalty on structural weight, regardless of the fidelity of the structural model. The quickest approach is to select a structure model that can be expressed analytically. However, in order to demonstrate the adjoint method approach to structural-weight sensitivity, this model should be sensitive to the aerodynamic loads as well. For future implementation with a high fidelity weight model, the approach will need to be augmented by the addition of structural-adjoint equations.

An analytical model to estimate the minimal material to resist material and buckling failures has been developed by Wakayama [73]. When shear and buckling effects are small, they may be neglected, resulting in a simplified model developed by Kroo [38] and McGeer[51]. In this dissertation, we follow the analysis developed by Kroo and McGeer, which combines analytical expression with empirical expression.

The wing structure is modeled by a box beam [56], whose major structural material is the upper and lower box skin. The skin thickness (t_s) varies along the span and

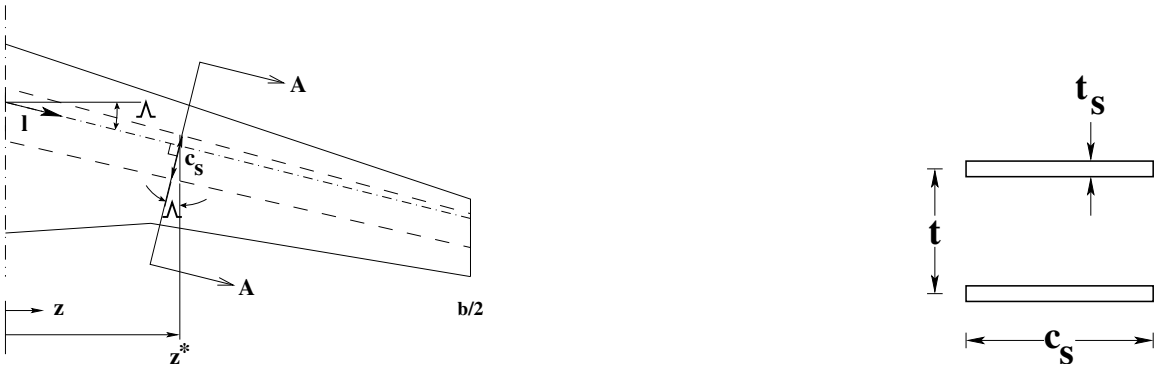

(a) swept wing planform

(b) section A-A

Figure 2.2: Structural model for a swept wing

resists the bending moment caused by the wing lift. Then, the structural wing weight W_{wing} can be calculated on the basis of the skin material.

Consider the box structure of a swept wing whose quarter-chord swept is Λ and its cross-section A-A as shown in figures 2.2. The skin thickness t_s, structure box chord c_s, and overall thickness t vary along the span, such that the local stress is equal to the maximum allowable stress everywhere. The maximum normal stress from the bending moment at a section z^* is

$$\sigma = \frac{M(z^*)}{t\ t_s c_s}$$

The corresponding structural weight of this box beam is is

$$\begin{aligned} W_{\text{wing}_{\text{box}}} &= \rho_{\text{mat}} g \int_{\text{structual span}} 2 t_s c_s dl \\ &= 2\frac{\rho_{\text{mat}} g}{\sigma cos(\Lambda)} \int_{-\frac{b}{2}}^{\frac{b}{2}} \frac{M(z^*)}{t(z^*)} dz^* \\ &= 4\frac{\rho_{\text{mat}} g}{\sigma cos(\Lambda)} \int_{0}^{\frac{b}{2}} \frac{M(z^*)}{t(z^*)} dz^*, \end{aligned}$$

and

$$\begin{aligned} C_{W_b} &= \frac{W_{\text{wing}_{\text{box}}}}{q_\infty S_{\text{ref}}} \\ &= \frac{\beta}{cos(\Lambda)} \int_0^{\frac{b}{2}} \frac{M(z^*)}{t(z^*)} dz^*, \end{aligned} \tag{2.16}$$

where

$$\beta = \frac{4\rho_{\text{mat}} g}{\sigma q_\infty S_{ref}},$$

ρ_{mat} is the material density, and g is the acceleration due to gravity.

The bending moment can be calculated by integrating pressure toward the wing tip. Ignoring the end effects due to the rotated axis of the box beam,

$$\begin{aligned} M(z^*) &= -\int_{z^*}^{\frac{b}{2}} \frac{p(x,z)(z-z^*)}{cos(\Lambda)} dA \\ &= -\int_{z^*}^{\frac{b}{2}} \oint_{\text{wing}} \frac{p(x,z)(z-z^*)}{cos(\Lambda)} dx dz \end{aligned}$$

Thus

$$C_{W_b} = \frac{-\beta}{cos(\Lambda)^2} \int_0^{\frac{b}{2}} \int_{z^*}^{\frac{b}{2}} \oint_{\text{wing}} \frac{p(x,z)(z-z^*)}{t(z^*)} dx dz dz^* \tag{2.17}$$

For the subsequent derivation of the corresponding adjoint boundary condition in section B.6, C_{W_b} must be expressed as $\int_{\mathcal{B}} d\mathcal{B}_\xi$ in the computational domain, or $\int\int dxdz$ in a physical domain to match the boundary term of equation (2.25).

To switch the order of integral of equation (2.17), introduce a Heaviside function

$$H(z-z^*) = \begin{cases} 0, & z < z^* \\ 1, & z > z^* \end{cases}$$

Then equation (2.17) can be rewritten as

$$\begin{aligned} C_{W_b} &= \frac{-\beta}{cos(\Lambda)^2} \cdot \\ &\quad \int_0^{\frac{b}{2}} \int_0^{\frac{b}{2}} \oint_{\text{wing}} \frac{p(x,z)H(z-z^*)(z-z^*)}{t(z^*)} dx dz dz^* \\ &= \frac{-\beta}{cos(\Lambda)^2} \int_0^{\frac{b}{2}} \oint_{\text{wing}} p(x,z)K(z) dx dz, \end{aligned} \tag{2.18}$$

where

$$\begin{aligned} K(z) &= \int_0^{\frac{b}{2}} \frac{H(z-z^*)(z-z^*)}{t(z^*)} dz^* \\ &= \int_0^{z} \frac{z-z^*}{t(z^*)} dz^* \end{aligned}$$

In the computational domain,

$$C_{W_b} = \frac{-\beta}{cos(\Lambda)^2} \oint_{\mathcal{B}} p(\xi_1, \xi_3) K(\xi_3) S_{22} d\xi_1 d\xi_3, \tag{2.19}$$

and $K(\xi_3)$ is a one-to-one mapping of $K(z)$.

Finally, to account for the weight of other wing material such as ribs, spars, webs, stiffeners, leading and trailing edges, slats, flaps, main gear doors, primer and sealant, we multiply C_{W_b} of equation (2.19) by a correction factor $K_{\text{corr,b}}$.

Moreover, statistical correlation over the range of aircraft type indicates a relationship between W_{wing}/S and $W_{\text{wing}_{\text{box}}}/S$ as a linear function, shown in figure 2.3. A good reference can be found in reference[37]. Therefore we add another term to account for area-dependent wing weight

$$C_{W_s} = \frac{1}{S\text{ref}} \oint_{\mathcal{B}} |S_{22}| d\xi_1 d\xi_3, \quad |S_{22}| = \sqrt{S_{2i} S_{2i}}, \tag{2.20}$$

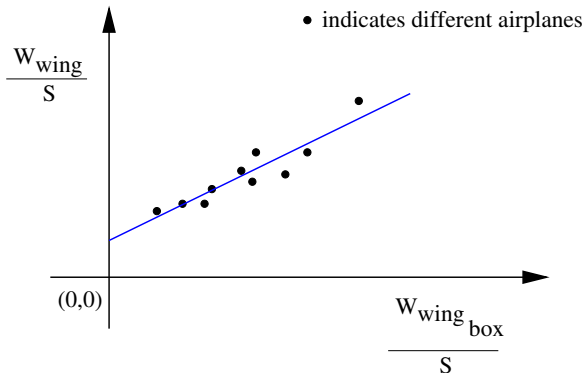

Figure 2.3: Statistical correlation of the total wing weight and the box weight based on wing loading over the range of aircraft type.

along with a correction factor $K_{\text{corr,s}}$. Thus

$$C_W = K_{\text{corr,b}} C_{W_b} + K_{\text{corr,s}} C_{W_s} \tag{2.21}$$

2.4 Design using the Euler and Navier-Stokes equations

Suppose we choose to minimize the cost function of a boundary integral

$$I = \int_{\mathcal{B}} \mathcal{M}(w, S)\, d\mathcal{B}_\xi + \int_{\mathcal{B}} \mathcal{N}(w, S)\, d\mathcal{B}_\xi$$

where $\mathcal{M}(w, S)$ could be an aerodynamic cost function, e.g. drag coefficient, and $\mathcal{N}(w, S)$ could be a structural cost function, e.g. structure weight. A shape change produces a variation in the flow solution δw and the metrics δS, which in turn produce a variation in the cost function

$$\delta I = \int_{\mathcal{B}} \delta\mathcal{M}(w, S)\, d\mathcal{B}_\xi + \int_{\mathcal{B}} \delta\mathcal{N}(w, S)\, d\mathcal{B}_\xi,$$

with

$$\begin{aligned} \delta\mathcal{M} &= [\mathcal{M}_w]_I \, \delta w + \delta\mathcal{M}_{II}, \quad \text{and} \\ \delta\mathcal{N} &= [\mathcal{N}_w]_I \, \delta w + \delta\mathcal{N}_{II}. \end{aligned}$$

Here we continue to use the subscripts I and II to distinguish between the contributions associated with the variation of the flow solution δw and those associated with the metric variations δS respectively. Thus $[\mathcal{M}_w]_I$ and $[\mathcal{N}_w]_I$ represent $\frac{\partial \mathcal{M}}{\partial w}$ and $\frac{\partial \mathcal{N}}{\partial w}$ with the metrics fixed, while $\delta\mathcal{M}_{II}$ and $\delta\mathcal{N}_{II}$ represent the contribution of the metric variations δS to $\delta\mathcal{M}$ and $\delta\mathcal{N}$.

In the steady state, the constraint equation (2.15) specifies the variation of the state vector δw by

$$\frac{\partial}{\partial \xi_i} \delta \left(F_i - F_{vi} \right) = 0.$$

Here δF_i and δF_{vi} can also be split into contributions associated with δw and δS using the notation

$$\begin{aligned} \delta F_i &= [F_{iw}]_I \, \delta w + \delta F_{iII} \\ \delta F_{vi} &= [F_{viw}]_I \, \delta w + \delta F_{viII}. \end{aligned}$$

Multiplying by a co-state vector ψ, which will play an analogous role to the Lagrange multiplier, and integrating over the domain produces

$$\int_{\mathcal{D}} \psi^T \frac{\partial}{\partial \xi_i} \delta \left(F_i - F_{vi} \right) d\mathcal{D}_\xi = 0.$$

If ψ is differentiable this may be integrated by parts to give

$$\int_{\mathcal{B}} n_i \psi^T \delta \left(F_i - F_{vi} \right) d\mathcal{B}_\xi - \int_{\mathcal{D}} \frac{\partial \psi^T}{\partial \xi_i} \delta \left(F_i - F_{vi} \right) d\mathcal{D}_\xi = 0. \tag{2.22}$$

Since the left hand expression is equal to zero, it can be subtracted from the variation

in the cost function to give

$$\begin{aligned}\delta I &= \int_{\mathcal{B}} \left[\delta\mathcal{M} + \delta\mathcal{N} - n_i\psi^T\delta\left(F_i - F_{vi}\right)\right] d\mathcal{B}_\xi \\ &+ \int_{\mathcal{D}} \left[\frac{\partial\psi^T}{\partial\xi_i}\delta\left(F_i - F_{vi}\right)\right] d\mathcal{D}_\xi. \end{aligned} \tag{2.23}$$

Now, since ψ is an arbitrary differentiable function, it can be chosen in such a way that δI no longer depends explicitly on the variation of the state vector δw. The gradient of the cost function can then be evaluated directly from the metric variations without having to recompute the variation δw resulting from the perturbation of each design variable.

The variation δw may be eliminated from (2.23) by equating all field terms with subscript "I" to produce a differential adjoint system governing ψ

$$\frac{\partial\psi^T}{\partial\xi_i}\left[F_{iw} - F_{viw}\right]_I = 0 \quad \text{in } \mathcal{D}. \tag{2.24}$$

The corresponding adjoint boundary condition is produced by equating the subscript "I" boundary terms in equation (2.23) to produce

$$n_i\psi^T\left[F_{iw} - F_{viw}\right]_I = \left[\mathcal{M}_w\right]_I + \left[\mathcal{N}_w\right]_I \quad \text{on } \mathcal{B}. \tag{2.25}$$

The remaining terms from equation (2.23) then yield a simplified expression for the variation of the cost function which defines the gradient

$$\begin{aligned}\delta I &= \int_{\mathcal{B}} \left\{\delta\mathcal{M}_{II} + \delta\mathcal{N}_{II} - n_i\psi^T\left[\delta F_i - \delta F_{vi}\right]_{II}\right\} d\mathcal{B}_\xi \\ &+ \int_{\mathcal{D}} \left\{\frac{\partial\psi^T}{\partial\xi_i}\left[\delta F_i - \delta F_{vi}\right]_{II}\right\} d\mathcal{D}_\xi, \end{aligned} \tag{2.26}$$

By choosing ψ to satisfy the adjoint equation with appropriate boundary conditions depending on the cost function, the explicit dependence on δw is eliminated. This allows the cost variations to be expressed in terms of δS and the adjoint solution.

Thus we obtain

$$\delta I = \int \mathcal{G}\delta S \, d\xi = \langle \mathcal{G}, \delta S \rangle$$

where $\mathcal{G}$ is the infinite dimensional gradient (Frechet derivative) at the cost of one flow and one adjoint solution. Then one can make an improvement by setting

$$\delta S = -\lambda \mathcal{G}$$

Although $\mathcal{G}$ can be obtained directly from equation (2.26), the explicit form of equation (2.26) is usually cumbersome to represent. A more compact form can be obtained by integrating the last term of equation (2.26) by parts

$$\begin{aligned} \delta I &= \int_{\mathcal{B}} \left\{ \delta \mathcal{M}_{II} + \delta \mathcal{N}_{II} - n_i \psi^T \left[\delta F_i - \delta F_{vi} \right]_{II} \right\} d\mathcal{B}_\xi \\ &+ \int_{\mathcal{B}} n_i \psi^T \left[\delta F_i - \delta F_{vi} \right]_{II} d\mathcal{B}_\xi - \int_{\mathcal{D}} \psi^T \frac{\partial}{\partial \xi_i} \delta \left[F_i - F_{vi} \right]_{II} d\mathcal{D}_\xi \end{aligned} \tag{2.27}$$

The middle terms cancel and equation (2.27) reduces to

$$\delta I = \int_{\mathcal{B}} \left\{ \delta \mathcal{M}_{II} + \delta \mathcal{N}_{II} \right\} d\mathcal{B}_\xi - \int_{\mathcal{D}} \psi^T \delta R_{II} d\mathcal{D}_\xi \tag{2.28}$$

Mathematically equations (2.26) and (2.28) are equivalent. However from a programming viewpoint, equation (2.28) is much more compact and easier to program.

2.5 Adjoint equation and boundary conditions

In this section we select an inverse design problem in the inviscid flow to illustrate how to develop the adjoint equation and the corresponding boundary conditions. Then we summarize the adjoint equation and boundary conditions for various optimization problem, including minimization of drag and structural weight. The full derivation of adjoint formulation is quite complicated. The detailed derivations can be found in appendix B.

2.5.1 Inviscid inverse design: Illustration

For the inverse design problem, we search for the wing shape that matches a desired pressure distribution p_d. The cost function is expressed as

$$I = \frac{1}{2}\int_{\mathcal{B}} (p - p_d)^2 \, dS \tag{2.29}$$

For simplicity, we will assume that the wing surface is mapped from a physical domain to a computational coordinate surface $\xi_2 = 0$, as shown in figure 2.1, which is the area surrounded by points $A, B, C, D, E,$ and F. On this $\xi_2 = 0$ surface,

$$n_1 = n_3 = 0, \quad n_2 = 1, \quad d\mathcal{B}_\xi = d\xi_1 d\xi_3.$$

Following the notation S_{ij} to represent the projection of the computational ξ_i cell face along the physical x_j axis, a wing area vector can be written as

$$S_2 = \left\{ \begin{array}{c} S_{21} \\ S_{22} \\ S_{23} \end{array} \right\}$$

In this computational domain, the cost function (2.29) is transformed to

$$I = \frac{1}{2}\int\int_{\mathcal{B}_w} (p - p_d)^2 \, |S_2| \; d\xi_1 d\xi_3, \tag{2.30}$$

where the quantity

$$|S_2| = \sqrt{S_{2j} S_{2j}}$$

denotes the face area corresponding to a unit element of face area in the computational domain.

To derive the adjoint equation and boundary condition of this inverse design problem, consider the variation of the cost function (2.30)

$$\delta I = \int\int_{\mathcal{B}_w} (p - p_d)|S_2|\delta p \; d\xi_1 d\xi_3 + \frac{1}{2}\int\int_{\mathcal{B}_w} (p - p_d)^2 \, \delta \, |S_2| \; d\xi_1 d\xi_3. \tag{2.31}$$

Also recall the inviscid portion of equation(2.22)

$$\int_{\mathcal{B}} n_i \psi^T \delta F_i d\mathcal{B}_\xi - \int_{\mathcal{D}} \frac{\partial \psi^T}{\partial \xi_i} \delta F_i d\mathcal{D}_\xi = 0. \tag{2.32}$$

We assume that the boundary contributions at the far field may either be neglected or else eliminated by a proper choice of boundary conditions. Moreover because the wing is restricted to the $\xi_2 = 0$ surface, the only non-zero n_i is n_2. Therefore we consider only the variation δF_2 for the boundary integral of equation (2.32). Recall the explicit form of F_2

$$F_2 = \left\{ \begin{array}{c} \rho U_2 \\ \rho U_2 u_1 + p S_{21} \\ \rho U_2 u_2 + p S_{22} \\ \rho U_2 u_3 + p S_{23} \\ \rho U_2 H \end{array} \right\}.$$

Because of the flow tangency boundary condition, we set $U_2 = 0$ and the variation of the inviscid flux at the wing boundary is reduced to

$$\delta F_2 = \delta p \left\{ \begin{array}{c} 0 \\ S_{21} \\ S_{22} \\ S_{23} \\ 0 \end{array} \right\} + p \left\{ \begin{array}{c} 0 \\ \delta S_{21} \\ \delta S_{22} \\ \delta S_{23} \\ 0 \end{array} \right\}. \tag{2.33}$$

Therefore, equation (2.32) can be simplified and then subtracted from equation (2.31)

to give

$$\begin{aligned}
\delta I &= \iint_{\mathcal{B}_w} (p - p_d)|S_2|\delta p \; d\xi_1 d\xi_3 + \frac{1}{2}\iint_{\mathcal{B}_w} (p - p_d)^2 \, \delta \, |S_2| \; d\xi_1 d\xi_3 \\
&- \iint_{\mathcal{B}_w} (\psi_2 S_{21} + \psi_3 S_{22} + \psi_4 S_{23}) \, \delta p \; d\xi_1 d\xi_3 \\
&- \iint_{\mathcal{B}_w} p \, (\psi_2 \delta S_{21} + \psi_3 \delta S_{22} + \psi_4 \delta S_{23}) \; d\xi_1 d\xi_3 \\
&+ \int_{\mathcal{D}} \frac{\partial \psi^T}{\partial \xi_i} S_{ij} \frac{\partial f_j}{\partial w} \delta w \; d\mathcal{D}_\xi + \int_{\mathcal{D}} \frac{\partial \psi^T}{\partial \xi_i} \delta S_{ij} f_j \; d\mathcal{D}_\xi. \qquad (2.34)
\end{aligned}$$

To eliminate the flow dependencies δp and δw from the variation of the cost function (2.34), we can choose ψ to satisfy

$$\left[S_{ij} \frac{\partial f_j}{\partial w} \right]^T \frac{\partial \psi}{\partial \xi_i} = 0 \quad \text{in } \mathcal{D}, \qquad (2.35)$$

and

$$\psi_2 \frac{S_{21}}{|S_2|} + \psi_3 \frac{S_{22}}{|S_2|} + \psi_4 \frac{S_{23}}{|S_2|} = p - p_d \quad \text{on } \mathcal{B}_w,$$

which is equivalent to

$$\psi_{j+1} n_j = p - p_d, \qquad (2.36)$$

where n_j are the components of the surface normal given by:

$$n_j = \frac{S_{2j}}{|S_2|}$$

Equation (2.35) is called the "adjoint equation", which is linear in terms of ψ. Because it is derived from the flow equation, which are the partial differential equations, the adjoint equation requires an adjoint boundary condition (2.36).

Once the adjoint variables ψ satisfy the adjoint equation and boundary condition,

the variation of the cost function (2.34) is reduced to

$$\begin{aligned}\delta I &= \frac{1}{2}\int\int_{\mathcal{B}_w}(p-p_d)^2\,\delta\,|S_2|\;d\xi_1 d\xi_3 \\ &- \int\int_{\mathcal{B}_w} p\,(\psi_2\delta S_{21}+\psi_3\delta S_{22}+\psi_4\delta S_{23})\;d\xi_1 d\xi_3 \\ &+ \int_{\mathcal{D}}\frac{\partial\psi^T}{\partial\xi_i}\delta S_{ij} f_j\;d\mathcal{D}_\xi. \end{aligned} \tag{2.37}$$

This form is quite complicated and could be error-prone. We can make it more compact as proposed in section 2.4 by integrating the last term by parts to give

$$\delta I = \frac{1}{2}\int\int_{\mathcal{B}_w}(p-p_d)^2\,\delta\,|S_2|\;d\xi_1 d\xi_3 - \int_{\mathcal{D}}\psi^T\frac{\partial}{\partial\xi_i}\delta S_{ij} f_j\;d\mathcal{D}_\xi. \tag{2.38}$$

To calculate the gradient of a design parameter $\mathcal{F}$, we perturb the shape with respect to the parameter $\mathcal{F}$ to produce δS on $\mathcal{B}_w$ and δS_{ij} on $\mathcal{D}$ then use equation (2.38) or (2.37) to calculate δI. Then the gradient is

$$\mathcal{G} = \frac{\delta\mathcal{I}}{\delta\mathcal{F}} \tag{2.39}$$

We repeat the same process for each different design parameter. However the advantage of equations (2.38) and (2.37) is that they are independent of flow variations δp and δw. Therefore, we are not required to re-solve the flow equation. This gives us a large advantage for gradient calculation, especially when the number of design variables is large as we have in full wing optimization.

2.5.2 Practical design cost functions

Following the same procedure, the adjoint equation for the design using the Navier-Stokes equations can be written as

$$\left\{S_{ij}\frac{\delta f_j}{\delta w}\right\}^T\frac{\partial\psi}{\partial\xi_i} - {M^{-1}}^T\tilde{L}\psi = 0 \quad \text{in } \mathcal{D}, \tag{2.40}$$

where

$$
\begin{aligned}
(\tilde{L}\psi)_1 &= -\tfrac{p}{\rho^2}\tfrac{\partial}{\partial\xi_l}\left(S_{lj}\kappa\tfrac{\partial\theta}{\partial x_j}\right) \\
(\tilde{L}\psi)_{i+1} &= \tfrac{\partial}{\partial\xi_l}\left\{S_{lj}\left[\mu\left(\tfrac{\partial\phi_i}{\partial x_j}+\tfrac{\partial\phi_j}{\partial x_i}\right)+\lambda\delta_{ij}\tfrac{\partial\phi_k}{\partial x_k}\right]\right\} \\
&+ \tfrac{\partial}{\partial\xi_l}\left\{S_{lj}\left[\mu\left(u_i\tfrac{\partial\theta}{\partial x_j}+u_j\tfrac{\partial\theta}{\partial x_i}\right)+\lambda\delta_{ij}u_k\tfrac{\partial\theta}{\partial x_k}\right]\right\} \\
&- \sigma_{ij}S_{lj}\tfrac{\partial\theta}{\partial\xi_l} \qquad\qquad \text{for} \quad i=1,2,3 \\
(\tilde{L}\psi)_5 &= \tfrac{1}{\rho}\tfrac{\partial}{\partial\xi_l}\left(S_{lj}\kappa\tfrac{\partial\theta}{\partial x_j}\right),
\end{aligned}
$$

and $L, \tilde{L}, \text{and} M$ are transformations which relate the conservative variables to the primitive variables. Their explicit form can be found in appendix B.

The form of the adjoint boundary conditions depends on the cost function. Table 2.1 summarizes some of the commonly used cost functions.

Table 2.1: Adjoint boundary conditions for various cost functions

Minimizing	Cost function I	Adjoint B.C.
Drag	$C_D = \int_{\mathcal{B}} q_i\tau_i dS$	$\phi_k = q_k$
Weight	$C_W = \frac{-\beta\, K_{\text{corr,b}}}{cos(\Lambda)^2}\oint_{\mathcal{B}} p(\xi_1,\xi_3)K(\xi_3)S_{22}d\xi_1 d\xi_3 + \frac{K_{\text{corr,s}}}{S\text{ref}}\oint_{\mathcal{B}}\lvert S_{22}\rvert d\xi_1 d\xi_3$	$\psi_{j+1}n_j = \frac{-\beta\, K_{\text{corr,b}}}{cos(\Lambda)^2}Kn_2$
Inverse	$\frac{1}{2}\int_{\mathcal{B}}(p-p_d)^2\, dS$	$\psi_{j+1}n_j = p - p_d$

2.5.3 Combined cost function

Notice that the adjoint equation is linear in ψ and the cost function term only appears at the boundary condition. Therefore when we optimize a combined cost function such as a weighted sumation of drag and weight, we only modify the adjoint boundary

condition. For example, if we choose to minimize

$$I = \alpha_1 C_D + \alpha_2 C_W$$

The adjoint equation still retains the form of equation (2.40) and the adjoint boundary condition becomes

$$\phi_k = \alpha_1 q_k + \alpha_2 \frac{-\beta}{cos(\Lambda)^2} K \delta_{2k}$$

2.6 Optimization technique

General optimization procedures typically involve two steps; calculation of the gradient and line searches along the direction of steepest descent or an improved direction based on an estimation of the Hessian. This method works quite well as long as the cost function can be evaluated easily. This is not the case for the design using the Euler or Navier-Strokes equations. Here we try to minimize the number of evaluations of the cost function.

The adjoint method is a strategy to reduce the cost of the gradient calculation. In order to avoid line searches, we use a continuous descent process with gradient smoothing as presented below.

2.6.1 Continuous descent

The basic idea is to treat the search process as a time dependent process in pseudo time

$$\frac{dS}{dt} = -\mathcal{G}$$

where S is the vector of design variables, as illustrated in the sketch for two design variables in figure 2.4

A sequence of small steps corresponds to a forward Euler discretization in pseudo time

$$S^{n+1} = S^n - \Delta \mathcal{G}^n$$

The continuous descent process can be analyzed as follows [30]. Suppose that the

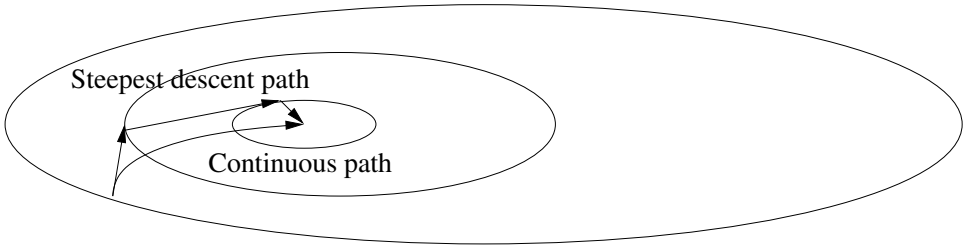

Figure 2.4: Continuous descent for two design variables

optimum is at S^*. Near the optimum the cost I can be represented as

$$I(S) = I(S^*) + \frac{1}{2}(S - S^*)^T A(S - S^*) + \dots$$

where there is no linear term because the gradient $\mathcal{G}(S^*)$ is zero, and A is the Hessian. Also the gradient near the optimum is

$$\mathcal{G}(S) = A(S - S^*) + \dots$$

Thus the continuous process becomes

$$\frac{d}{dt}(S - S^*) = -A(S - S^*)$$

Since A is positive definite at a minimum, it can be expected that

$$A = RMR^T$$

where M is a diagonal matrix of the eigenvalues μ_k and R is a unitary transformation

$$R^T R = RR^T = I$$

Then setting

$$v = R^T(S - S^*)$$

we find that

$$\frac{dv}{dt} = Mv$$

Now the maximum allowable time step is $\Delta t = \frac{2}{\mu_{max}}$ while the rate of decay is dominated by the slowest mode $e^{-\mu_{min}t}$.

In order to improve the rate of convergence we can precondition the descent process as

$$\frac{dS}{dt} = -P\mathcal{G}$$

An ideal preconditioner is the inverse Hessian A^{-1}. However this is prohibitively expensive to calculate. Moreover when it is estimated iteratively from changes in the gradient at each step, as in the well-known quasi Newton methods, we have both to perform exact line searches and to calculate the gradient very accurately.

2.6.2 Gradient smoothing

In fact, the gradient $\mathcal{G}$ obtained from section 2.4 is generally of a lower smoothness class than the shape S. Hence it is important to restore the smoothness. This may be affected by passing this gradient $\mathcal{G}$ to a Sobolev inner product of the form

$$\langle u, v\rangle = \int (uv + \epsilon \frac{\partial u}{\partial \xi}\frac{\partial v}{\partial \xi})\, d\xi$$

This is equivalent to replacing $\mathcal{G}$ by $\bar{\mathcal{G}}$, where in one dimension

$$\bar{\mathcal{G}} - \frac{\partial}{\partial \xi}\epsilon\frac{\partial \bar{\mathcal{G}}}{\partial \xi} = \mathcal{G}, \quad \bar{\mathcal{G}} = \text{zero at end points}$$

and making a shape change $\delta S = -\lambda\bar{\mathcal{G}}$. Then for small positive λ

$$\begin{aligned} \delta I &= -\lambda\langle\bar{\mathcal{G}}, \bar{\mathcal{G}}\rangle \\ &\leq 0 \end{aligned}$$

guaranteeing an improvement.

This gradient smoothing proves to be an effective preconditioner, based on the understanding that the gradient is in a lower smoothness class than the initial geometry. It is shown by Jameson and Vassberg[34] that for problems in the calculus of

variations, it can yield convergence in a number of steps independent of the number of design variables. Moreover the continuous descent process has the advantage that it does not require accurate gradients to achieve an improvement at each step. The descent direction only needs to be within 90 degrees of the true gradient. Thus it is not necessary to solve the flow or the adjoint equations to full convergence at each step. This effectively reduces the optimization to a "one-shot" process.

The efficiency of gradient smoothing stems from the fact that when the mesh points are used as the design variables, they can not be moved independently without violating the requirement of maintaining a smooth shape. Conventional optimization methods, on the other hand, assume that the design variables are completely independent. It appears that gradient smoothing may be a superior method for shape and trajectory optimization problems where smoothness is critical. It should also be noted that this method is based entirely on driving the gradient to zero, and does not directly measure the cost function. It is of course possible that the gradient could reach zero at a local minimum. In two-dimensional optimization studies of airfoils in inviscid transonic flow this never seems to occur, since the drag is almost invariably reduced to zero, corresponding to a shock free shape. In this case the optimum shape is entirely non-unique, and the final optimized shape will depend on the initial shape. In three-dimensional design the possibility of reaching a local minimum which is not the global optimum cannot be ruled out. If this situation is suspected, it may be prudent to start optimizations from alternative initial configurations. As in the two-dimensional case there may also be flat regions of the design space where significantly different shapes have equal performance.

2.7 Discretization of the flow equations

Both the flow and the adjoint equations are discretized using a semi-discrete cell-centered finite volume scheme. The convective fluxes across cell interfaces are represented by simple arithmetic averages of the fluxes computed using values from the cells on either side of the face, augmented by artificial diffusive terms to prevent numerical oscillations in the vicinity of shock waves.

The numerical convective flux across the interface between cells A and B in a three dimensional mesh has the form

$$h_{AB} = \frac{1}{2} S_{AB_j} \left(f_{A_j} + f_{B_j} \right) - d_{AB},$$

where S_{AB_j} is the component of the face area in the j^{th} Cartesian coordinate direction, $\left(f_{A_j}\right)$ and $\left(f_{B_j}\right)$ denote the flux f_j as defined by equation (2.10) and d_{AB} is the diffusive term. To include the viscous terms of the Navier-Stokes equations into the spatial discretization scheme it is necessary to approximate the velocity derivatives $\frac{\partial u_i}{\partial x_j}$ which constitute the stress tensor σ_{ij}. These derivatives may be evaluated by applying Gauss' formula to a control volume V with boundary S.

Throughout this dissertation we use a multistage explicit scheme, belonging to the general class of Runge-Kutta schemes [7]. Rapid convergence to a steady state is achieved via variable local time steps, residual averaging, and a full approximation multi-grid scheme.

The detailed description of the discretization including convergence acceleration techniques such as multi-grid, local time stepping, and residual averaging can be found in appendix A.

2.8 Discretization of the adjoint equations

The adjoint differential equations for the Navier-Stokes formulation have been given by equation (2.40). To find the solution of the adjoint equations, we introduce a time-like derivative term, which will vanish at the steady state solution of equation (2.40). Thus, the adjoint equations (2.40) can be written as

$$\frac{\partial \psi}{\partial t} - C_i^T \frac{\partial \psi}{\partial \xi_i} + M^{-1^T} \tilde{L} \psi = 0 \quad \text{in } \mathcal{D}. \tag{2.41}$$

The main differences between the flow equations and the time-like adjoint equations (2.41) are that the adjoint equations are linear equations and they are not in strong conservation form. However, they correspond closely to the linearized flow equations

with the wave propagating in reverse directions. Thus similar discretization techniques that have been applied earlier to the flow equations can be applied to the adjoint equations. Also similar artificial diffusive terms are introduced in the discretization of the adjoint equation, but with the opposite sign because of the reversal of the the wave directions. The detailed description for the adjoint discretization can also be found in appendix B.

2.9 Flow and adjoint solvers

The baseline flow and adjoint solver used in the discretization are "syn88" and "syn107". These codes were developed by Jameson et.al.[31, 26, 23, 24]. The flow solver solves the three dimensional Euler(syn88) and Navier-Stokes (syn107) equations, by employing the JST scheme[33], together with a multi-step time stepping scheme. Rapid convergence to a steady state is achieved via variable local time steps, residual averaging, and a full approximation multi-grid scheme. The adjoint solver solves the corresponding adjoint equations using similar techniques to those of the flow solver. In fact, much of the software is shared by the flow solver and adjoint solver.

Chapter 3

Implementation

3.1 Design variables

As we discussed in chapter 1, both wing sections (airfoils) and wing planform have a large impact on the drag and weight of the wing. In this dissertation, we employ both wing sections and wing planform as wing design parameters.

3.1.1 Section design variables

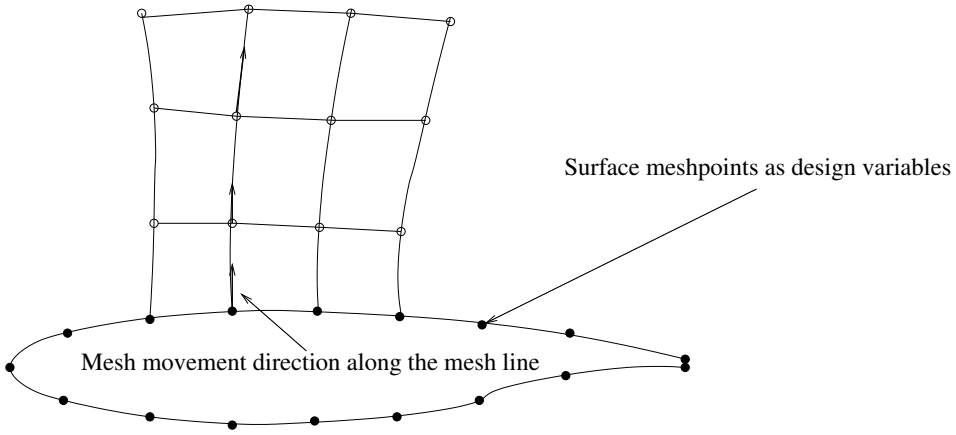

Figure 3.1: Section design variables and mesh movement direction

In computational fluid dynamics, a wing is generally represented by boundary

mesh points. Therefore, the simplest way to select section design variables is to use the surface mesh points on the wing as the design variables. This choice of design variables has an advantage that it does not require surface fitting, such as the spline or polynomial function, which is important when the computational grid is provided without detailed information of how the grid is generated. This type of geometry is call "CAD free" geometry.

Once the gradient information of each point is provided, e.g. by the solution of an adjoint method, we can move the surface points to improve the design. For a small mesh perturbation, which is normally the case for the wing design, it is not necessary to regenerate the mesh. Instead we can perturb it smoothly along the mesh lines emanating from the surface, as shown in figure 3.1. This can avoid cross-over of the perturbed grid.

3.1.2 Planform design variables

From the trade study, the parameters that lead up to a basic design which satisfies the general design criteria include[46]:

- wing shape
- area
- span
- sweep
- aspect ratio
- taper ratio
- airfoil types
- airfoil thickness

Because some of these parameters do not define the wing geometry uniquely, we employ another set of design parameters that still represent these parameters but can be extracted from surface mesh points. In this dissertation we model the wing of interest using six planform variables: root chord (c_1), mid-span chord (c_2), tip chord (c_3), span (b), leading-edge sweep(Λ), and wing thickness ratio (t), as shown in figure 3.2. This choice of design parameters will lead to an optimum wing shape that will not require an extensive structural analysis and can be easily manufactured.

In the industry standard, it may require upto three hundred parameters to completely describe the wing planform. Although we demonstrate our design methodology using the simplified planform, our design method is still applicable to the industry

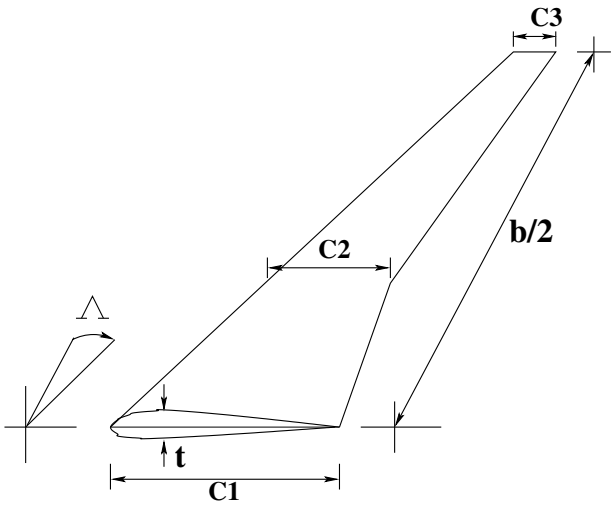

Figure 3.2: Planform design variables

standard because the adjoint method is independent of the number of design variables. Thus our method can be easily extend to cover many parameters without a large increase in computational cost.

3.2 Cost function for planform design

As proposed in section 1.2.4, in this work we minimize the weighted sum of drag and a simplified wing weight

$$I = \alpha_1 C_D + \alpha_3 C_W$$

using the Navier-Stokes equations (NS). However, as we will shown in chapter 4, the computational cost of the design using the NS is one order higher than the design using the Euler equations. The problem comes from the slower rate of convergence due to the limited time step that is required for a highly stress cell to resolve the boundary layer. Moreover the number of computational cells required for the NS calculation are four to five times higher that that of the Euler calculation. One way to reduce the computation cost of the design is to start the optimization using the Euler equation to obtain an intermediate shape. Then we perform the Navier-Stokes

design on this redesigned shape.

However, without the viscosity, the optimization tool can not prevent steep adverse pressure gradient, which will lead to flow separation if the viscosity is present. We add an inverse design term to address this problem. Therefore we optimize

$$I = \alpha_1 C_D + \alpha_2 \frac{1}{2} \int_{\mathcal{B}} (p - p_d)^2 dS + \alpha_3 C_W \tag{3.1}$$

where p_d is the target pressure which can be set by smoothing the existing pressure, and α_1, α_2, and α_3 are weighting constants. The relative importance of drag and weight are represented by the coefficients α_1 and α_3. The choice of these weighting constants is discussed in detail in section 3.6.

3.3 Wing weight estimation

From our discussion in section 2.3, the expression of wing weight contains terms that correspond to bending-load-carrying material and two correction factors; $K_{\text{corr,b}}$ and $K_{\text{corr,s}}$. To estimate these correction factors, we can rewrite the expression (2.21) as

$$\frac{W_{\text{wing}}}{S} = \alpha_1 \frac{W_{\text{b}}}{S} + \alpha_2 \tag{3.2}$$

where W_{wing} is the total weight of the wing, W_{b} is the weight of the wing box, and S is a gross wing area. When there is information from more than two aircraft, we can use the "least-square" curve-fitting strategy to calculate α_1 and α_2. For this dissertation, due to the restricted access to proprietary aircraft weight information, only two sets of data are available; the Boeing 747 and McDonnell Douglas MD-11. However, this is enough estimate the correction factors. The relevant data is shown in table 3.1. In this table, W_{lc} is load-carrying structure. It consists of spar caps, inter-spar coverings, spanwise stiffeners, spar webs, spar stiffeners, and inter-spar ribs. The term W_{b} is our computed bending-carrying material, which is calculated by using CFD. We first compute C_{W_b} of equation (2.19) and then multiply this non-dimensional weight by the free-stream dynamic pressure at 33,000 feet and the corresponding reference area.

Table 3.1: Structural weight data [3]

Aircraft	S (ft^2)	W_{b} (lbs)	W_{lc} (lbs)	W_{wing} (lbs)
B747	5,023	44,705	50,395	88,202
MD11	3,293	33,292	35,157	62,985

Table 3.2: Flight conditions for wing weight estimation

Aircraft	S_{ref} (ft^2)	Mach	C_L	N_{ult}
B747	5,825	.85	.45	3.75
MD11	3,648	.83	.50	3.75

The flight conditions are shown in table 3.2.

By comparing our computed W_{b} with the real weight W_{lc} in table 3.1, we can see that our box-weight estimation is quite close to the load-carrying structure. As expected, we underestimate the box weight because the wing is not fully stressed and our calculation does not account for the weight of spar webs and ribs.

To compute α_1 and α_2, we solve a system of two equations and two unknowns. These equations have the form of equation (3.2) but with different values of $\frac{W_{\mathrm{wing}}}{S}$ and $\frac{W_{\mathrm{b}}}{S}$. This gives

$$\alpha_1 = 1.30 \quad \text{and} \quad \alpha_2 = 6.03 \ \ (lb/ft^2).$$

Compared to reference [37] which gives an estimation of $\alpha_2 = 4.22$, our estimation is

reasonable. However, the total wing weight estimation will be inexact because of the limitation of aircraft number. Finally, $K_{\text{corr,b}}$ and $K_{\text{corr,s}}$ can be computed by

$$K_{\text{corr,b}} = \alpha_1 \quad \text{and} \quad K_{\text{corr,s}} = \frac{\alpha_2}{q_\infty}$$

3.4 Planform gradient calculation

The gradient with respect to planform variation can be computed by integrating point-gradients projected in the planform movement direction. Recall the compact form of the gradient calculation (2.28)

$$\delta I = \int_{\mathcal{B}} \{\delta \mathcal{M}_{II} + \delta \mathcal{N}_{II}\}\, d\mathcal{B}_\xi - \int_{\mathcal{D}} \psi^T \delta R_{II} d\mathcal{D}_\xi$$

where the adjoint variables ψ satisfy the adjoint equation (B.10). The discrete form of this equation is

$$\begin{aligned}
\delta I(w, S) &= \delta I(S) \\
&= \int_{\mathcal{B}} (\delta \mathcal{M}_{II} + \delta \mathcal{N}_{II})\, d\mathcal{B}_\xi - \int_{\mathcal{D}} \psi^T \delta R\, d\mathcal{D}_\xi \\
&\approx \sum_{\mathcal{B}} (\delta \mathcal{M}_{II} + \delta \mathcal{N}_{II})\, \Delta\mathcal{B} - \sum_{\mathcal{D}} \psi^T \Delta \bar{R} \\
&\approx \sum_{\mathcal{B}} (\delta \mathcal{M}_{II} + \delta \mathcal{N}_{II})\, \Delta\mathcal{B} - \sum_{\mathcal{D}} \psi^T \left(\bar{R}|_{S+\delta S} - \bar{R}|_S\right),
\end{aligned}$$

where $\bar{R}|_S$ and $\bar{R}|_{S+\delta S}$ are volume weighted residuals calculated at the original mesh and at the mesh perturbed in the design direction.

Provided that ψ has already been calculated and $\bar{R}$ can be easily calculated, the gradient of the planform variables can be computed effectively by first perturbing all the mesh points along the direction of interest. For example, to calculate the gradient with respect to the sweepback, move all the points on the wing surface as if the wing were pushed backward and also move all other associated points in the

computational domain to match the new location of points on the wing. Then recalculate the residual value and subtract the previous residual value from the new value to form $\Delta\bar{R}$. Finally, to calculate the planform gradient, multiply $\Delta\bar{R}$ by the co-state vector and add the contribution from the boundary terms.

This way of calculating the planform gradient exploits the full benefit of knowing the value of adjoint variables ψ with no extra cost of flow or adjoint calculations.

3.5 Gradient validation

3.5.1 Inviscid planform gradients

To verify the accuracy of the gradients calculated by the method described in section 3.4, we compare these gradients with the gradients computed by the finite-difference method.

For the purpose of this comparison, we fixed angle of attack to eliminate the effect of pitch variation on the gradient. We chose the wing-fuselage of the Boeing 747 at Mach 0.87, and wing angle of attack 2.3 degrees. We performed a design optimization by allowing section changes. At each design iteration, we calculated both the adjoint and finite difference gradients. Figure 3.3 shows one of these computational meshes.

For the finite difference calculation, we used a forward differencing technique with a moderate step size of 0.1% of planform variables to achieve both small discretization error and small cancellation error.

Figures 3.4 and 3.5 show the planform gradient comparison where the cost functions are C_D and C_W respectively. It can be seen that the results from both adjoint and finite difference methods match each other within the 15% error range. This error, especially for the weight sensitivity of sweep changes, arises from the neglected terms at the far-field boundary which we generally assume to be small [36]. More accurate error can be obtained by accounting those terms or enlarging the far field of the computational domain. However, as we will show in the next chapter, these gradients are practical enough to achieve improvements in the design. Nevertheless, this result indicates that the adjoint method provides a moderately accurate planform

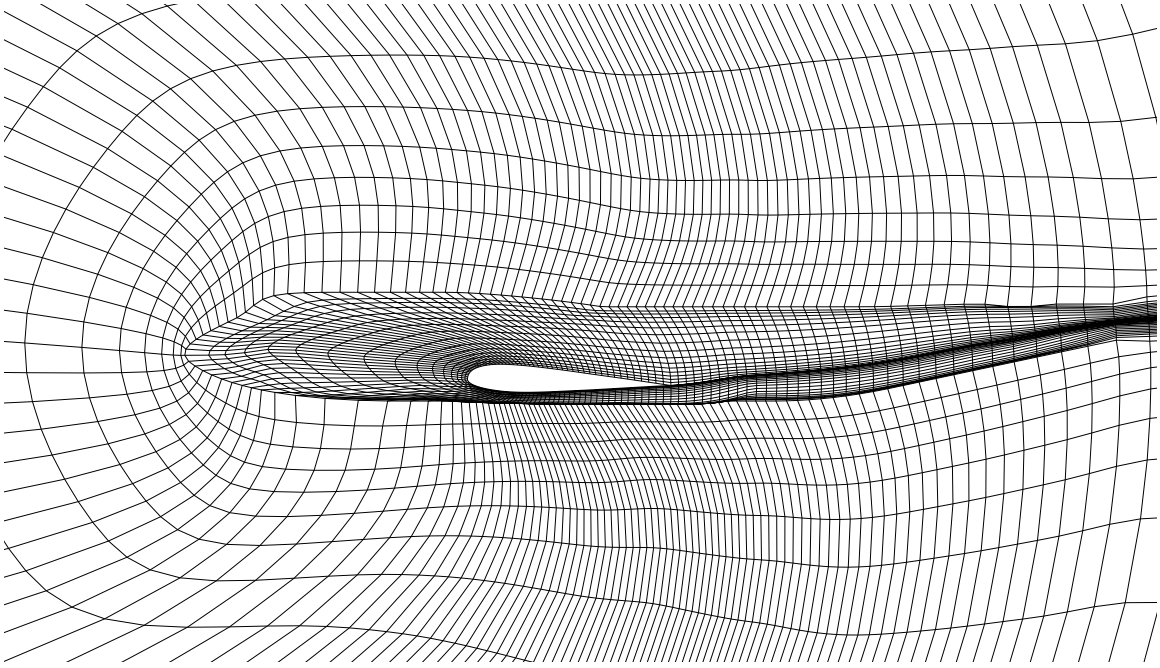

Figure 3.3: Computational grid of the B747 wing fuselage for the Euler calculation

gradient while reducing the computational cost by a factor of the number of design parameters.

3.5.2 Viscous planform gradients

In this section, we performed a similar comparison for the planform viscous gradient. We chose the same Boeing 747 wing-fuselage, but used a four times finer grid to resolve the boundary layer. The size is 256x64x48.

Figure 3.6 plots gradients from the adjoint and finite difference methods for both drag and structural weight. The comparision indicates that the adjoint and finite difference gradients match within the range of %20 error. Compared to the accuray of the inviscid gradient in the previous section, an additional error comes from the accuracy of flow and adjoint solutions. The highly stretch computational cells of the Navier-Stokes design restrict the convergence of the flow solutions to the level that is worse than those of the inviscid solutions. However, this proofs to be good enough for the design purpose.

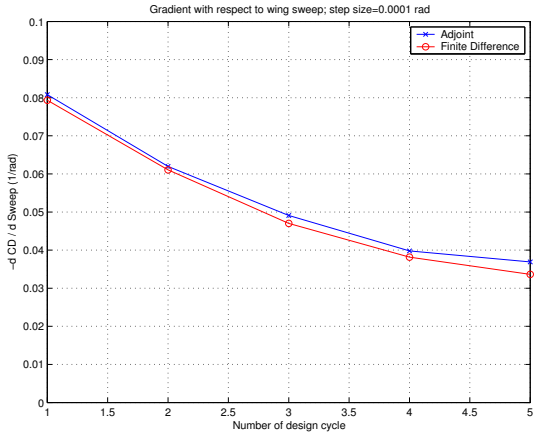

(a) Sweepback Angle Λ.

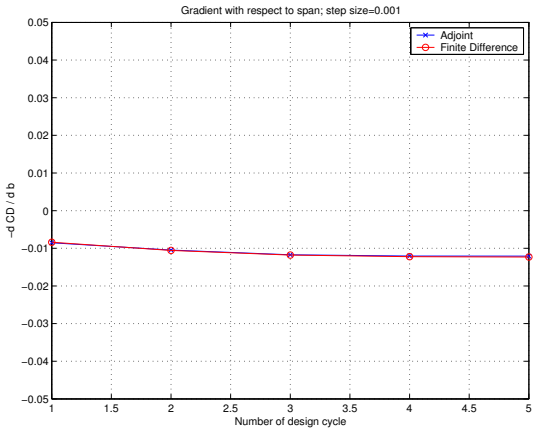

(b) Span b.

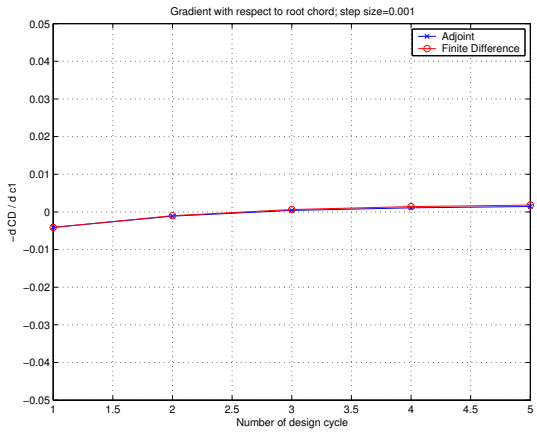

(c) Root chord c_1.

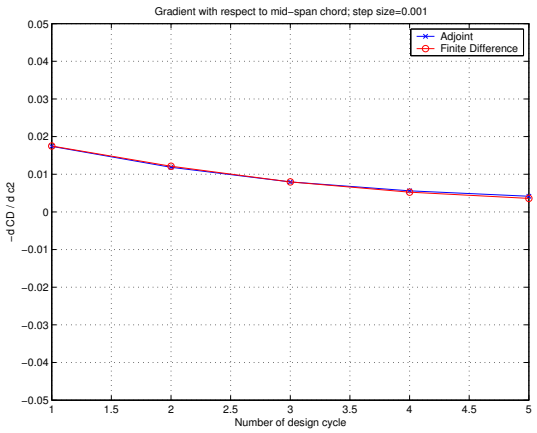

(d) Mid-span chord c_2.

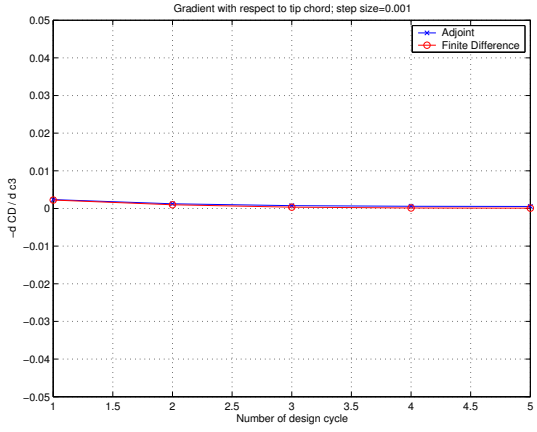

(e) Tip chord c_3.

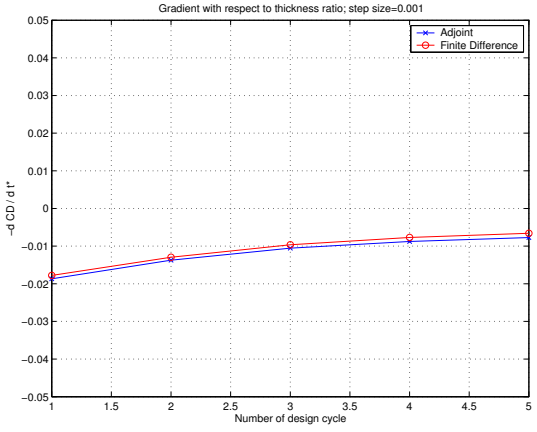

(f) Wing thickness ratio t.

Figure 3.4: Inviscid gradient comparison: drag sensitivities.

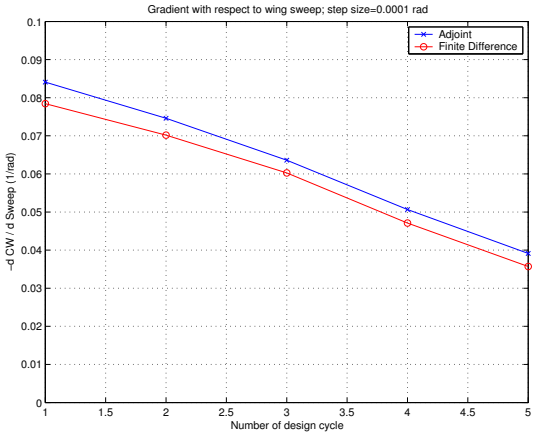

(a) Sweepback Angle Λ.

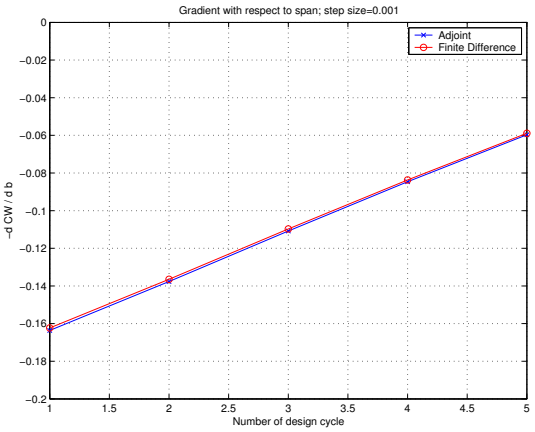

(b) Span b.

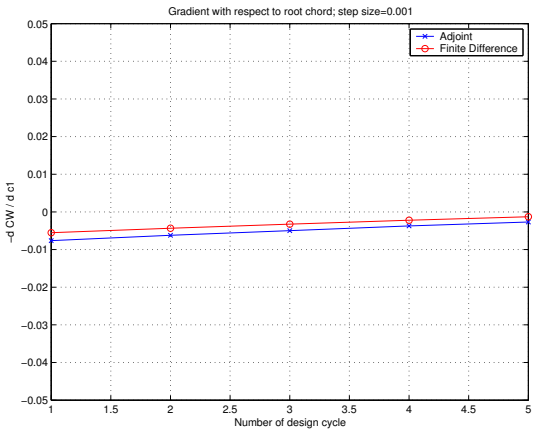

(c) Root chord c_1.

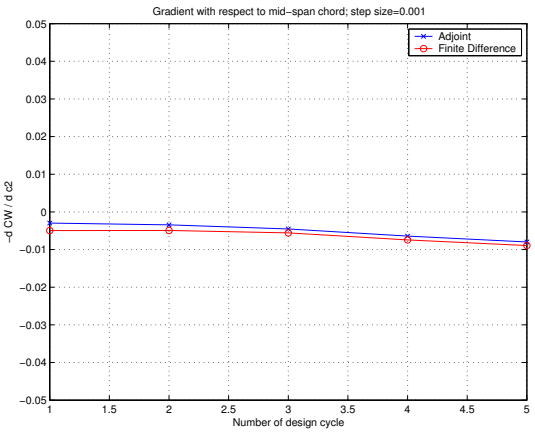

(d) Mid-span chord c_2.

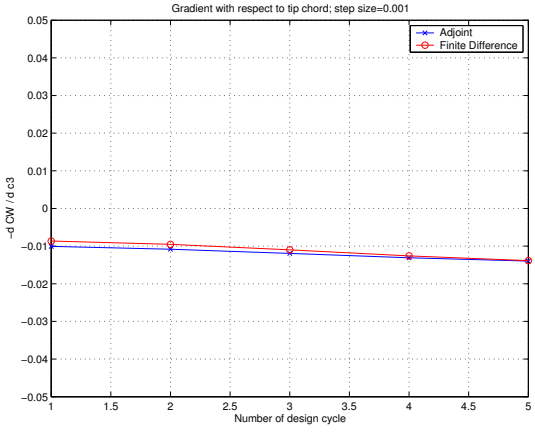

(e) Tip chord c_3.

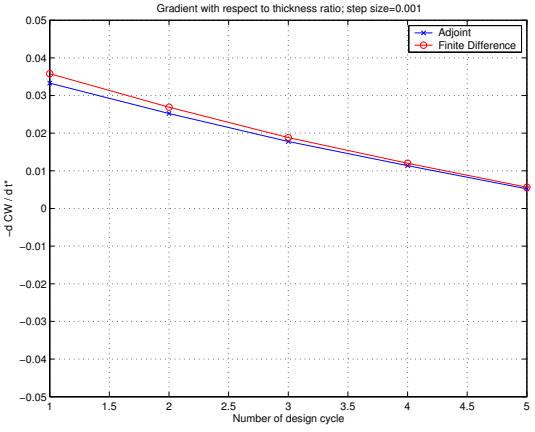

(f) Wing thickness ratio t.

Figure 3.5: Inviscid gradient comparison: wing weight sensitivities.

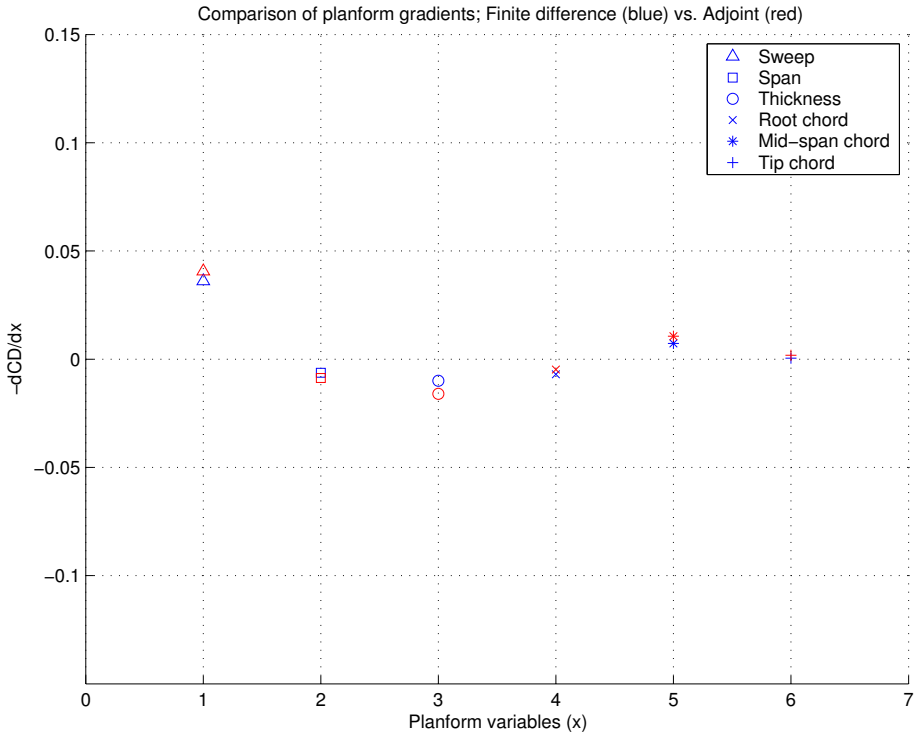

(a) Gradient of C_D

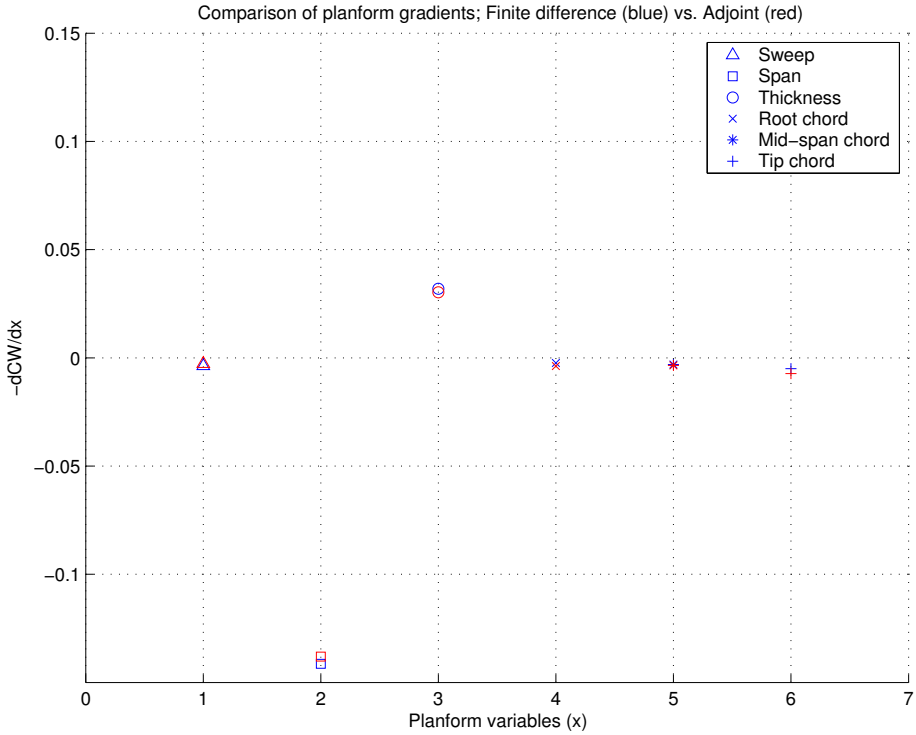

(b) Gradient of C_W

Figure 3.6: Viscous gradient comparison.

3.6 Choice of weighting constants

3.6.1 Maximizing the range of the aircraft

The choice of α_1 and α_3 greatly affects the optimum shape. We can interpret α_1 and α_3 as how much emphases we give to drag and wing weight. If $\frac{\alpha_1}{\alpha_3}$ is high, we focus more on minimizing the drag than the weight and we tend to get an optimum shape that has low C_D but high C_W.

An intuitive choice of α_1 and α_3 can be made by considering the problem of maximizing range of an aircraft. Consider the simplified range equation (1.5)

$$R = \frac{V}{C}\frac{L}{D} ln \frac{W_e + W_f}{W_e}$$

where W_e is the gross weight of the airplane without fuel and W_f is weight of fuel burnt.

If we take

$$\begin{aligned} W_1 &= W_e + W_f = \text{fixed} \\ W_2 &= W_e \end{aligned}$$

then the variation of the weight can be expressed as

$$\delta W_2 = \delta W_e.$$

With fixed $\frac{V}{C}$, W_1, and L, the variation of R can be stated as

$$\begin{aligned} \delta R &= \frac{V}{C}\left(\delta\left(\frac{L}{D}\right) ln\frac{W_1}{W_2} + \frac{L}{D}\delta\left(ln\frac{W_1}{W_2}\right)\right) \\ &= \frac{V}{C}\left(-\frac{\delta D}{D}\frac{L}{D} ln\frac{W_1}{W_2} - \frac{L}{D}\frac{\delta W_2}{W_2}\right) \\ &= -\frac{V}{C}\frac{L}{D} ln\frac{W_1}{W_2}\left(\frac{\delta D}{D} + \frac{1}{ln\frac{W_1}{W_2}}\frac{\delta W_2}{W_2}\right) \end{aligned}$$

and

$$\begin{aligned}\frac{\delta R}{R} &= -\left(\frac{\delta C_D}{C_D} + \frac{1}{ln\frac{W_1}{W_2}}\frac{\delta W_2}{W_2}\right) \\ &= -\left(\frac{\delta C_D}{C_D} + \frac{1}{ln\frac{C_{W_1}}{C_{W_2}}}\frac{\delta C_{W_2}}{C_{W_2}}\right).\end{aligned}$$

If we minimize the cost function defined as

$$I = C_D + \alpha C_W,$$

where α is the weighting multiplication, then choosing

$$\alpha = \frac{C_D}{C_{W_2} ln\frac{C_{W_1}}{C_{W_2}}}, \tag{3.3}$$

corresponds to maximizing the range of the aircraft.

3.6.2 Pareto front

In order to present the designer with a wider range of choices, the problem of optimizing both drag and weight can be treated as a multi-objective optimization problem [8]. In this sense one may also view the problem as a "game", where one player tries to minimize C_D and the other tries to minimize C_W. In order to compare the performance of various trial designs, designated by the symbol X in figure 3.7, they may be ranked for both drag and weight. A design is un-dominated if it is impossible either to reduce the drag for the same weight or to reduce the weight for the same drag. Any dominated point should be eliminated, leaving a set of un-dominated points which form the Pareto front. In figure 3.7, for example, the point Q is dominated by the point P (same drag, less weight) and also the point R (same weight, less drag). So the point Q will be eliminated. The Pareto front can be fit through the points P, R and other dominating points, which may be generated by using an array of different values of α_1 and α_3 in the cost function to compute different optimum shapes. With

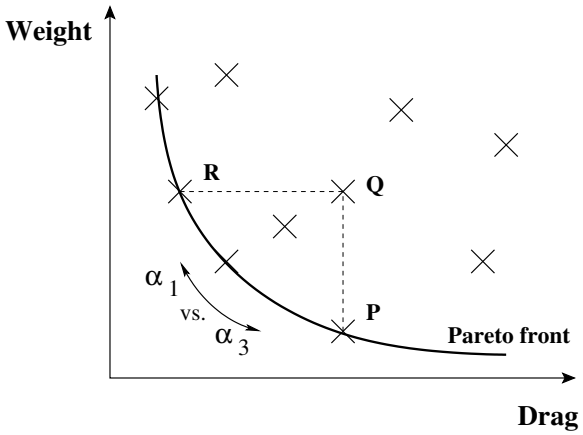

Figure 3.7: Cooperative game strategy with drag and weight as players

the aid of the Pareto front the designer will have freedom to pick the most useful design.

3.7 Design cycle

The design cycle starts by first solving the flow field until at least a 2 order of magnitude drop in the residual. The flow solution is then passed to the adjoint solver. Second, the adjoint solver is run to calculate the costate vector. Iteration continues until at least a 2 order of magnitude drop in the residual. The costate vector is passed to the gradient module to evaluate the aerodynamic gradient. For the pointwise gradients of each surface mesh points, the we calculate the Sobolev gradients and use this Sobolev gradients to update the shape. Then, the structural gradient is calculated and added to the aerodynamic gradient to form the overall gradient. The steepest descent method is used with a small step size to guarantee that the solution will converge to the optimum point. The design cycle is shown in figure 3.8.

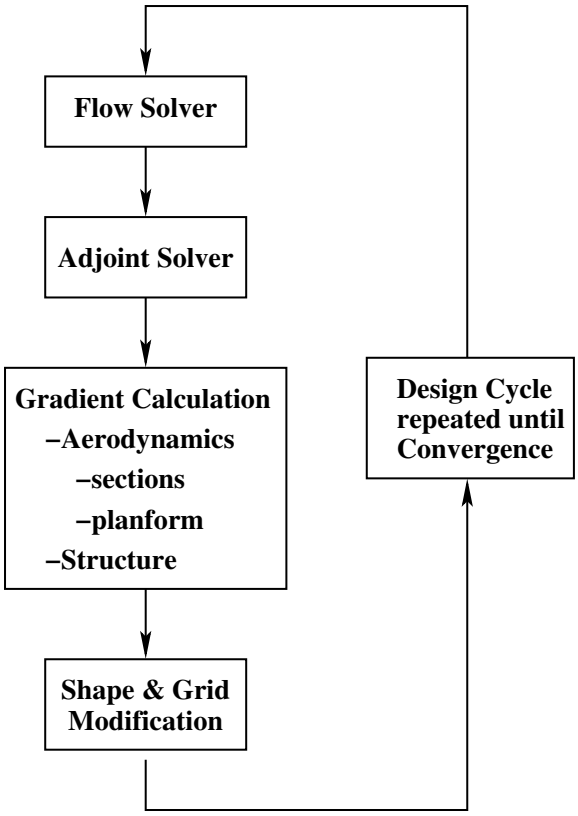

Figure 3.8: Design cycle

Chapter 4

Wing planform optimization results

In this chapter, we present results of the wing planform optimization to show the advantage of integrating shock-free section design with wing planform optimization. The design methodology is defined in chapter 3. We also demonstrate that using trade-offs between aerodynamics and a simplified wing weight model allows us to eliminate the maximum thickness constraints that were required for a pure aerodynamic wing optimization.

The proposed design strategy employs both the Euler and Navier-Stokes optimizations. While the Navier-Stokes equations provide more insight to the flow phenomenon and wing design, the computational cost of the viscous design is an order of magnitude greater than the inviscid design. This is due to several reasons. The number of mesh points must be increased by a factor of four (or more) to resolve the boundary layer. There is also the additional cost of computing the viscous terms and turbulence model. Finally, the Navier-Stokes calculations converge much more slowly than the Euler calculations due to the highly stretch cells used in most models.

Thus, it is more practical and economical to employ the inviscid design tool in flow phenomena where viscous effects are not dominant, e.g. a wing at low angle of attack and high Reynolds number, such as an airplane at cruise condition. This leads us to suggest a time-saving strategy which initiates the viscous design with the

a result from the inviscid design.

4.1 Inviscid redesign of the Boeing 747 wing

We first applied our inviscid design tool to the wing of the Boeing 747. The computational grid was created for the wing fuselage combination as shown in figure 3.3 to provide effects of fuselage disturbance on the wing. On this 192x32x32 grid, the wing sections were represented by 2037 surface mesh points and six planform variables (leading edge sweep, span, chords at three span stations, and wing thickness) are extracted from these mesh points. The redesigns were done at the cruise condition Mach 0.85 and fixed lift coefficient $C_L = 0.45$. Because a planform variation can lead to a variation of wing area, and to avoid any confusion, throughout this dissertation we calculate all the force coefficients such as C_L, C_D, and C_W based on a fixed reference area. Thus a constant C_L implies a constant total lift.

For a reference, we first simulated flow over the baseline wing. The result is shown in figure 4.2. The pressure contours show strong shock waves over the wing, indicated by a region of dense contour lines. These shocks can be eliminated by modifying the wing sections, resulting in a reduction of C_D from 112 counts to 103 counts * while C_W remains constant, as shown in figure 4.3. The capability to redesign for shock free wings has been demonstrated by Jameson[20, 30, 26, 62] during the last decade.

We now extend the redesign to use section changes together with variations of sweep angle, span length, chords, and section thickness simultaneously. The ratio $\frac{\alpha 3}{\alpha_1}$ was chosen according to formula (3.3) such that the cost function corresponds to maximizing the range of the aircraft. Moreover, we eliminated the maximum thickness constraints that were imposed on the previous design.

In twenty-two design iterations the drag coefficient † was reduced from 112 counts to 92.2 counts at the same time the weight C_W was also reduced from 546 counts to 533 counts. The further reduction in drag is the result of the increase in span from 212 ft to 235 ft, which reduces the induced drag. The redesigned geometry also

*1 counts = 0.0001

†C_L, C_D, and C_W are calculated based on the fixed reference area.

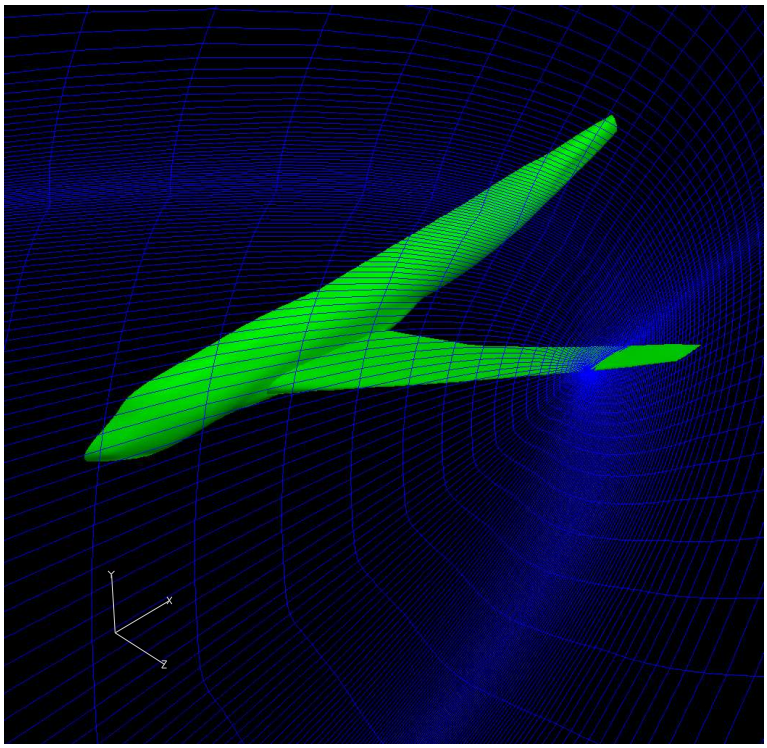

Figure 4.1: C-H grid of the Boeing 747 wing-fuselage.

has a lower sweep angle and a thicker wing section, which both reduce the structural weight, thus compensating for the weight increase due to the increase in span. There was only a slight growth in the chords. This may seem doubtful because without the viscosity there is no strong mechanism to prevent an excessive growth in the chord length. However, if we consider the history of the cost function, there was very slow improvement as the design iterations continued. For a practical purpose, the optimization would cut-off the design iterations when it obtains no significant improvement. This ambiguity does not arise in viscous optimization.

The redesigned geometry is shown in figures 4.4 and 4.5. Overall, the redesign with planform variations gives improvements in both aerodynamic performance and structural weight, compared to the previous

Notice that the only constraints applied here were fixed C_L. There were no constraints on the planform parameters or minimum section-thickness. The design iterations were stopped when there were no appreciable improvements of the cost function, as shown in figure 4.6. This corresponds to the gradient being reduced to such a small value that no significant improvement could be achieved by movement in the negative gradient direction. The redesigned planform still has finite span and its sweep angle is less than 90 degrees. Moreover, the wing sections do not have zero thickness. This result has shown a successful trade-off between the aerodynamics and structures, preventing unrealistic design results.

This inviscid redesigned result in this section can be useful if shock and vortex drag are the main focus of the optimization. The result can also be used as a starting point for viscous optimization.

4.2 General comments for inviscid design

While the inviscid design methods have proven useful for the design of transonic wings at the cruise condition, the required changes in the section shape are comparable in magnitude to the displacement thickness of the boundary layer. The user should also recognize that some flow physics have been neglected and it is important to know the limitations of the design tool.

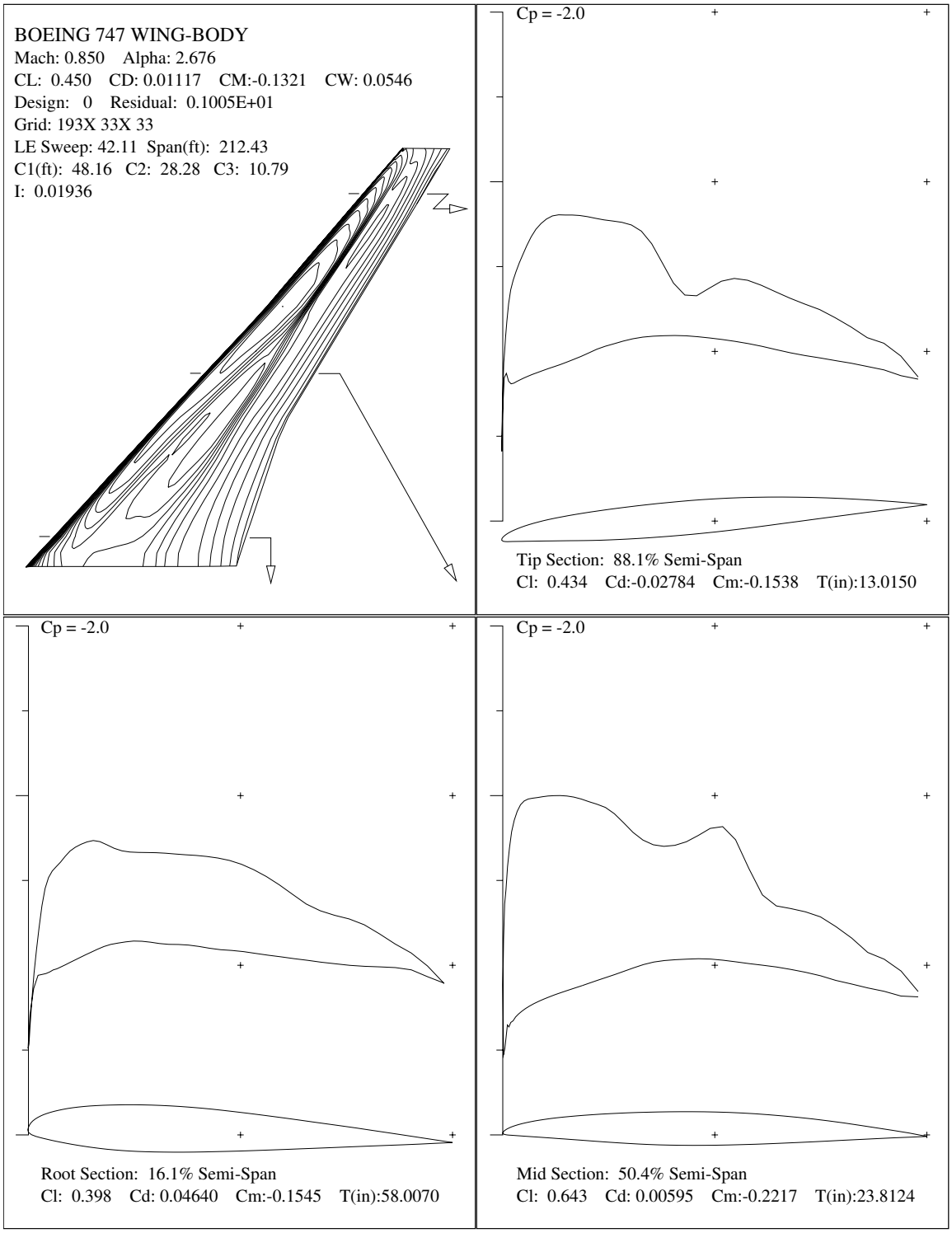

Figure 4.2: Pressure distribution over the baseline Boeing 747 at cruise M .85, using the Euler calculation.

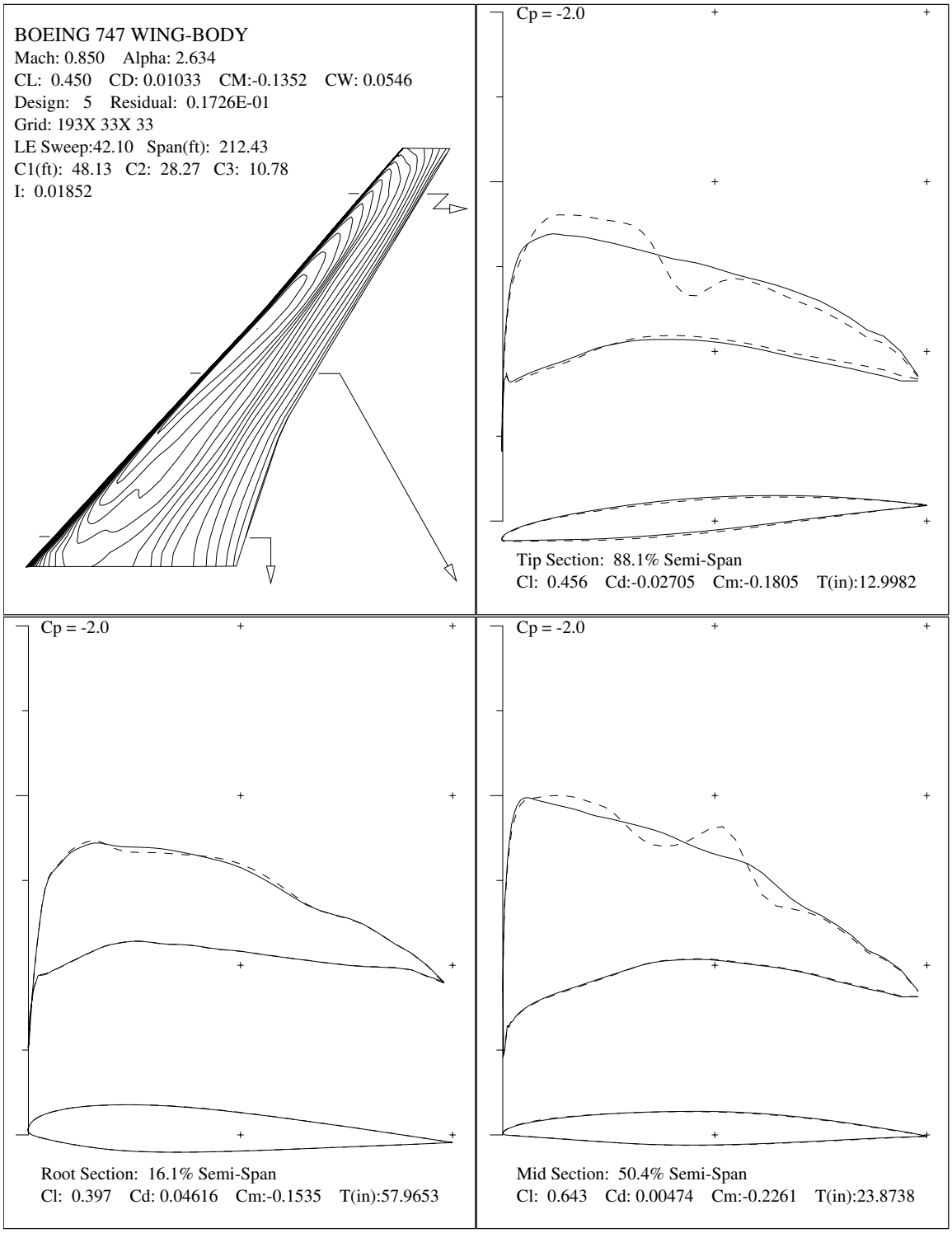

Figure 4.3: Inviscid redesigned wing sections of the Boeing 747 with fixed planform. Dashed and solid lines represent pressure distributions of the baseline Boeing 747 and redesigned configuration respectively.

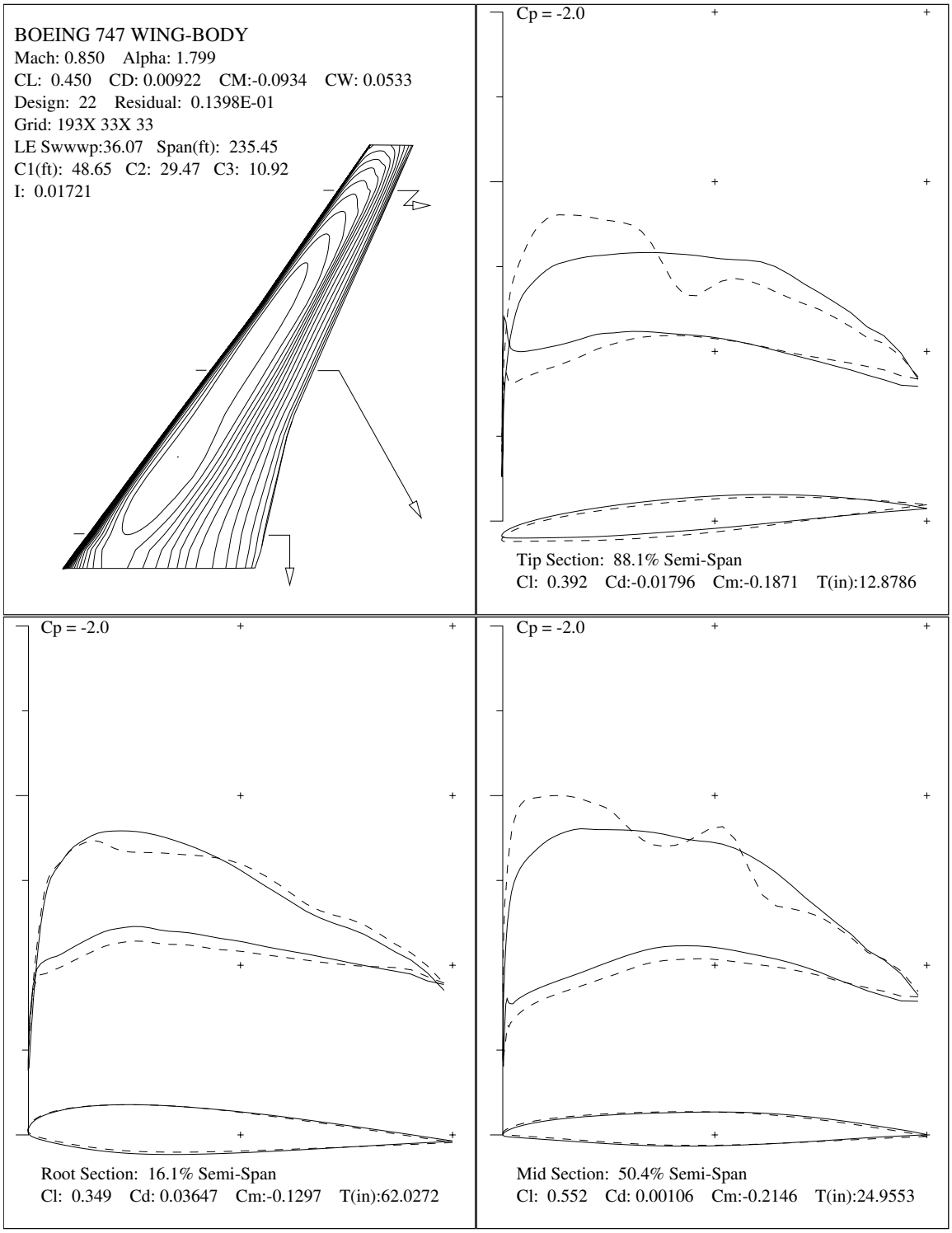

Figure 4.4: Inviscid redesign of both sections and planform of the Boeing 747. Dashed and solid lines represent pressure distributions of the baseline and redesigned configurations respectively.

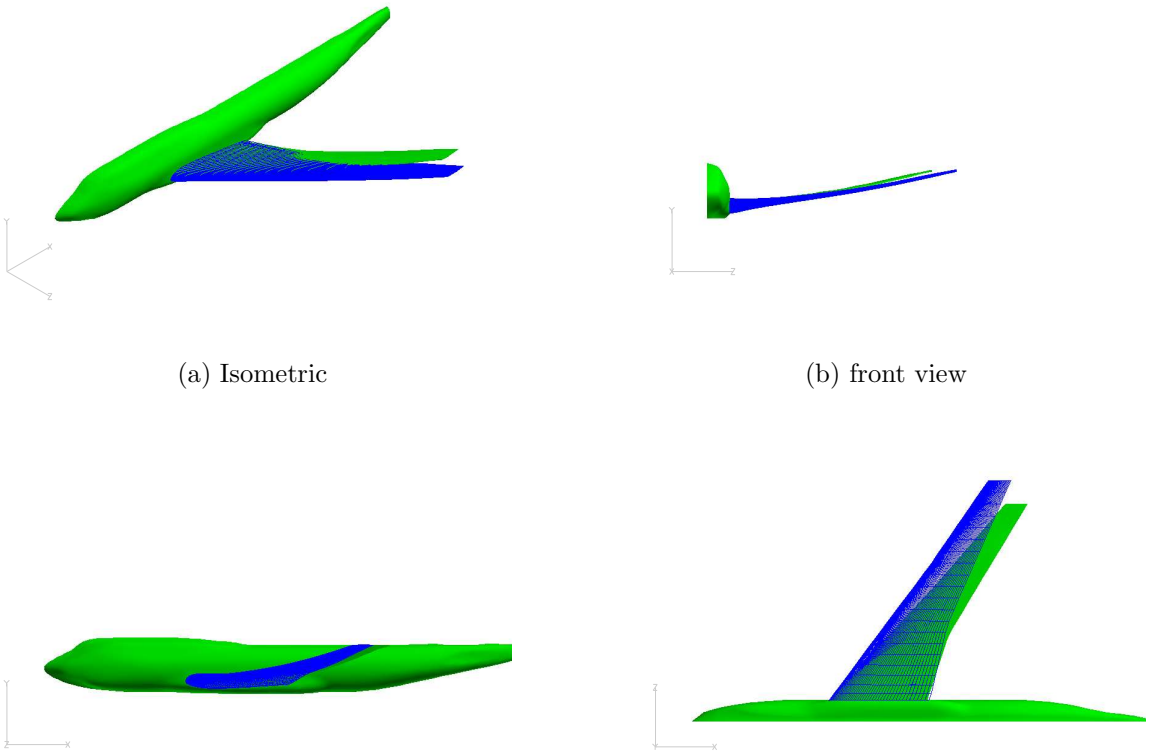

(a) Isometric

(b) front view

(c) side view

(d) top view

Figure 4.5: Geometry changes of the B747 wing using the Euler optimization; baseline (green/light) and redesigned section-and-planform (blue/dark).

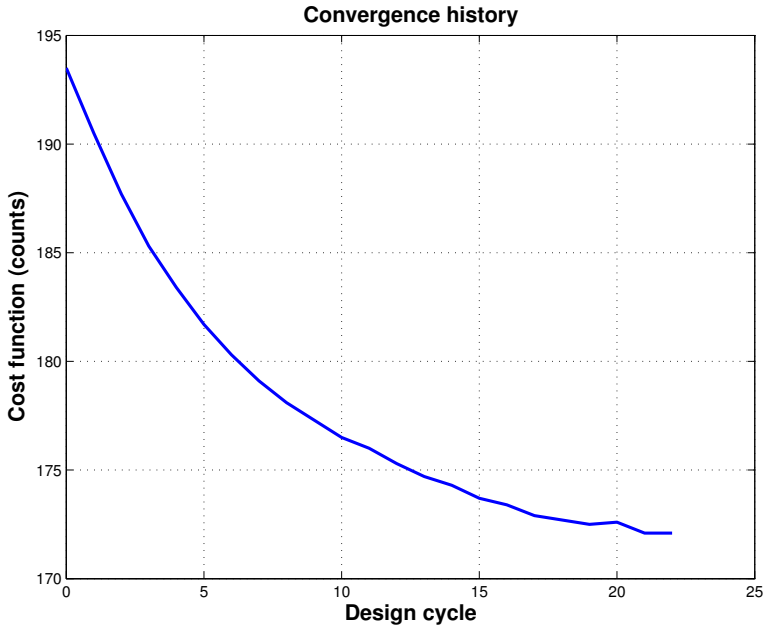

Figure 4.6: History plot of the Boeing 747 planform optimization cost function.

Three concerns missing from the previous case study are discussed here:

- Viscous (skin friction) drag
- Flow separation
- Excessive increment of chords

The redesign result of the Boeing 747 shows large improvement in drag, mostly due to the elimination of shocks and reduction of vortex drag. However, because the design tool was based on the Euler calculation, the skin friction drag has been neglected. It is well known that the skin friction drag is proportional to the wetted area. Thus the redesigned Boeing 747 wing will have higher skin friction drag. In sections 4.3, we will show that the reduction in vortex drag generally outweighs the increase in skin friction drag. Moreover when the viscosity effect is included, the trend of the planform improvements is similar to that for the inviscid calculations.

The second concern deals with flow separation. Although the inviscid calculation can not predict flow separation, the pressure distribution can indicate the risk of the

separation. Near the trailing edge, the flow must decelerate to recover the free stream pressure. In this region of adverse pressure gradient, it is advisable to avoid a design result that has steeper gradients compared to those of the baseline. So, provided that the issue of premature separation is recognized, the inviscid tool can be useful for the wing design problem, especially when fast turn around is an important factor.

The last concern can be recalled in the discussion from section 1.2.2. Without the presence of viscosity, wing area can grow excessively. While the area-dependent term in the weight formula (2.21) may help, the equilibrium point usually has too much area. This did not happen in our inviscid design, mainly because the chord growth rate was very small and the optimizer stopped the design process when no significant improvement is gained. However, if such a case occurs, an additional constraint on maximum chord must be imposed. This could be necessary to allow the wing to fit on the fixed fuselage fairing. However, as we will show in the section 4.1, this did not happen because the slow rate and limitation of mesh movement.

Another great advantage of a design using inviscid calculation is its fast turn-around. A entire design process can be completed within an hour. With the continuing improvement in computer performance, inviscid planform optimization does not require a workstation level of computer. The results shown in section 4.1 were performed on author's laptop in about half an hour. With this advantage, we find another benefit of exploring the design space with inviscid optimization. For example, to validate the results of the Boeing 747 planform design we could perform a series of optimization at fixed different spans, but allowing variations of sweep, thickness, and chords.

The next sections describe a design strategy using the Reynolds Averaged Navier-Stokes (RANS) equations. Viscous design provides increased realism, and alleviates shocks that would otherwise form in the viscous solution over the final inviscid design because of the failure to account for the boundary layer displacement effect. Accurate resolution of viscous effects such as separation and shock/boundary layer interaction is also essential for optimal design encompassing off-design conditions.

4.3 Viscous redesign of the Boeing 747 wing

The design in this section accounts for viscous effects on the design. In these calculations the flow was modeled by the Reynolds Averaged Navier-Stokes equation, with a Baldwin Lomax turbulence model. This turbulence model was considered sufficient because the design point was at cruise condition with attached flow. We investigate the same geometry as in section 4.1, which is the Boeing 747 wing fuselage combination at normal cruising Mach 0.85 and a lift coefficient $C_L = 0.45$. On this 256x64x48 grid, the wing sections were represented by 4224 surface mesh points and six planform variables. Similarly to in the inviscid case, all coefficients are calculated with a fixed reference area based on the initial configuration. Thus an increase in skin friction due to an increase in wetted area will appear as an increase in the friction drag coefficient.

As a reference point, we first modified only the wing sections to eliminate the shock drag, while planform of the baseline B747 was kept unchanged. Figure 4.7 shows the redesigned calculation. Here in 30 design iterations the drag was reduced from 137 counts to 127 counts (7.3% reduction) and the weight remained roughly constant.

We implement both section and planform optimization in viscous design, using the inviscid-redesigned wing shown in figure 4.4 as a starting point. Figure 4.8 shows the effect of allowing changes in sweepback, span, root chord, mid-span chord, and tip chord. The parameter α_3/α_1 was again chosen to maximize the range of the aircraft. In 30 design iterations the drag was reduced to 117 counts (14.5% reduction from the baseline B747), while the dimensionless structure weight was decreased to 516 counts (6.1% reduction), which corresponds to a reduction of 4,800 lbs. The planform changes are shown in figure 4.9. This viscous redesigned wing has less drag and structural weight than the fixed planform viscous redesigned wing.

When we compare this planform with the redesign by inviscid optimization in section 4.1 as shown in figure 4.10, we can see that the effect of viscosity is to shrink the area of the inviscidly redesigned planform. This trend is to be expected because skin friction drag varies roughly linearly with the area. By reducing the area, we can reduce the skin friction drag. Another benefit of using the viscous optimization is

that we can prevent separation. Notice that the steep inverse pressure gradient in figure 4.4 is now removed.

The results from the both inviscid and viscous planform optimizations yield large drag reduction without structural weight penalty in a meaningful way. They show the following basic trends:

- Increase wing span to reduce vortex drag,
- Reduce sweep but increase section-thickness to reduce structural weight,
- Use section optimization to minimize shock drag.

Although the suggested strategy tends to increase the wing area, which increases the skin friction drag, the pressure drag drops at a faster rate, dominating the trade-off. Overall, the combined results yields improvements in both drag and weight.

4.4 Pareto front

The problem of optimizing both drag and weight can be treated as a multi-objective function optimization. A different choice of α_1 and α_3 will result in a different optimum shape. The optimum shapes should not dominate each other, and therefore lie on the Pareto front. The Pareto front can be very useful to the designer because it represents a set which is optimal in the sense that no improvement can be achieved in one objective component that does not lead to degradation in at least one of the remaining components.

Figure 4.11 shows the effect of the weighting parameters (α_1, α_3) on the optimal design. As before, the design variables are sweepback, span, chords, section thickness, and mesh points on the wing surface. In figure 4.11, each point corresponds to an optimal shape for one specific choice of (α_1, α_3). By varying α_1 and α_3, we capture a Pareto front that bounds all the solutions. All points on this front are acceptable solutions, and choosing the final design along this front depends on the nature of the problem and several other factors. The optimum shape that corresponds to the maximum Breguet range is also marked in the figure. In this test case, the Mach

number is the current normal cruising Mach number of 0.85. We allowed section changes together with variations of sweep angle, span length, chords, and section thickness. Figure 4.7 shows the baseline wing. Figure 4.8 shows the redesigned wing. The parameter $\frac{\alpha_3}{\alpha_1}$ was chosen according to formula (3.3) such that the cost function corresponds to maximizing the range of the aircraft. Here, in 30 design iterations the drag was reduced from 137 counts to 117 counts and the structural weight was reduced from 546 counts (88,202 lbs) to 516 counts (83,356 lbs). The large reduction in drag is the result of the increase in span from 212.4 ft to 231.7 ft, which reduces the induced drag. The redesigned geometry also has a lower sweep angle and a thicker wing section in the inboard part of the wing, which both reduce the structural weight. Moreover the section modification prevents the formation of shock. The baseline and redesigned planforms are shown in figure 4.10, together with the planform which resulted from inviscid optimization. Overall, the redesign with variation planform gives improvements in both aerodynamic performance and structural weight, compared to the previous optimization with a fixed planform.

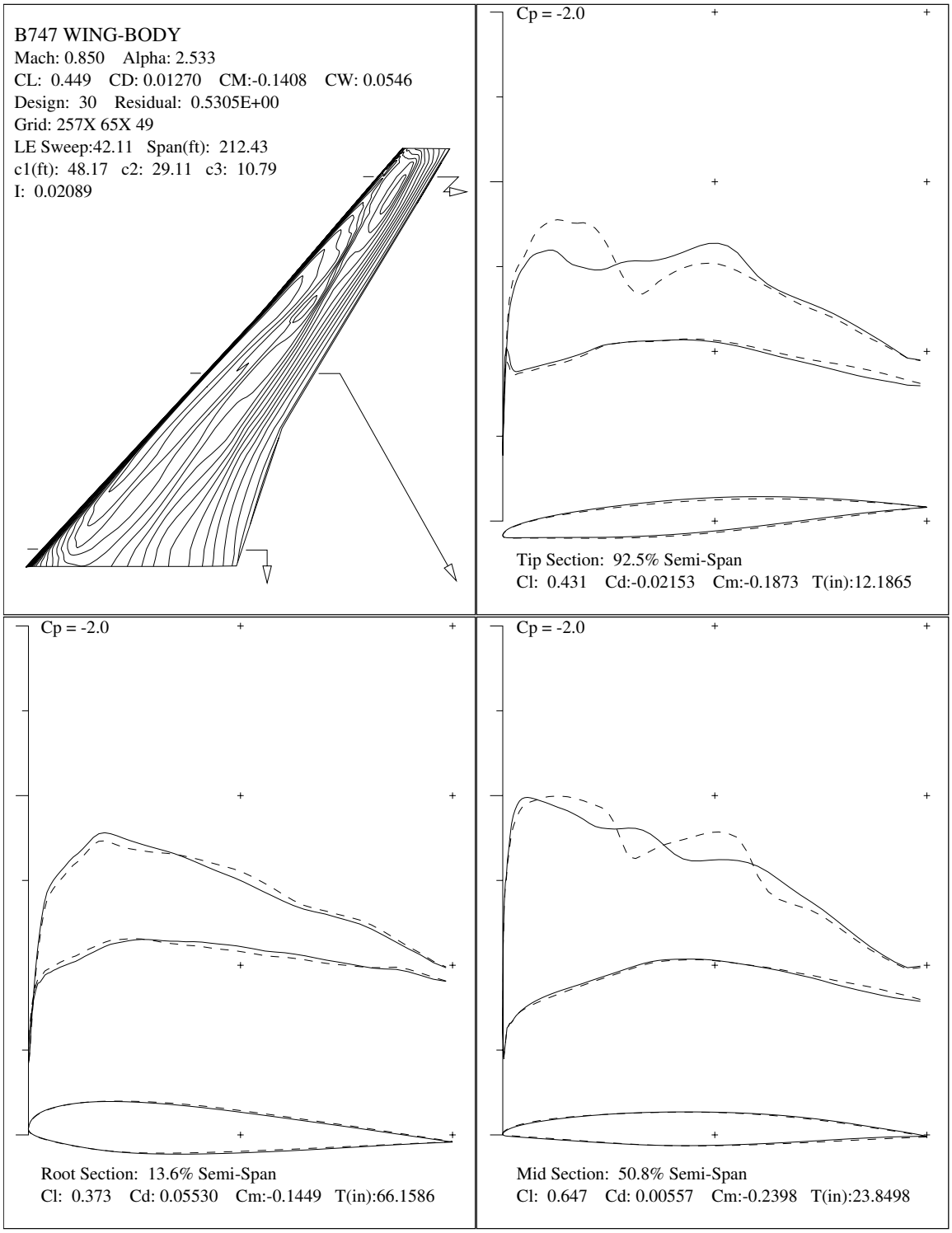

Figure 4.7: Wing-section optimization of Boeing 747 at fixed baseline-planform. Dashed and solid lines represent pressure distributions of the baseline Boeing 747 and redesigned configuration respectively.

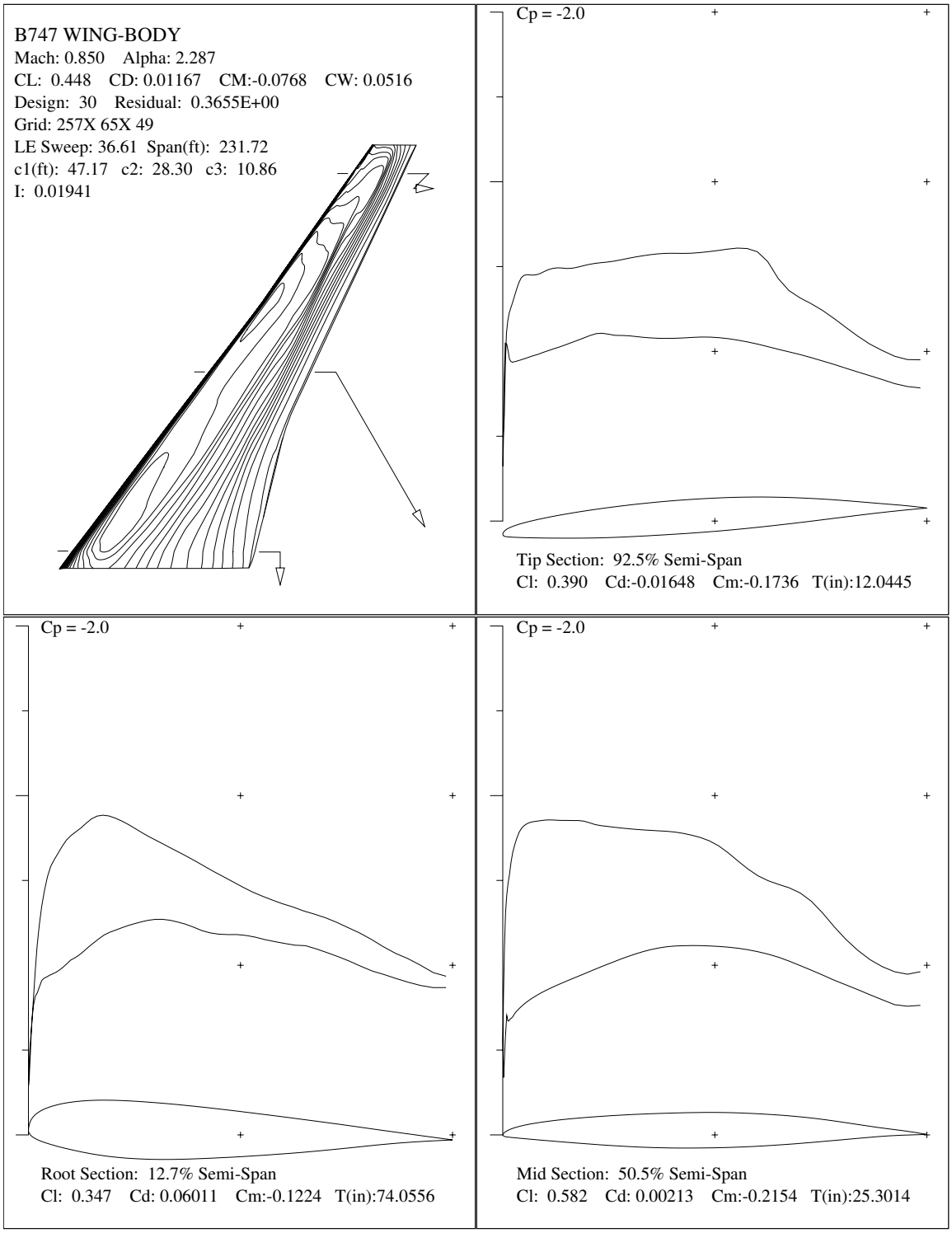

Figure 4.8: Complete optimization of Boeing 747. Both wing-section and planform are optimized to maximize the Breguet range, using inviscid-redesigned planform as a starting points.

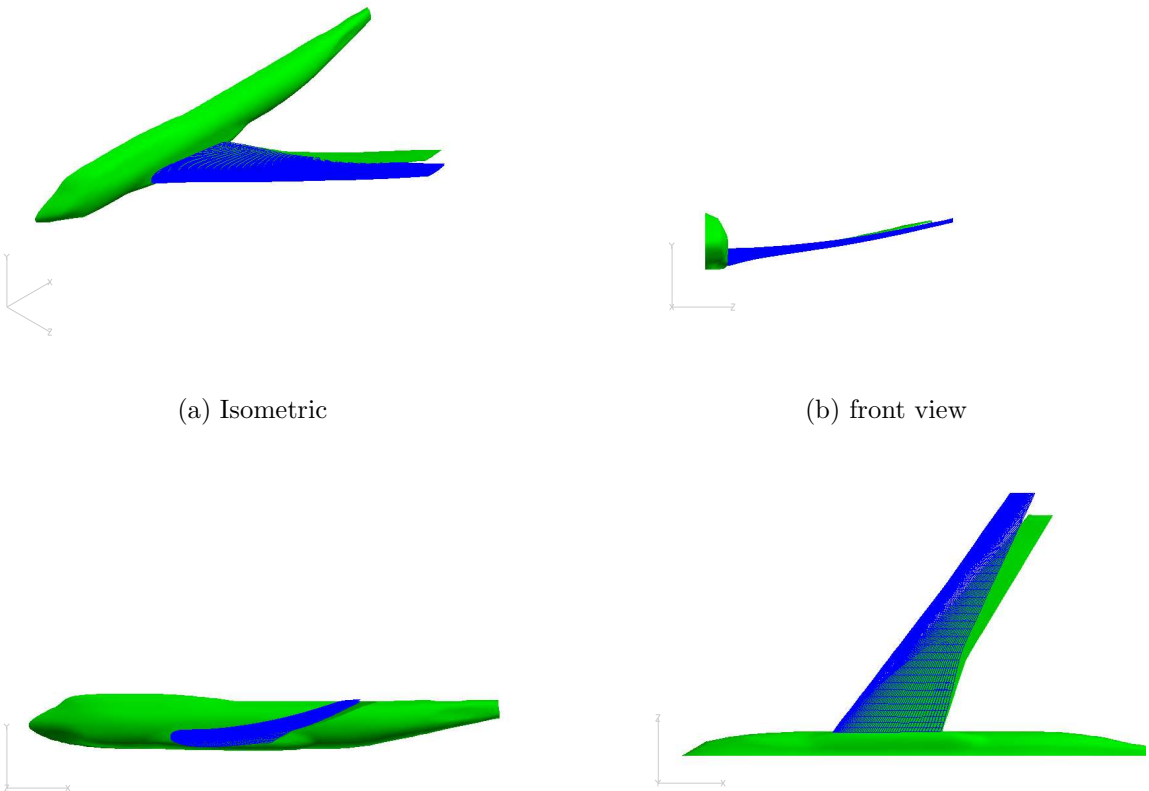

(a) Isometric

(b) front view

(c) side view

(d) top view

Figure 4.9: Geometry changes of the B747 wing using the Navier-Stokes optimization; baseline (green/light) and redesigned section-and-planform (blue/dark).

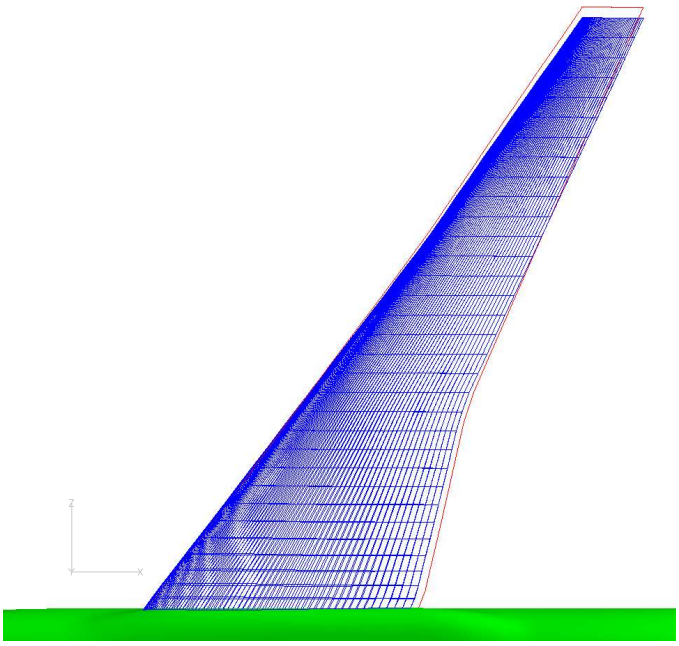

Figure 4.10: Comparison of Euler-redesigned (red) and NS-redesigned planforms (blue). The Euler-redesigned planform has larger area.

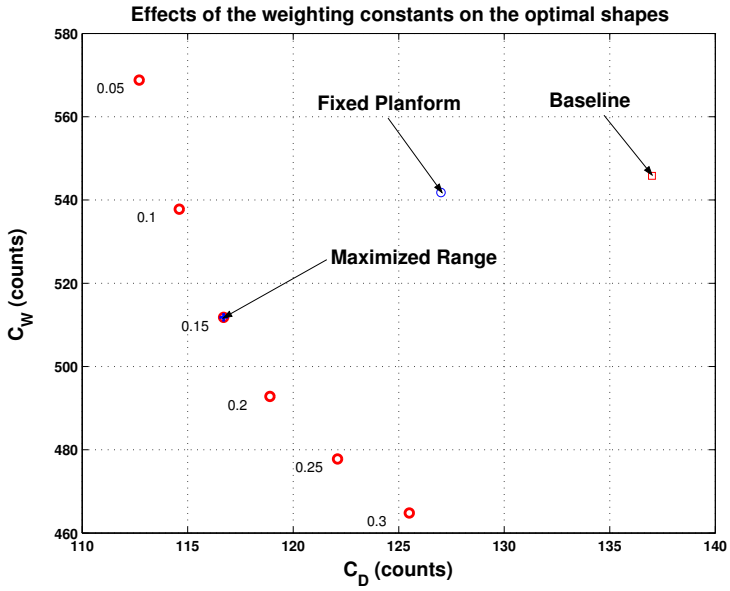

Figure 4.11: Pareto front of section and planform modifications. The ratios of $\frac{\alpha_3}{\alpha_1}$ are marked for each optimal point.

4.5 Viscous redesign of the McDonnell Douglas MD-11 wing

In order to validate the trends suggested by the previous test case, we select another airplane in the long-range transportation category. Here the case chosen is the MD11 wing fuselage combination at cruising Mach number 0.83 and a lift coefficient $C_L = 0.50$.

The baseline and redesigned wings are shown in figures 4.12(a) and 4.12(b) respectively. The geometry changes are shown in figure 4.13. Again, the parameter $\frac{\alpha_3}{\alpha_1}$ was chosen to maximizing the range of the aircraft. In 30 design iterations the drag was reduced from 180 counts to 164 counts, while the wing weight was slightly reduced from 654 counts (62,985 lbs) to 651 (62,696 lbs). Span increases from 174.4 ft to 184.2 ft, sweep slightly reduced from 37.9 to 36.9 degrees, and the section thickness increases. The increase of span reduces vortex drag while the decrease of sweep and the increase of section depth reduce the structural weight. These results are very similar to those obtained for the Boeing 747.

4.6 Viscous redesign of BAe MDO DATUM wing

To further validate this planform-and-section trend, we select the BAe MDO DATUM wing. At its cruising Mach number .85, this wing has low sweep angle and high thickness-to-chord ratio sections.

This test case presents a technical challenge to the optimization because the BAe and B747 are designed to operate at the same flight condition and their planforms are sized closely in the same range. However the original sweep of BAe is already smaller than the optimum sweep of B747 and its wing span is already longer than the optimum span of B747.

Figures 4.14(a), 4.14(b), and 4.15 show the original wing, optimized wing, and their planforms respectively. Despite the low-sweep, long-span, and thick-wing-sections

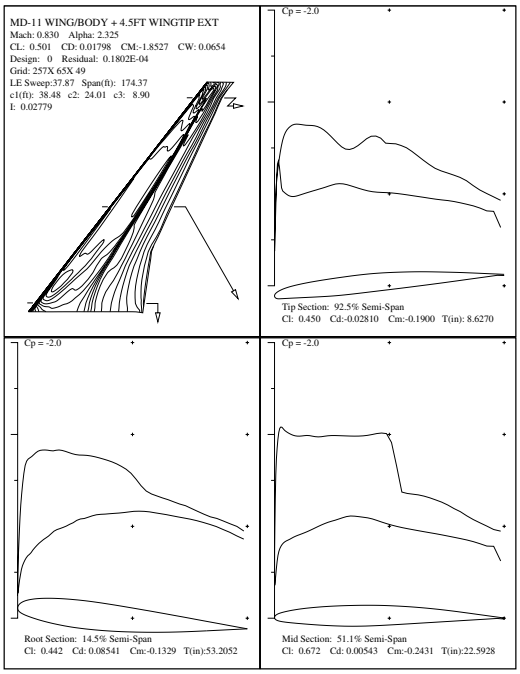

(a) Baseline

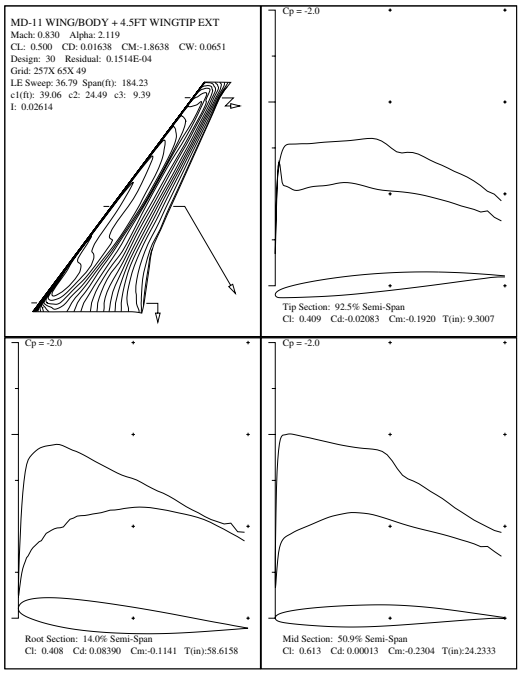

(b) Redesign

Figure 4.12: Pressure distribution of the McDonnell Douglas MD 11 wing.

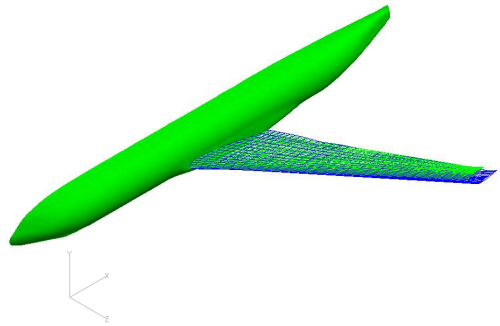

(a) Isometric

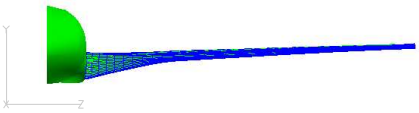

(b) front view

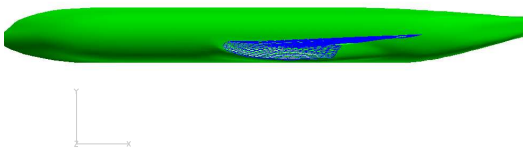

(c) side view

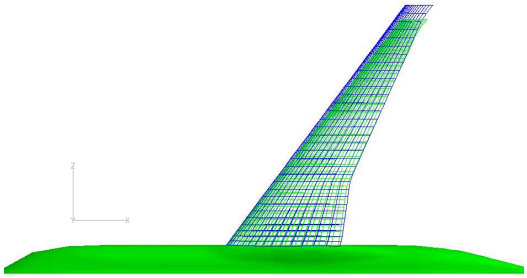

(d) top view

Figure 4.13: Geometry changes of the MD11 wing using the Navier-Stokes optimization; baseline (green/light) and redesigned section-and-planform (blue/dark). The redesigned wing has longer span, less sweep, and thicker wing sections.

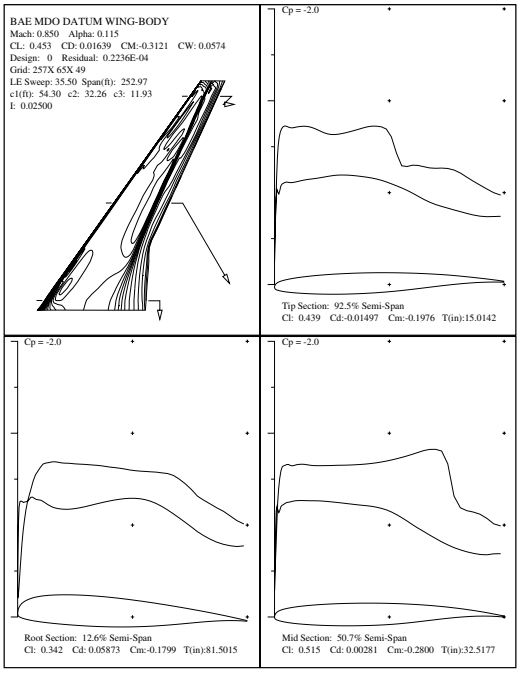

(a) Baseline

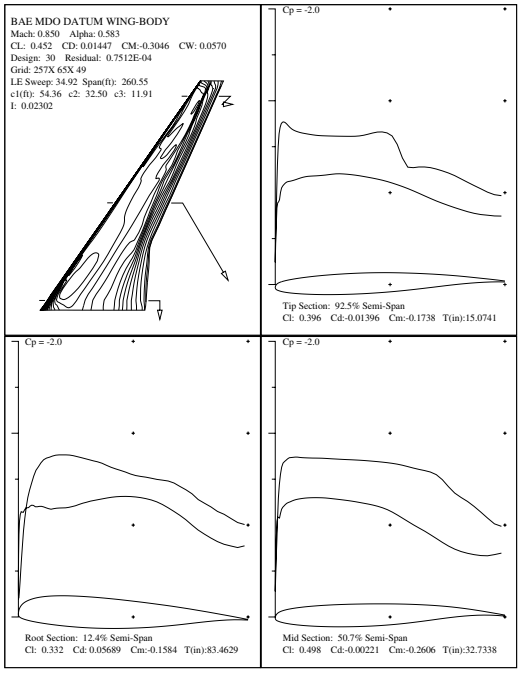

(b) Redesign

Figure 4.14: Pressure distribution of the BAe MDO Datum wing.

of the original wing, the optimal wing has less sweep, longer span, and thicker wing sections. But the changes in the planform are not large. With these changes, the optimum wing shows improvement in both drag and weight. The drag is reduced from 164 counts to 145 counts, and the weight is reduced from 574 counts (87,473 lbs) to 570 counts (86,863lbs). This redesigned BAe wing strongly agrees with the trend suggested from the B747 and MD11 cases.

4.7 Discussion

It can be seen from the results in this chapter that both inviscid and viscous optimizers can improve the performance of the wing by reducing drag without any penalty on the structure weight. The changes that were made to accomplish this were done by the optimizer in a meaningful sense. The weight reduction was the consequence result

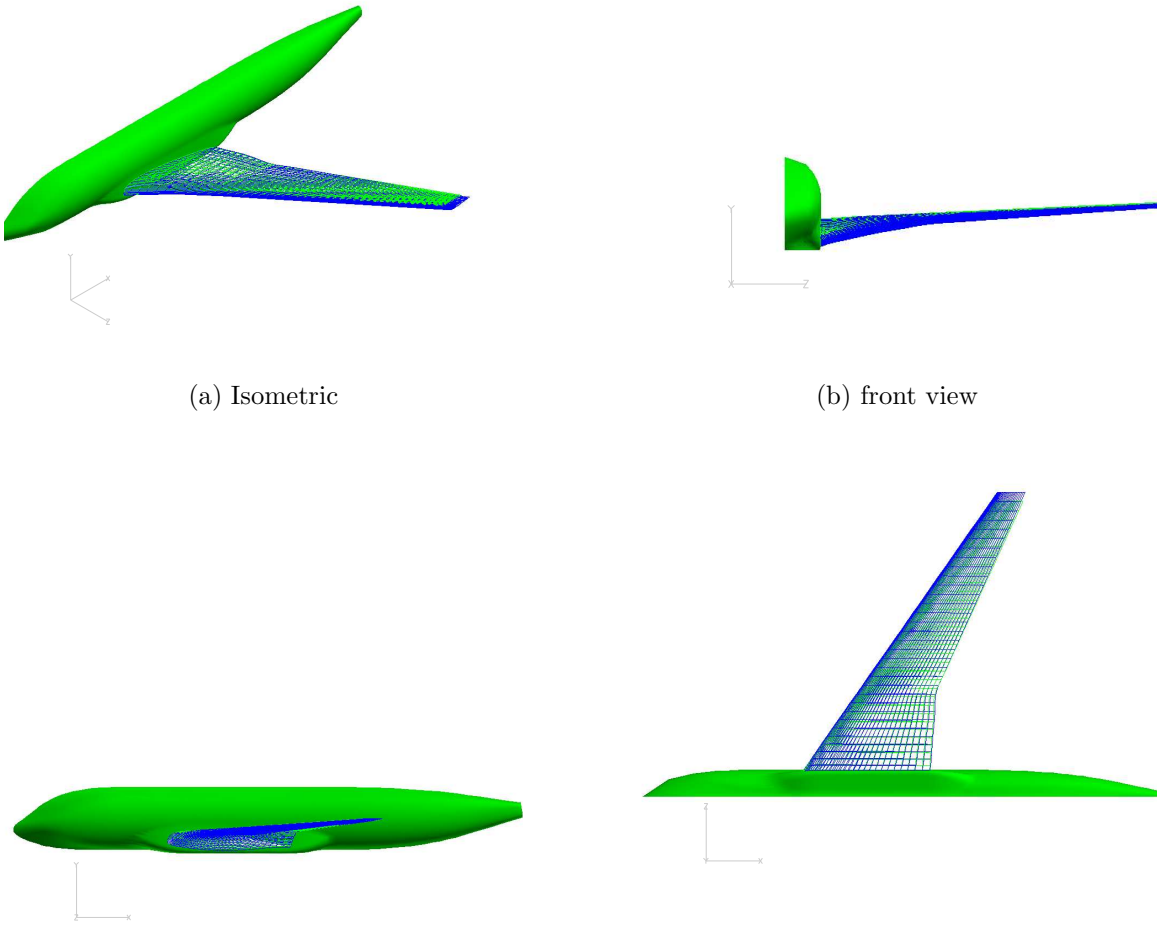

(a) Isometric

(b) front view

(c) side view

(d) top view

Figure 4.15: Geometry changes of the BAe MDO Datum wing using the Navier-Stokes optimization; baseline (green/light) and redesigned section-and-planform (blue/dark). The redesigned wing has longer span, slightly less sweep, and thicker wing sections.

of sweep reduction and thicker wing section. The drag reduction was the result of weakened shock wave and weaker induced drag. These planform changes move in the same direction, however at different magnitude. In the case of the Boeing 747, we see large changes. These changes get smaller for the BAe wing. The Boeing 747 wing was designed during the 1970s, while the BAe wing was designed during the 1990s. The improvement in the airfoil technology definitely makes the wing better. Therefore, the improvement we can achieve should be less for a newer wing. Our optimizer confirms this expectation.

Chapter 5

Conclusion

This dissertation focuses on the problem of wing planform optimization for transonic aircraft based on the solution of Computational Fluid Dynamics (CFD) combined with an adjoint-gradient based numerical optimization procedure. It exploits the shock-free-wing technology, extensively developed during the past decade for wing section design, to "cheat" the conventional wisdom of the planform design. The integration of the shock-free concept and planform optimization enables a range of planform configurations previously prohibited by the strong compressibility drag. This extended freedom can lead to a large reduction in both structural weight and the induced drag.

In order to incorporate this idea, we employ the wing planform as well as the wing sections as the design parameters. Because the two relevant disciplines are aerodynamics and weight, we focus on the aerodynamic optimization with a simplified structural weight model, treating a wing as fully-stressed and rigid. This choice of cost function not only increases the reality of the design but also prevents unrealistic results by exposing the trade-off between the aerodynamics and structures. To formulate our design tool, we extend the aerodynamic shape optimization tool that was initially developed for wing section design to include the planform optimization. The original tool was developed by combining CFD with gradient-based numerical optimization, and applied the adjoint formulation to calculate gradients of a large number of design parameters at very low computational cost, allowing the wing be treated as a "free"

surface to achieve a shock-free shape. Then we extend the adjoint method to cover the planform variations and to compute the sensitivities of the structural weight of both the wing section and planform variations.

Results of a variety of long range transports at fixed-altitude cruise conditions indicate that significant improvement in both aerodynamics and structures can be achieved simultaneously. They also reveal a similar trend from these improvements; by utilizing the shock-free concept, the compressibility drag can be weakened and thus the wing does not require as large a sweep or as small a thickness-to-chord ratio as one that is conventionally designed. The sweep reduction and thickness increment help reduce structural weight, which can be traded for a longer span. The increase of span reduces the induced drag, which is a large portion of drag at the cruise condition, and therefore results in large drag reduction without a penalty on the structural weight. Finally, inclusion of the structural weight and area-dependent viscosity prevents any unrealistic result.

This wing planform optimization is the "first step" in the right direction beyond the pure aerodynamic shape optimization using the adjoint method for fixed planform. The proof-of-concept optimal results indicate large improvements for both drag and structural weight. The next step may require the incorporation of a higher-fidelity structural model, which can capture aero-elastic interaction and structure failure, and the implementations of constraints to satisfy performance, stability-and-control, and manufacturing requirements within the design envelope. It is important to note that additional constraints will certainly affect the results presented here. Yet, the design methodology presented in this work provides the basis for an extension to form a more complete wing design tool.

Appendix A

Discretization of the flow equations

The discretization of the spatial operators is accomplished by using a cell-centered finite volume scheme. The flow domain is divided into a large number of small subdomains, and the integral form of the conservation laws

$$\frac{\partial}{\partial t}\int_{\mathcal{D}} \mathbf{w} dV + \int_{\mathcal{B}} \mathbf{F}\cdot d\mathbf{S} = 0$$

is applied to each subdomain. Here $\mathbf{F}$ is the flux appearing in equation (2.15) and $d\mathbf{S}$ is the directed surface element of the boundary $\mathcal{B}$ of the domain $\mathcal{D}$. The use of the integral form has the advantage that no assumption of the differentiability of the solution is implied, with the result that it remains a valid statement for a subdomain containing a shock wave. In general the subdomains could be arbitrary, but in this work we use the hexahedral cells of a body-conforming curvilinear mesh.

To include the viscous terms of the Navier-Stokes equations into the spatial discretization scheme it is necessary to approximate the velocity derivatives $\frac{\partial u_i}{\partial x_j}$ which constitute the stress tensor σ_{ij}. These derivatives may be evaluated by applying Gauss' formula to a control volume V with boundary S:

$$\int_V \frac{\partial u_i}{\partial x_j} dV = \int_S u_i n_j dS \ ,$$

where n_j is the outward normal. For a hexahedral cell this gives

$$\overline{\frac{\partial u_i}{\partial x_j}} = \frac{1}{\mathrm{V}} \sum_{\text{faces}} \overline{u}_i \; n_j \; S \; , \tag{A.1}$$

where $\overline{u}_i$ is an estimate of the average of u_i over the face, n_j is the j^{th} component of the normal, and S is the face area.

Discretization of this type reduce to central differences on a regular Cartesian grid, and in order to eliminate possible odd-even decoupling modes allowed by the discretization of the convective terms, some form of artificial dissipation must be added. Moreover, when shock waves are present, it is necessary to upwind the discretization to provide a non-oscillatory capture of discontinuities. The effects of numerical diffusion, which may be introduced either explicitly to avoid decoupling or implicitly by means of upwind formulas, could adversely impact the overall accuracy of the solution. Thus, extreme care in devising an appropriate numerical diffusion, or upwind method is required. The next section gives some details on the baseline formulation currently implemented in our solvers.

A.1 Upwinding and numerical viscosity

Over the last twenty years, Jameson et.al. have developed a large class of shock capturing schemes including High Resolution Switched, Symmetric Limited Positive (SLIP) and Upstream Limited Positive (USLIP) schemes [22, 23, 68]. SLIP and USLIP schemes were implemented and tested using several forms of flux-splitting including scalar, characteristic, and Convective Upstream Split Pressure (CUSP) schemes. Careful comparisons with analytical results for laminar boundary layers [69] clearly indicate that the limiting process plays a greater role than the flux-splitting in determining the quality of viscous results. However, new trade-offs between the different forms of flux-splitting arise whenever crisp resolution of shocks becomes important.

Roe has shown that characteristic splitting can yield an optimal discrete shock resolution with only one interior point [65]. More recently, Jameson [24] has shown that

a discrete shock structure with a single interior point can, in general, be supported by artificial diffusion which both:

1. produces an upwind flux if the flow is determined to be supersonic through the interface between the left and the intermediate state,

2. satisfies a generalized eigenvalue problem for the exit from the shock.

These two conditions can be satisfied by both the characteristic and CUSP schemes whereas scalar diffusion fails to satisfy the first condition.

At this time CUSP based schemes, which combine perfect one-point shock capturing of stationary shocks with high resolution of boundary layers, are considered to be the best compromise.

For simplicity we consider only the general one dimensional conservation law for a system of equations which can be expressed as

$$\frac{\partial w}{\partial t} + \frac{\partial}{\partial x} f(w) = 0. \tag{A.2}$$

Here the state and the flux vectors are

$$w = \begin{pmatrix} \rho \\ \rho u \\ \rho E \end{pmatrix}, \quad f = \begin{pmatrix} \rho u \\ \rho u^2 + p \\ \rho u H \end{pmatrix},$$

where ρ is the density, u is the velocity, E is the total energy, p is the pressure, and H is the stagnation enthalpy. If γ is the ratio of specific heats and c is the speed of sound then

$$p = (\gamma - 1)\rho \left(E - \frac{u^2}{2} \right)$$
$$c^2 = \frac{\gamma p}{\rho}$$
$$H = E + \frac{p}{\rho} = \frac{c^2}{\gamma - 1} + \frac{u^2}{2}.$$

In a steady flow H is constant. This remains true for the discrete scheme only if the

numerical diffusion is constructed so that it is compatible with this condition.

It is well known that when the flow is smooth it can be represented by the quasi-linear form

$$\frac{\partial w}{\partial t} + A(w)\frac{\partial w}{\partial x} = 0,$$

where $A(w) = \frac{\partial f}{\partial w}$, and the eigenvalues u, $u+c$ and $u-c$ of the Jacobian matrix A are the wave speeds for the three characteristics. Depending on the initial data, there may not be a smooth solution of the conservation law (A.2). Nonlinear wave interactions along converging characteristics may lead to the formation and propagation of shock waves, while contact discontinuities may also appear.

The conservation law (A.2) is approximated over the interval $(0, L)$ on a mesh with an interval Δx by the semi-discrete scheme

$$\Delta x \frac{dw_j}{dt} + h_{j+\frac{1}{2}} - h_{j-\frac{1}{2}} = 0, \tag{A.3}$$

where w_j denotes the value of the discrete solution in cell j, and $h_{j+\frac{1}{2}}$ is the numerical flux between cells j and $j+1$.

The numerical flux can be taken as

$$h_{j+\frac{1}{2}} = \frac{1}{2}(f_{j+1} + f_j) - d_{j+\frac{1}{2}}, \tag{A.4}$$

where f_j denotes the flux vector $f(w_j)$ evaluated for the state w_j, and $d_{j+\frac{1}{2}}$ is a diffusive flux which is introduced to enable the scheme to resolve discontinuities without producing oscillations in the discrete solution.

A rather general form for the diffusive flux is

$$d_{j+\frac{1}{2}} = \frac{1}{2}\alpha_{j+\frac{1}{2}} B_{j+\frac{1}{2}}(w_{j+1} - w_j),$$

where the matrix $B_{j+\frac{1}{2}}$ controls the numerical diffusion and determines the properties of the scheme, and the scaling factor $\alpha_{j+\frac{1}{2}}$ is included for convenience. Notice that since $w_{j+1} - w_j$ approximates $\Delta x \frac{\partial w}{\partial x}$, the diffusive flux introduces an error proportional to the mesh width. Hence all of these schemes will be first order accurate unless

compensating anti-diffusive terms are introduced.

With this notation, scalar diffusion is produced by setting

$$B_{j+\frac{1}{2}} = I, \tag{A.5}$$

while the characteristic upwind scheme is produced by setting

$$B_{j+\frac{1}{2}} = \left|A_{j+\frac{1}{2}}\right| = T\,|\Lambda|\,T^{-1}. \tag{A.6}$$

In equation (A.6), $A_{j+\frac{1}{2}}(w_{j+1}, w_j)$ is an estimate of the Jacobian matrix $\frac{\partial f}{\partial w}$ obtained by Roe linearization, with the property that the equation

$$f_{j+1} - f_j = A_{j+\frac{1}{2}}(w_{j+1} - w_j)$$

is satisfied exactly, and T is a similarity transformation such that

$$A_{j+\frac{1}{2}} = T\Lambda T^{-1}. \tag{A.7}$$

Thus, the columns of T are the eigenvectors of $A_{j+\frac{1}{2}}$, and Λ is a diagonal matrix containing its eigenvalues. The symbol $\left|A_{j+\frac{1}{2}}\right|$ is used to represent the matrix obtained by replacing the eigenvalues by their absolute values.

An intermediate class of schemes which can be formulated by defining the first order diffusive flux as a combination of differences of the state and flux vectors are given by

$$d_{j+\frac{1}{2}} = \frac{1}{2}\alpha^*_{j+\frac{1}{2}} c\,(w_{j+1} - w_j) + \frac{1}{2}\beta_{j+\frac{1}{2}}\,(f_{j+1} - f_j) \tag{A.8}$$

where the factor c is included so that α^* is dimensionless. Schemes of this class are fully upwind in supersonic flow if one takes $\alpha_{j+\frac{1}{2}} = 0$ and $\beta_{j+\frac{1}{2}} = \text{sign}(M)$ when the absolute value of the local Mach number satisfies $|M| > 1$. In order to support a stationary discrete shock structure with a single interior point, α^* and β cannot be chosen independently. It turns out that once α^* is chosen, β is uniquely determined by the equilibrium at the exit of the shock, leading to a one parameter family of

schemes satisfying the relation

$$\alpha^* = (1+\beta)(1-M)$$

when $M > 0$ [24].

A.2 CUSP formulation

Very accurate schemes of this class can be based on a decomposition of the flux vector f obtained by setting

$$f = uw + f_p, \tag{A.9}$$

where

$$f_p = \begin{pmatrix} 0 \\ p \\ up \end{pmatrix}. \tag{A.10}$$

Then

$$f_{j+1} - f_j = \bar{u}\,(w_{j+1} - w_j) + \bar{w}\,(u_{j+1} - u_j) + f_{p_{j+1}} - f_{p_j}, \tag{A.11}$$

where $\bar{u}$ and $\bar{w}$ are the arithmetic averages

$$\bar{u} = \frac{1}{2}\,(u_{j+1} + u_j)\,, \quad \bar{w} = \frac{1}{2}\,(w_{j+1} + w_j)\,.$$

If the convective terms are separated by splitting the flux according to equations (A.9), (A.10) and (A.11), then the total effective coefficient of convective diffusion is

$$\alpha c = \alpha^* c + \beta \bar{u}.$$

The choice $\alpha c = \bar{u}$ leads to low diffusion near a stagnation point, and also leads to a smooth continuation of convective diffusion across the sonic line since $\alpha^* = 0$ and $\beta = 1$ when $|M| > 1$. The scheme must also be formulated so that the cases of $u > 0$ and $u < 0$ are treated symmetrically. Using the notation $M = \frac{u}{c}$, $\lambda^{\pm} = u \pm c$, this

leads to the diffusion coefficients

$$\alpha = |M| \tag{A.12}$$

$$\beta = \begin{cases} +\max\left(0, \frac{u+\lambda^-}{u-\lambda^-}\right) & \text{if } 0 \le M \le 1 \\ -\max\left(0, \frac{u+\lambda^+}{u-\lambda^+}\right)\right) & \text{if } -1 \le M \le 0 \\ \text{sign}(M) & \text{if } |M| \ge 1. \end{cases} \tag{A.13}$$

Near a stagnation point α may be modified to $\alpha = \frac{1}{2}\left(\alpha_0 + \frac{|M|^2}{\alpha_0}\right)$ if $|M|$ is smaller than a threshold α_0. The expression for β in subsonic flow can also be expressed as

$$\beta = \begin{cases} \max(0, 2M-1) & \text{if } 0 \le M \le 1 \\ \min(0, 2M+1) & \text{if } -1 \le M \le 0 \end{cases}$$

Equation (A.13) remains valid when the CUSP scheme is modified as described below to allow solutions with constant stagnation enthalpy. The coefficients $\alpha(M)$ and $\beta(M)$ are displayed in figure A.1 for the case when $\alpha_0 = 0$. The cutoff of β when $|M| < \frac{1}{2}$,

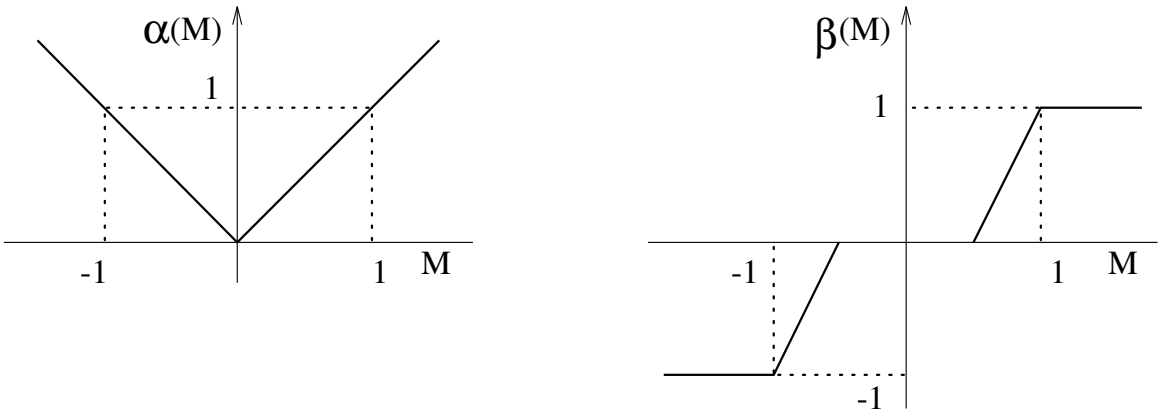

Figure A.1: Diffusion coefficients.

together with α approaching zero as $|M|$ approaches zero, is also appropriate for the capture of contact discontinuities.

An important property of this scheme can be illustrated by introducing a Roe

linearization and by rewriting the diffusive flux as

$$d_{j+\frac{1}{2}} = \frac{1}{2}\left(\alpha^* cI + \beta A_{j+\frac{1}{2}}\right)(w_{j+1} - w_j).$$

Introducing the characteristic decomposition (A.7), the diffusive flux can now be represented as

$$d_{j+\frac{1}{2}} = R\mathcal{M}R^{-1}(w_{j+1} - w_j).$$

The matrix $\mathcal{M}$ is diagonal with eigenvalues $\mu_1 c, \mu_2 c, \mu_3 c$ given by

$$\mu_1 = \alpha - \beta M + \beta M = \alpha = |M|$$

$$\mu_2 = \begin{cases} |M| & \text{if } |M| < \frac{1}{2} \\ \alpha + \beta & \text{if } \frac{1}{2} \leq M \leq 1 \\ |M+1| & \text{if } |M| \geq 1 \end{cases}$$

$$\mu_3 = \begin{cases} |M| & \text{if } |M| < \frac{1}{2} \\ \alpha - \beta & \text{if } \frac{1}{2} \leq M \leq 1 \\ |M-1| & \text{if } |M| \geq 1 \end{cases}$$

These values are displayed in figure A.2.

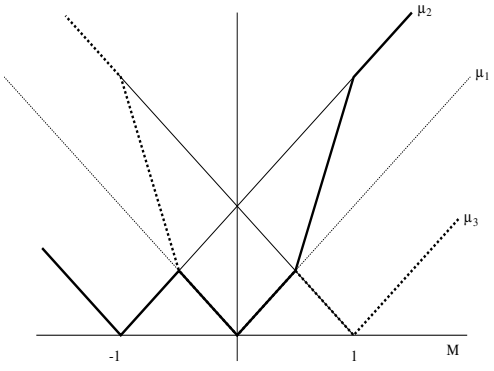

Figure A.2: Eigenvalues of diffusion matrix

In the region $|M| \leq \frac{1}{2}$, $\mu_1 = \mu_2 = \mu_3 = |M|$, while in the region $|M| < 1$ $\mu_2 < |M+1|$, $\mu_3 < |M-1|$. Thus the scheme has lower diffusion than the standard characteristic upwind scheme. Strict positivity is not enforced, but at a shock

$$\Delta f = A\Delta w = \mathcal{S}\Delta w$$

where $\mathcal{S}$ is the shock speed. Thus Δw must be an eigenvector corresponding to one of the eigenvalues $u \pm c$, and positivity is enforced for the corresponding characteristic variable.

In steady flow the stagnation enthalpy H is constant, corresponding to the fact that the energy and mass equations are consistent when the constant factor H is removed from the energy equation. Discrete and semi-discrete schemes do not necessarily satisfy this property. In the case of a semi-discrete scheme expressed in viscosity form - equations (A.3) and (A.4) - a solution with constant H is admitted if the viscosity for the energy equation reduces to the viscosity for the continuity equation with ρ replaced by ρH.

In order to extend the CUSP formulation to allow for isenthalpic solutions, we introduce the linearization

$$f_R - f_L = A_h(w_{h_R} - w_{h_L}),$$

where w_h is a modified state vector with ρH replacing ρE. The matrix A_h may be calculated in the same way as the standard Roe linearization. In particular, by introducing the vector

$$v = \begin{pmatrix} \sqrt{\rho} \\ \sqrt{\rho}u \\ \sqrt{\rho}H \end{pmatrix},$$

all quantities in both f and w_h are products of the form $v_j v_k$ which have the property that a finite difference $\Delta(v_j v_k)$ between left and right states can be expressed as

$$\Delta(v_j v_k) = \bar{v_j}\Delta v_k + \bar{v_k}\Delta v_j$$

where $\bar{v_j}$ is the arithmetic mean $\frac{1}{2}(v_{jR} + v_{jL})$. Therefore,

$$\Delta w = B\Delta v, \;\; \Delta f = C\Delta v = CB^{-1}\Delta w,$$

where B and C can be expressed in terms of appropriate mean values of the quantities v_j. Thus, by defining

$$u = \frac{\sqrt{\rho_R}u_R + \sqrt{\rho_L}u_L}{\sqrt{\rho_R} + \sqrt{\rho_L}}, \;\; H = \frac{\sqrt{\rho_R}H_R + \sqrt{\rho_L}H_L}{\sqrt{\rho_R} + \sqrt{\rho_L}},$$

and

$$c = \sqrt{(\gamma - 1)(H - \frac{u^2}{2})},$$

it follows that

$$A_h = \begin{pmatrix} 0 & 1 & 0 \\ -\frac{\gamma+1}{\gamma}\frac{u^2}{2} & \frac{\gamma+1}{\gamma}u & \frac{\gamma-1}{\gamma} \\ -uH & H & u \end{pmatrix}.$$

The eigenvalues of A_h are u, λ^+ and λ^- where

$$\lambda^{\pm} = \frac{\gamma + 1}{2\gamma}u \pm \sqrt{(\frac{\gamma + 1}{2\gamma}u)^2 + \frac{c^2 - u^2}{\gamma}}. \tag{A.14}$$

Note that λ^+ and λ^- have the same sign as $u + c$ and $u - c$, and change sign at the sonic line $u = \pm c$. The corresponding left and right eigenvectors of A_h can be computed, and are given in [24].

Using the modified linearization the CUSP scheme can be reformulated as follows to admit isenthalpic steady solutions. The diffusive flux is expressed as

$$d_{j+\frac{1}{2}} = \frac{1}{2}\alpha^* c\Delta w_h + \frac{1}{2}\beta\Delta f,$$

where Δ denotes the difference from $j + 1$ to j. The split is redefined as

$$f = uw_h + f_p,$$

where

$$f_p = \begin{pmatrix} 0 \\ p \\ 0 \end{pmatrix}$$

and the diffusive flux can be expressed as

$$d_{j+\frac{1}{2}} = \frac{1}{2}\alpha c \Delta w_h + \frac{1}{2}\beta \bar{w}_h \Delta u + \frac{1}{2}\beta \Delta f_p.$$

As before, α and β are defined by equations (A.12) and (A.13), using the modified eigenvalues $\lambda^{\pm}$ defined in equation (A.14). This splitting corresponds to the Liou-Steffen splitting [44, 71], denoted as H-CUSP formulation.

A.3 Implementation of limiters

In the case of a scalar conservation law, high resolution schemes which guarantee the preservation of the positivity or monotonicity of the solution can be constructed by limiting the action of higher order or anti-diffusive terms, which might otherwise cause extrema to grow. Typically, these schemes compare the slope of the solution at nearby mesh intervals. The fluxes appearing in the CUSP scheme have different slopes approaching from either side of the sonic line, and use of limiters which depends on comparisons of the slopes of these fluxes can lead to a loss of smoothness in the solution at the entrance to supersonic zones in the flow. This problem can be avoided in the implementation of the CUSP schemes by forming the diffusive flux from left and right states at the cell interface. These are interpolated or extrapolated from nearby data, subject to limiters to preserve monotonicity. In a similar manner to the reconstruction of the solution in Van Leer's MUSCL scheme [40], we use the following construction.

Define the limiter

$$R(u, v) = 1 - \left| \frac{u - v}{|u| + |v|} \right|^q, \tag{A.15}$$

where q is a positive power which is set equal to two in the present study. Clearly

$R(u,v) = 0$ when u and v have opposite sign. Also define the limited average

$$L(u,v) = \frac{1}{2}R(u,v)(u+v). \tag{A.16}$$

Let $w^{(k)}$ denote the kth element of the state vector w. Now define left and right states for each dependent variable separately as

$$\begin{aligned} w_L^{(k)} &= w_j^{(k)} + \frac{1}{2}L(\Delta w_{j+\frac{3}{2}}^{(k)}, \Delta w_{j-\frac{1}{2}}^{(k)}) \\ w_R^{(k)} &= w_{j+1}^{(k)} - \frac{1}{2}L(\Delta w_{j+\frac{3}{2}}^{(k)}, \Delta w_{j-\frac{1}{2}}^{(k)}), \end{aligned}$$

where

$$\Delta w_{j+\frac{1}{2}} = w_{j+1} - w_j.$$

Then

$$w_R^{(k)} - w_L^{(k)} = \Delta w_{j+\frac{1}{2}}^{(k)} - L(\Delta w_{j+\frac{3}{2}}^{(k)}, \Delta w_{j-\frac{1}{2}}^{(k)})$$

which in the case of a scalar equation reduces to the SLIP formulation [23].

For the CUSP schemes the pressures p_L and p_R for the left and right states are determined from w_L and w_R. Then the diffusive flux is calculated by substituting w_L for w_j and w_R for w_{j+1} to give

$$d_{j+\frac{1}{2}} = \frac{1}{2}\alpha^* c(w_R - w_L) + \frac{1}{2}\beta(f(w_R) - f(w_L)).$$

The alternative reconstruction:

$$\begin{aligned} w_L^{(k)} &= w_j^{(k)} + R(\Delta w_{j+\frac{3}{2}}^{(k)}, \Delta w_{j-\frac{1}{2}}^{(k)})\Delta w_{j-\frac{1}{2}}^{(k)} \\ w_R^{(k)} &= w_j^{(k)} - R(\Delta w_{j+\frac{3}{2}}^{(k)}, \Delta w_{j-\frac{1}{2}}^{(k)})\Delta w_{j+\frac{3}{2}}^{(k)} \end{aligned}$$

has been found to yield essentially identical results for calculations of steady flows.

A.4 Time stepping scheme

When the space discretization procedure is implemented separately from the discretization in time, it leads to a set of coupled ordinary differential equations which can be written in the form

$$\frac{d\mathbf{w}}{dt} + \mathbf{R}(\mathbf{w}) = \mathbf{0}, \tag{A.17}$$

where $\mathbf{w}$ is the vector of the flow variables at the mesh locations, and $\mathbf{R}(\mathbf{w})$ is the vector of the residuals, consisting of the flux balances defined by the spatial discretization together with the added dissipative terms. If the objective is simply to reach the steady state and details of the transient solution are immaterial, the time-stepping scheme may be designed solely to maximize the rate of convergence.

Throughout this dissertation we use a multistage explicit scheme, belonging to the general class of Runge-Kutta schemes [7]. Schemes of this type have proved very effective for a wide variety of problems, and they have the advantage that they can be applied equally easily on both structured and unstructured meshes [33, 17, 18, 64, 29].

If one reduces the linear scalar model problem corresponding to (A.17) to an ordinary differential equation by substituting a Fourier mode $\hat{w} = e^{ipx_j}$, the resulting Fourier symbol has an imaginary part proportional to the wave speed, and a negative real part proportional to the diffusion. Thus, the time stepping scheme should have a stability region which contains a substantial interval of the negative real axis, as well as an interval along the imaginary axis. To achieve this we treat the convective and dissipative terms in a distinct fashion. Thus, the residual is split as

$$R(w) = Q(w) + D(w),$$

where $Q(w)$ is the convective part and $D(w)$ the dissipative part. Denote the time level $n\Delta t$ by a superscript n. Then the multistage time stepping scheme is formulated

as

$$\begin{aligned} w^{(n+1,0)} &= w^n \\ &\cdots \\ w^{(n+1,k)} &= w^n - \alpha_k \Delta t \left(Q^{(k-1)} + D^{(k-1)} \right) \\ &\cdots \\ w^{n+1} &= w^{(n+1,m)}, \end{aligned}$$

where the superscript k denotes the k-th stage, $\alpha_m = 1$, and

$$\begin{aligned} Q^{(0)} &= Q\left(w^n\right), \quad D^{(0)} = D\left(w^n\right) \\ &\cdots \\ Q^{(k)} &= Q\left(w^{(n+1,k)}\right) \\ D^{(k)} &= \beta_k D\left(w^{(n+1,k)}\right) + (1-\beta_k) D^{(k-1)}. \end{aligned}$$

The coefficients α_k are chosen to maximize the stability interval along the imaginary axis, and the coefficients β_k are chosen to increase the stability interval along the negative real axis.

The coefficients of a five-stage scheme [47] which has been found to be particularly effective are tabulated below.

$$\begin{aligned} \alpha_1 &= \tfrac{1}{4} \quad \beta_1 = 1 \\ \alpha_2 &= \tfrac{1}{6} \quad \beta_2 = 0 \\ \alpha_3 &= \tfrac{3}{8} \quad \beta_3 = 0.56 \\ \alpha_4 &= \tfrac{1}{2} \quad \beta_4 = 0 \\ \alpha_5 &= 1 \quad \beta_5 = 0.44 \end{aligned} \qquad \text{(A.18)}$$

A.5 Convergence acceleration

A.5.1 Multigrid method

Radical improvements in the rate of convergence to a steady-state solution can be realized by the multigrid time-stepping technique. The concept of acceleration by the introduction of multiple grids was first proposed by Fedorenko [9]. There is by now a fairly well-developed theory of multigrid methods for elliptic equations based on treating the updating scheme as a smoothing operator on each grid [5, 12]. This theory, however, does not hold for hyperbolic systems. Nevertheless, it seems that it ought to be possible to accelerate the evolution of a hyperbolic system to a steady state by using large time steps on coarse grids so that disturbances can be more rapidly expelled through the outer boundary. Various multigrid time-stepping schemes designed to take advantage of this effect have been proposed [54, 16, 13, 19, 6, 2, 14, 32, 39].

The multigrid scheme used in this work has been originally developed by Jameson [16] for the Euler equation and then extended to the Navier-Stokes equation by Martinelli and Jameson [48]. This method uses a sequence of coarser meshes generated by eliminating alternate points in each coordinate direction. In order to give a precise description of the multigrid scheme, subscripts may be used to indicate the grid level. Several transfer operations need to be defined. First the solution vector on grid k must be initialized as

$$w_k^{(0)} = T_{k,k-1} w_{k-1},$$

where w_{k-1} is the current value on grid $k-1$, and $T_{k,k-1}$ is a transfer operator. Next it is necessary to transfer a residual forcing function such that the solution on grid k is driven by the residuals calculated on grid $k-1$. This can be accomplished by setting

$$P_k = Q_{k,k-1} R_{k-1}\left(w_{k-1}\right) - R_k\left[w_k^{(0)}\right],$$

where $Q_{k,k-1}$ is another transfer operator. Then $R_k(w_k)$ is replaced by $R_k(w_k) + P_k$

in the time- stepping scheme. Thus, the multistage scheme is reformulated as

$$\begin{aligned} w_k^{(1)} &= w_k^{(0)} - \alpha_1 \Delta t_k \left[R_k^{(0)} + P_k \right] \\ \cdots &\quad \cdots \\ w_k^{(q+1)} &= w_k^{(0)} - \alpha_{q+1} \Delta t_k \left[R_k^{(q)} + P_k \right]. \end{aligned}$$

The resulting $w_k^{(m)}$ then provides the initial data for grid $k+1$. Finally, the accumulated correction on grid k has to be transferred back to grid $k-1$ with the aid of an interpolation operator $I_{k-1,k}$. With properly optimized coefficients, multistage time-stepping schemes can be very efficient drivers of the multigrid process. A W-cycle of the type illustrated in figure A.3 proves to be a particularly effective strategy for

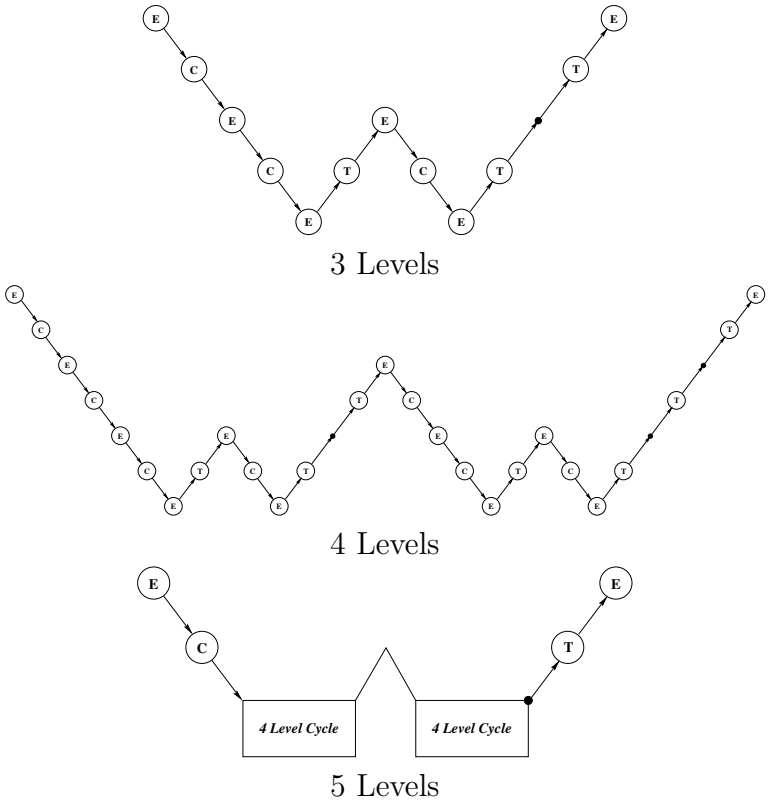

Figure A.3: Multigrid W-cycle for managing the grid calculation. E, evaluate the change in the flow for one step; C, collect the solution; T, transfer the data without updating the solution.

managing the work split between the meshes. In a three-dimensional case the number of cells is reduced by a factor of eight on each coarser grid. Upon examination of the figure, it can therefore be seen that the work measured in units corresponding to a step on the fine grid is on the order of

$$1 + 2/8 + 4/64 + \cdots < 4/3,$$

and consequently the very large effective time step of the complete cycle costs only slightly more than a single time step in the fine grid.

A.5.2 Local time stepping

Once the time step limit for the scheme is estimated, the minimum time step can be used for computations in the flow field. However this choice may not be effective since typical computational meshes used for aerodynamic problems are stretched away from solid surfaces. This problem is particularly severe in grids designed to resolve the viscous phenomena in the boundary layer.

On the other hand, if the final steady state flow field in the limit of large time is the only desired result, then one can choose to advance every computational cell at its own stability limit. This choice frequently leads to faster convergence of both explicit and implicit schemes and has been used for the solution of the steady Euler and Navier-Stokes equations to accelerate the convergence.

A.5.3 Implicit residual smoothing

The rate of convergence of a multistage scheme can also be enhanced by implicit residual smoothing. The general idea behind this technique is to increase the time step limit by replacing the residual at one cell in the flow field by a weighted average of the residuals at the neighboring cells. The average is calculated implicitly and can be expressed in the three-dimensional case:

$$(1 - \epsilon_i \delta_{xx})\,(1 - \epsilon_j \delta_{yy})\,(1 - \epsilon_k \delta_{zz})\,\bar{\boldsymbol{R}}_{i,j,k} = \boldsymbol{R}_{i,j,k}, \tag{A.19}$$

where ϵ_i, ϵ_j, and ϵ_k control the level of smoothing, and $\bar{\boldsymbol{R}}_{i,j,k}$ is the updated value of the residual that is obtained by solving the equation implicitly in each coordinate direction using a tridiagonal solver. A complete discussion of the stability character and overall benefit of this acceleration method is provided by Jameson and Baker [19, 28].

Appendix B

Adjoint equations and discretization

This appendix describes the formulation of the adjoint equations based on control theory for aerodynamic shape design in viscous compressible flow modeled by the Reynolds-Averaged Navier-Stokes(RANS) equations. The extension to aerodynamic shape design with a simplified structural weight is also presented.

The detailed derivation of the adjoint equations and adjoint boundary conditions as developed by Jameson, Martinelli, and Pierce [31] is presented, together with the extension to inclusion analytical structural weight model by Leoviriyakit [41, 42].

B.1 Design using the Navier-Stokes equations

Recall the general formulation for the design using the Euler and Navier-Stokes equation described in section 2.4. Here we minimize the cost function of a boundary integral

$$I = \int_{\mathcal{B}} \mathcal{M}(w, S)\, d\mathcal{B}_\xi + \int_{\mathcal{B}} \mathcal{N}(w, S)\, d\mathcal{B}_\xi \tag{B.1}$$

where $\mathcal{M}(w, S)$ is an aerodynamic cost function, and $\mathcal{N}(w, S)$ is a structure weight. Also, the flow variables w and geometry S satisfy flow equation

$$\frac{\partial}{\partial \xi_i}\left(F_i - F_{vi}\right) = 0. \tag{B.2}$$

which can be regarded as the constraint equation. To eliminate the dependency of flow variations δw from the sensitivity of the cost function δI, we introduce the Lagrange multiplier ψ and integrate over the domain

$$\int_{\mathcal{D}} \psi^T \frac{\partial}{\partial \xi_i} \delta\left(F_i - F_{vi}\right) d\mathcal{D}_\xi = 0. \tag{B.3}$$

Assuming ψ is differentiable, equation (B.3) can be integrated by parts to give

$$\int_{\mathcal{B}} n_i \psi^T \delta\left(F_i - F_{vi}\right) d\mathcal{B}_\xi - \int_{\mathcal{D}} \frac{\partial \psi^T}{\partial \xi_i} \delta\left(F_i - F_{vi}\right) d\mathcal{D}_\xi = 0. \tag{B.4}$$

Using the property that equation (B.4) is equal to zero, it can be subtracted from the variation form of the cost function B.1 without altering the value to give

$$\begin{aligned} \delta I &= \int_{\mathcal{B}} \left[\delta\mathcal{M} + \delta\mathcal{N} - n_i \psi^T \delta\left(F_i - F_{vi}\right)\right] d\mathcal{B}_\xi \\ &+ \int_{\mathcal{D}} \left[\frac{\partial \psi^T}{\partial \xi_i} \delta\left(F_i - F_{vi}\right)\right] d\mathcal{D}_\xi. \end{aligned} \tag{B.5}$$

Since ψ is an arbitrary differentiable function, it can be chosen in such a way that δI no longer depends explicitly on the variation of the state vector δw. The co-state variable ψ then satisfy the adjoint equation

$$\frac{\partial \psi^T}{\partial \xi_i}\left[F_{iw} - F_{viw}\right]_I = 0 \quad \text{in } \mathcal{D}. \tag{B.6}$$

The co-state variable that has this property must also satisfy the adjoint boundary condition

$$n_i \psi^T \left[F_{iw} - F_{viw}\right]_I = \left[\mathcal{M}_w\right]_I + \left[\mathcal{N}_w\right]_I \quad \text{on } \mathcal{B}.$$

The explicit for of the adjoint equation and boundary condition will be shown as follow.

B.2 Adjoint boundary conditions

Due to the additional level of derivatives in the stress and heat flux terms, it is more practical to derive the contributions from the inviscid and viscous terms separately, following the work of Jameson[31].

In order to derive the adjoint equation in detail, equation (B.4) can be expanded as

$$\begin{aligned}
&\int_{\mathcal{B}} \psi^T \left(\delta S_{2j} f_j + S_{2j} \delta f_j\right) d\mathcal{B}_\xi \\
&- \int_{\mathcal{D}} \frac{\partial \psi^T}{\partial \xi_i} \left(\delta S_{ij} f_j + S_{ij} \delta f_j\right) d\mathcal{D}_\xi \\
&- \int_{\mathcal{B}} \psi^T \left(\delta S_{2j} f_{vj} + S_{2j} \delta f_{vj}\right) d\mathcal{B}_\xi \\
&+ \int_{\mathcal{D}} \frac{\partial \psi^T}{\partial \xi_i} \left(\delta S_{ij} f_{vj} + S_{ij} \delta f_{vj}\right) d\mathcal{D}_\xi = 0
\end{aligned} \tag{B.7}$$

It is convenient to assume that the shape modification is restricted to the coordinate surface $\xi_2 = 0$ so that $n_1 = n_3 = 0$, and $n_2 = 1$. Furthermore, it is assumed that the boundary contributions at the far field may either be neglected or else eliminated by a proper choice of boundary conditions as previously shown for the inviscid case [21, 25].

B.3 Derivation of the Inviscid Adjoint Terms

In equation (B.7) the inviscid flux variation can be expanded by setting

$$S_{ij} \delta f_j = S_{ij} \frac{\partial f_j}{\partial w} \delta w.$$

Taking the transpose of equation (B.7), it can be seen that in order to eliminate the explicit dependence on δw in the absence of viscosity effect, ψ should be chosen to

satisfy the inviscid adjoint equation

$$C_i^T \frac{\partial \psi}{\partial \xi_i} = 0 \quad \text{in } \mathcal{D}, \tag{B.8}$$

where the inviscid Jacobian matrices in the transformed space are given by

$$C_i = S_{ij} \frac{\partial f_j}{\partial w}.$$

In order to design a shape which will lead to a desired pressure distribution, the natural choice is to set

$$I = \frac{1}{2} \int_{\mathcal{B}} (p - p_d)^2 \, dS$$

where p_d is the desired surface pressure, and the integral is evaluated over the actual surface area. In the computational domain this is transformed to

$$I = \frac{1}{2} \int\int_{\mathcal{B}_w} (p - p_d)^2 \, |S_2| \, d\xi_1 d\xi_3,$$

where the quantity

$$|S_2| = \sqrt{S_{2j} S_{2j}}$$

denotes the face area corresponding to a unit element of face area in the computational domain. Now, to cancel the dependence of the boundary integral on δp, the adjoint boundary condition reduces to

$$\psi_j n_j = p - p_d \tag{B.9}$$

where n_j are the components of the surface normal, given by:

$$n_j = \frac{S_{2j}}{|S_2|}.$$

This amounts to a transpiration boundary condition on the co-state variables corresponding to the momentum components. Note that it imposes no restriction on the tangential component of ψ at the boundary.

B.4 Derivation of the viscous adjoint equations

The viscous terms are derived below under the assumption that the viscosity and heat conduction coefficients μ and k are essentially independent of the flow, and that their variations may be neglected. This simplification has been successfully used for may aerodynamic problems of interest. However, if the flow variations could result in significant changes in the turbulent viscosity, it may be necessary to account for its variation in the calculation.

The derivation of the viscous adjoint terms can be simplified by transforming to the primitive variables

$$\tilde{w}^T = (\rho, u_1, u_2, u_3, p),$$

because the viscous stresses depend on the velocity derivatives $\frac{\partial u_i}{\partial x_j}$, while the heat flux can be expressed as

$$\kappa \frac{\partial}{\partial x_i}\left(\frac{p}{\rho}\right).$$

where $\kappa = \frac{k}{R} = \frac{\gamma\mu}{Pr(\gamma-1)}$. The relationship between the conservative and primitive variations is defined by the expressions

$$\delta w = M\delta\tilde{w}, \quad \delta\tilde{w} = M^{-1}\delta w$$

which make use of the transformation matrices $M = \frac{\partial w}{\partial \tilde{w}}$ and $M^{-1} = \frac{\partial \tilde{w}}{\partial w}$. These matrices are provided in transposed form for future convenience

$$M^T = \begin{bmatrix} 1 & u_1 & u_2 & u_3 & \frac{u_i u_i}{2} \\ 0 & \rho & 0 & 0 & \rho u_1 \\ 0 & 0 & \rho & 0 & \rho u_2 \\ 0 & 0 & 0 & \rho & \rho u_3 \\ 0 & 0 & 0 & 0 & \frac{1}{\gamma-1} \end{bmatrix}$$

$$M^{-1^T} = \begin{bmatrix} 1 & -\frac{u_1}{\rho} & -\frac{u_2}{\rho} & -\frac{u_3}{\rho} & \frac{(\gamma-1)u_i u_i}{2} \\ 0 & \frac{1}{\rho} & 0 & 0 & -(\gamma-1)u_1 \\ 0 & 0 & \frac{1}{\rho} & 0 & -(\gamma-1)u_2 \\ 0 & 0 & 0 & \frac{1}{\rho} & -(\gamma-1)u_3 \\ 0 & 0 & 0 & 0 & \gamma-1 \end{bmatrix}.$$

The conservative and primitive adjoint operators L and $\tilde{L}$ corresponding to the variations δw and $\delta\tilde{w}$ are then related by

$$\int_{\mathcal{D}} \delta w^T L\psi \; d\mathcal{D}_\xi = \int_{\mathcal{D}} \delta\tilde{w}^T \tilde{L}\psi \; d\mathcal{D}_\xi,$$

with

$$\tilde{L} = M^T L,$$

so that after determining the primitive adjoint operator by direct evaluation of the viscous portion of equation (B.7), the conservative operator may be obtained by the transformation $L = M^{-1^T}\tilde{L}$. Since the continuity equation contains no viscous terms, it makes no contribution to the viscous adjoint system. Therefore, the derivation proceeds by first examining the adjoint operators arising from the momentum equations and then the energy equation. The details may be found in [27].

In order to make use of the summation convention, it is convenient to set $\psi_{j+1} = \phi_j$ for $j = 1, 2, 3$ and $\psi_5 = \theta$. Collecting together the contributions from the momentum and energy equations, the viscous adjoint operator in primitive variables can be finally expressed as

$$\begin{aligned}
(\tilde{L}\psi)_1 &= -\tfrac{p}{\rho^2}\tfrac{\partial}{\partial\xi_l}\left(S_{lj}\kappa\tfrac{\partial\theta}{\partial x_j}\right) \\
(\tilde{L}\psi)_{i+1} &= \tfrac{\partial}{\partial\xi_l}\left\{S_{lj}\left[\mu\left(\tfrac{\partial\phi_i}{\partial x_j}+\tfrac{\partial\phi_j}{\partial x_i}\right)+\lambda\delta_{ij}\tfrac{\partial\phi_k}{\partial x_k}\right]\right\} \\
&+ \tfrac{\partial}{\partial\xi_l}\left\{S_{lj}\left[\mu\left(u_i\tfrac{\partial\theta}{\partial x_j}+u_j\tfrac{\partial\theta}{\partial x_i}\right)+\lambda\delta_{ij}u_k\tfrac{\partial\theta}{\partial x_k}\right]\right\} \\
&- \sigma_{ij}S_{lj}\tfrac{\partial\theta}{\partial\xi_l} \qquad\qquad \text{for} \quad i = 1, 2, 3 \\
(\tilde{L}\psi)_5 &= \tfrac{1}{\rho}\tfrac{\partial}{\partial\xi_l}\left(S_{lj}\kappa\tfrac{\partial\theta}{\partial x_j}\right).
\end{aligned}$$

The conservative viscous adjoint operator may now be obtained by the transformation

$$L = M^{-1^T}\tilde{L}.$$

Finally, the resulting adjoint equations for the Navier-Stokes equations are as follows:

$$C_i^T \frac{\partial \psi}{\partial \xi_i} - M^{-1^T}\tilde{L}\psi = 0 \quad \text{in } \mathcal{D}. \tag{B.10}$$

The first and the second terms come from the convective and diffusive terms of the Navier-Stokes equations respectively. The adjoint equation, a linear set of equations, is solved by marching the co-state variables in time after a time-like derivative has been added.

B.5 Viscous adjoint boundary conditions

The boundary term that arises from the momentum equations including both the δw and δS components equation (B.7) takes the form

$$\int_{\mathcal{B}} \phi_k \delta \left(S_{2j} \left(\delta_{kj} p + \sigma_{kj} \right) \right) d\mathcal{B}_\xi.$$

Replacing the metric term with the corresponding local face area S_2 and unit normal n_j defined by

$$|S_2| = \sqrt{S_{2j} S_{2j}}, \quad n_j = \frac{S_{2j}}{|S_2|}$$

then leads to

$$\int_{\mathcal{B}} \phi_k \delta \left(|S_2| \, n_j \left(\delta_{kj} p + \sigma_{kj} \right) \right) d\mathcal{B}_\xi.$$

Defining the components of the total surface stress as

$$\tau_k = n_j \left(\delta_{kj} p + \sigma_{kj} \right)$$

and the physical surface element

$$dS = |S_2|\, d\mathcal{B}_\xi,$$

the integral may then be split into two components

$$\int_{\mathcal{B}} \phi_k \tau_k \, |\delta S_2| \, d\mathcal{B}_\xi + \int_{\mathcal{B}} \phi_k \delta\tau_k dS, \tag{B.11}$$

where only the second term contains variations in the flow variables and must consequently cancel the δw terms arising in the cost function. The first term will appear in the expression for the gradient.

A general expression for the cost function that allows cancellation with terms containing $\delta\tau_k$ has the form

$$I = \int_{\mathcal{B}} \mathcal{I}(\tau) dS, \tag{B.12}$$

corresponding to a variation

$$\delta I = \int_{\mathcal{B}} \frac{\partial \mathcal{I}}{\partial \tau_k} \delta\tau_k dS,$$

for which cancellation is achieved by the adjoint boundary condition

$$\phi_k = \frac{\partial \mathcal{I}}{\partial \tau_k}.$$

Natural choices for $\mathcal{I}$ arise from force optimization and are a measure of the deviation of the surface stresses from desired target values.

The force in a direction with cosines q_i has the form

$$C_q = \int_{\mathcal{B}} q_i \tau_i dS.$$

If we take this as the cost function (B.12), this quantity gives

$$\mathcal{I} = q_i \tau_i.$$

Cancellation with the flow variation terms in equation (B.11) therefore mandates the

adjoint boundary condition

$$\phi_k = q_k.$$

Note that this choice of boundary condition also eliminates the first term in equation (B.11) so that it need not be included in the gradient calculation.

In the inverse design case, where the cost function is intended to measure the deviation of the surface stresses from some desired target values, a suitable definition is

$$\mathcal{I}(\tau) = \frac{1}{2} a_{lk} \left(\tau_l - \tau_{dl}\right) \left(\tau_k - \tau_{dk}\right),$$

where τ_d is the desired surface stress, including the contribution of the pressure, and the coefficients a_{lk} define a weighting matrix. For flow variation cancellation of

$$\phi_k \delta\tau_k = a_{lk} \left(\tau_l - \tau_{dl}\right) \delta\tau_k$$

we can choose the boundary condition

$$\phi_k = a_{lk} \left(\tau_l - \tau_{dl}\right). \tag{B.13}$$

Assuming arbitrary variations in $\delta\tau_k$, this condition is also necessary.

In order to control the surface pressure and normal stress one can measure the difference

$$n_j \left\{\sigma_{kj} + \delta_{kj} \left(p - p_d\right)\right\},$$

where p_d is the desired pressure. The normal component is then

$$\tau_n = n_k n_j \sigma_{kj} + p - p_d,$$

so that the measure becomes

$$\begin{aligned} \mathcal{I}(\tau) &= \frac{1}{2} \tau_n^2 \\ &= \frac{1}{2} n_l n_m n_k n_j \left\{\sigma_{lm} + \delta_{lm} \left(p - p_d\right)\right\} \left\{\sigma_{kj} + \delta_{kj} \left(p - p_d\right)\right\} \end{aligned}$$

This corresponds to setting

$$a_{lk} = n_l n_k$$

in equation (B.13). Defining the viscous normal stress as

$$\tau_{vn} = n_k n_j \sigma_{kj},$$

the measure can be expanded as

$$\begin{aligned} \mathcal{I}(\tau) &= \frac{1}{2} n_l n_m n_k n_j \sigma_{lm} \sigma_{kj} \\ &\quad + \frac{1}{2} \left(n_k n_j \sigma_{kj} + n_l n_m \sigma_{lm} \right) (p - p_d) \\ &\quad + \frac{1}{2} (p - p_d)^2 \\ &= \frac{1}{2} \tau_{vn}^2 + \tau_{vn} (p - p_d) + \frac{1}{2} (p - p_d)^2 . \end{aligned}$$

For flow variation cancellation of the boundary terms,

$$\phi_k \left(n_j \delta\sigma_{kj} + n_k \delta p \right) = \left\{ n_l n_m \sigma_{lm} + n_l^2 (p - p_d) \right\} n_k \left(n_j \delta\sigma_{kj} + n_k \delta p \right)$$

leads to the boundary condition

$$\phi_k = n_k \left(\tau_{vn} + p - p_d \right).$$

In the case of high Reynolds number, this is well approximated by the equations

$$\phi_k = n_k \left(p - p_d \right), \tag{B.14}$$

which should be compared with the single scalar equation derived for the inviscid boundary condition (B.9). In the case of an inviscid flow, choosing

$$\mathcal{I}(\tau) = \frac{1}{2} (p - p_d)^2$$

requires

$$\phi_k n_k \delta p = (p - p_d)\, n_k^2 \delta p = (p - p_d)\, \delta p$$

which is satisfied by equation (B.14), but represents an over-specification of the boundary condition since only the single condition (B.9) needs to be specified to ensure cancellation.

The form of the boundary terms arising from the energy equation depends on the choice of temperature boundary condition at the wall. For the adiabatic case, the boundary contribution is

$$\int_{\mathcal{B}} k \delta T \frac{\partial \theta}{\partial n} d\mathcal{B}_\xi,$$

while for the constant temperature case the boundary term is

$$\int_{\mathcal{B}} k\theta \left\{ \frac{{S_{2_j}}^2}{J} \frac{\partial}{\partial \xi_2} \delta T + \delta \left(\frac{{S_{2_j}}^2}{J} \right) \frac{\partial T}{\partial \xi_2} \right\} d\mathcal{B}_\xi \ .$$

One possibility is to introduce a contribution into the cost function which depends on T or $\frac{\partial T}{\partial n}$ so that appropriate cancellation would occur. Since there is little physical intuition to guide the choice of such a cost function for aerodynamic design, a more natural solution is to set

$$\theta = 0$$

in the constant temperature case or

$$\frac{\partial \theta}{\partial n} = 0$$

in the adiabatic case. Note that in the constant temperature case, this choice of θ on the boundary would also eliminate the boundary metric variation terms in

$$\int_{\mathcal{B}} \theta \delta \left(S_{2_j} Q_j \right) d\mathcal{B}_\xi.$$

B.6 Adjoint boundary condition for the structural weight

For simplicity, it is assumed that the portion of the boundary that undergoes shape modifications is restricted to the coordinate $\xi_2 = 0$. Then equation (B.7) may be simplified by incorporating the conditions

$$n_1 = n_3 = 0, \quad n_2 = 1 \quad and \quad d\mathcal{B}_\xi = d\xi_1 d\xi_3,$$

so that only the variation δF_2 needs to be considered at the wall boundary. Moreover, the condition that there is no flow through the wall boundary at $\xi_2 = 0$ is equivalent to

$$U_2 = 0,$$

and

$$\delta U_2 = 0$$

when the boundary shape is modified. Consequently,

$$\delta F_2 = \delta p \begin{Bmatrix} 0 \\ S_{21} \\ S_{22} \\ S_{23} \\ 0 \end{Bmatrix} + p \begin{Bmatrix} 0 \\ \delta S_{21} \\ \delta S_{22} \\ \delta S_{23} \\ 0 \end{Bmatrix}. \tag{B.15}$$

Following the derivation in section 2.3, the simplified weight model can be written as

$$C_W = K_{\text{corr,b}} C_{W_b} + K_{\text{corr,s}} C_{W_s},$$

where $K_{\text{corr,b}}$ and $K_{\text{corr,s}}$ are constants,

$$C_{W_b} = \frac{-\beta}{cos(\Lambda)^2} \oint_{\mathcal{B}} p(\xi_1, \xi_3) K(\xi_3) S_{22} d\xi_1 d\xi_3,$$

and

$$C_{W_s} = \frac{1}{S\text{ref}} \oint_{\mathcal{B}} |S_{22}| d\xi_1 d\xi_3.$$

The variation of C_W is

$$\begin{aligned} \delta C_W &= -K_{\text{corr,b}} \beta \oint_{\mathcal{B}} \delta p \frac{K S_{22}}{cos(\Lambda)^2} + p\delta \left(\frac{K S_{22}}{cos(\Lambda)^2} \right) d\xi_1 d\xi_3 \\ &+ \frac{K_{\text{corr,s}}}{S\text{ref}} \oint_{\mathcal{B}} \delta |S_{22}| d\xi_1 d\xi_3 \end{aligned} \tag{B.16}$$

Since δF_2 and δC_W depend only on the pressure, it allows a complete cancellation of dependency of the boundary integral on δp, and the adjoint boundary condition reduces to

$$\psi_2 S_{21} + \psi_3 S_{22} + \psi_4 S_{23} = \frac{-\beta K_{\text{corr,b}}}{cos(\Lambda)^2} K S_{22} \tag{B.17}$$

Notice that since C_{W_s} contains no flow variables, no contribution from the area-dependent weight appears in the adjoint boundary condition.

B.7 Discretization of the adjoint equations

The adjoint differential equations for the Navier-Stokes formulation have been given by equation (B.10). To find the solution of the adjoint equations, introduce a time-like derivative term, which will vanish at the steady state solution of equation (B.10). Thus the adjoint equations (B.10) can be written as

$$\frac{\partial \psi}{\partial t} - C_i^T \frac{\partial \psi}{\partial \xi_i} + M^{-1^T} \tilde{L} \psi = 0 \quad \text{in } \mathcal{D}. \tag{B.18}$$

The main difference between (B.18) and the corresponding flow equation (2.15) is that (B.18) is a linear equation which is not in strong conservation form.

Basically, the same discretization methodology discussed in appendix A for the flow equations is used for the flux balance of the adjoint equation. For the inviscid terms in Equation (B.18), straightforward central differencing is applied with C_i^T evaluated at the cell centers. This differencing is essentially the same discretization

described in appendix A for the inviscid flux balance of the flow equations.

To evaluate the viscous adjoint fluxes, the pseudo stress tensor of the co-state variable ψ can be defined by

$$\sigma^*_{ij} = \mu \left(\frac{\partial \phi_i}{\partial x_j} + \frac{\partial \phi_j}{\partial x_i} \right) + \lambda \delta_{ij} \frac{\partial \phi_k}{\partial x_k}, \tag{B.19}$$

$$\theta^*_{ij} = \mu \left(u_i \frac{\partial \theta}{\partial x_j} + u_j \frac{\partial \theta}{\partial x_i} \right) + \lambda \delta_{ij} u_k \frac{\partial \theta}{\partial x_k}, \tag{B.20}$$

and their derivative terms are obtained in the same manner described in appendix A using the same auxiliary control volume.

Because central differencing applied to the inviscid adjoint fluxes permits odd-even decoupling, the adjoint system has been augmented with artificial dissipation just as was done for the Navier-Stokes equations. The last component of the ψ_i vector ($i = 4$ for two dimensions, for example) is used without modification for the artificial dissipation in this case. For the flow equations, the dissipation is applied to ρH instead of ρE.

B.8 Solution Methodology and Convergence Acceleration for the Viscous Adjoint Equation

The multistage Runge-Kutta time-stepping procedure described in section A.4 is reused here to solve the adjoint equations. Furthermore, the convergence acceleration techniques of section A.5 are also used here.

B.9 Discrete Adjoint Boundary Conditions

In order to make use of the summation convention, it is convenient to set $\psi_{j+1} = \phi_j$ for $j = 1, 2, 3$ and $\psi_5 = \theta$ as before.

B.10 Discrete Adjoint Wall Boundary Conditions

While the boundary conditions for the flow equations are based on physical phenomena that occurs at the boundaries, the adjoint boundary conditions are based on mathematics and depend upon the cost function used for design optimization.

For example, the adjoint wall boundary condition (B.9) has been formulated for the inverse design problem with the cost function

$$I = \frac{1}{2} \int_{\mathcal{B}} (p - p_d)^2 \, dS,$$

which is the Euclidean norm of the difference between the current pressure distribution and a desired target pressure, p_d.

This boundary condition is restated here as

$$\phi_j n_j = p - p_d, \qquad j = 1, 2, 3 \tag{B.21}$$

which means that the normal component of ϕ is equal to the difference between the current pressure and target pressure at a solid wall. the mathematics of this derivation imposes no restrictions on the tangential component of the ϕ vector. A variety of different treatments for this tangential component could be devised. A gradient accuracy study such as the one conducted in chapter 2 could be carried out for each alternative treatment and the one producing highest accuracy gradients can be selected as the preferred option. Three different types of boundary condition treatments were tried for inverse problems and the gradient accuracy studies were performed by Reuther [63]. The type described here is preferred due to its simplicity and gradient accuracy and was selected for use in this research.

First, equation (B.21) is applied to the boundary cells shown in figure B.1 for the cell centered finite-volume scheme as

$$\left(\frac{\phi_j^+ + \phi_{j+1}^-}{2} \right) n_j = p - p_d \quad j = 1, 2, 3, \tag{B.22}$$

where superscript $^+$ indicates the values in the cells right above the boundary and $^-$

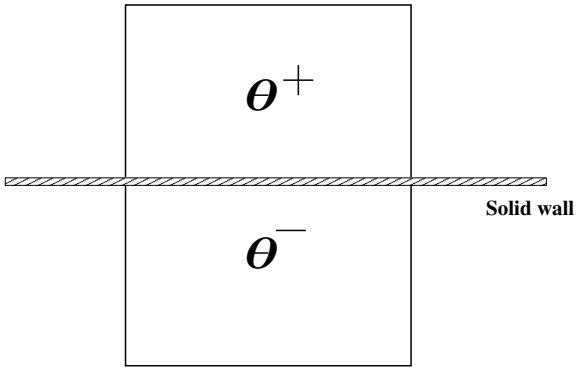

Figure B.1: Solid Boundary for the Finite-Volume Scheme

indicates the values in the halo cells right below the boundary. Additional conditions are imposed on the tangential component of ϕ

$$\phi_j^+ - \left(\phi_i^+ n_i\right) n_j = \phi_j^- - \left(\phi_i^- n_i\right) n_j \tag{B.23}$$

which represents that the tangential components of ϕ above and below the wall are the same. The following expression is obtained for ϕ from the above relations

$$\phi_j^- = \phi_j^+ + 2\left[(p - p_d) - \phi_i^+ n_i\right] n_j. \tag{B.24}$$

For the first costate variable ψ_1, the discrete boundary condition is given by

$$\psi_1^- = \psi_1^+$$

as was given for ρ of the flow equations.

For the last costate variable θ, the same relation is found as

$$\theta_1^- = \theta_1^+$$

based on the adiabatic wall boundary condition described in section B.5.

Thus, for an inverse problem, a set of discrete boundary conditions at the wall

may be summarized as

$$\begin{aligned}
&\psi_1^- = \psi_1^+, \\
&\phi_j^- = \phi_j^+ + 2\left[(p - p_d) - \phi_i^+ n_i\right] n_j, \quad j = 1, 2, 3 \\
&\theta^- = \theta^+.
\end{aligned} \tag{B.25}$$

For the force optimization cases such as the drag minimization and lift maximization, the adjoint wall boundary condition has been derived in section B.5. It is simply restated here as

$$\phi_k = c_k. \tag{B.26}$$

Unlike the boundary condition for the inverse problem, no additional constraints are necessary since we have the same number of equations as costate variables, ϕ.

Equation (B.26) can be written for the computational cells as

$$\left(\frac{\phi_k^+ + \phi_k^-}{2}\right) = c_k \tag{B.27}$$

and now the discrete wall adjoint boundary conditions are given by

$$\phi_k^- = 2c_k - \phi_k^+. \tag{B.28}$$

For force optimization problems, ψ_1 and θ are obtained in the same way as was described for the inverse problem.

B.11 Discrete Adjoint Far Field Boundary Conditions

While various choices for the discretization of the far field boundary conditions for the viscous adjoint equations are possible, in this work ψ_{1-5} were simply specified as the initial value, which is typically zero, which is equivalent to assuming that the far field boundary is very far from the geometry of interest.

Bibliography

[1] W. K. Anderson and V. Venkatakrishnan. Aerodynamic design optimization on unstructured grids with a continuous adjoint formulation. *AIAA paper 1997-643*, 35th Aerospace Sciences Meeting and Exhibit, Reno, NV, January 6-9 1997.

[2] W.K. Anderson, J.L. Thomas, and D.L. Whitfield. Multigrid acceleration of the flux split Euler equations. AIAA Paper 86-0274, AIAA 24th Aerospace Sciences Meeting, Reno, January 1986.

[3] M.D. Ardema, M.C. Chambers, A.P.Patron, A.S. Hahn, H. Miura, and M.D. Moore. Analytical fuselage and wing weight estimation of transport aircraft. NASA Technical Memorandum 110392, National Aeronautics and Space Administation, Moffett Field, CA, 1996.

[4] G. Bernardini and F. Mastroddi. Multidisciplinary design optimization for the preliminary design of aeronautical. *AIAA paper 2004-1544*, 45th AIAA/ASME/ASCE/AHS/ASC Structures, Structural Dynamics and Materials Conference, Palm Springs, California, April 2004.

[5] A. Brandt. Multi-level adaptive solutions to boundary value problems. *Math. Comp.*, 31:333–390, 1977.

[6] D.A. Caughey. A diagonal implicit multigrid algorithm for the Euler equations. AIAA Paper 87-453, 25th Aerospace Sciences Meeting, Reno, January 1987.

[7] R. Chipman and A. Jameson. Fully conservative numerical solutions for unsteady irrotational transonic flow about airfoils. AIAA Paper 79-1555, AIAA 12th Fluid and Plasma Dynamics Conference, Williamsburg, VA, July 1979.

[8] K. Deb. *Multi-Objective Optimization using Evolutionary Algorithms*. John Wiley & Sons, LTD, England, 2002.

[9] R.P. Fedorenko. The speed of convergence of one iterative process. *USSR Comp. Math. and Math. Phys.*, 4:227–235, 1964.

[10] M.B. Giles, M.C. Duta, J.D. Muller, and N.A. Pierce. Algorithm developments for discrete adjoint methods. *AIAA Journal*, 41 no.2:198–205, 2003.

[11] P.E. Gill, W. Murray, and M.H. Weight. *Practical Optimization*. Academic Press, 111 Fifth Avenue, New York, New York 10003, 1981.

[12] W. Hackbusch. On the multi-grid method applied to difference equations. *Computing*, 20:291–306, 1978.

[13] M.G. Hall. Cell vertex multigrid schemes for solution of the Euler equations. In *Proc. IMA Conference on Numerical Methods for Fluid Dynamics*, Reading, April 1985.

[14] P.W. Hemker and S.P. Spekreijse. Multigrid solution of the steady Euler equations. In *Proc. Oberwolfach Meeting on Multigrid Methods*, December 1984.

[15] M.G. Hutchison, E.R. Unger, W.H. Mason, B. Grossman, and R.T. Haftka. Variable-complexity aerodynamic optimization of an hsct wing using structural wing-weight equations. *AIAA paper 1992-0212*, 30th Aerospace Sciences Meeting and Exhibit, Reno, Nevada, January 6-9 1992.

[16] A. Jameson. Solution of the Euler equations by a multigrid method. *Appl. Math. and Comp.*, 13:327–356, 1983.

[17] A. Jameson. Multigrid algorithms for compressible flow calculations. In *Second European Conference on Multigrid Methods*, Cologne, October 1985. Princeton University Report MAE 1743.

[18] A. Jameson. Transonic flow calculations for aircraft. In F. Brezzi, editor, *Lecture Notes in Mathematics, Numerical Methods in Fluid Dynamics*, pages 156–242. Springer Verlag, 1985.

[19] A. Jameson. A vertex based multigrid algorithm for three-dimensional compressible flow calculations. In T.E. Tezduar and T.J.R. Hughes, editors, *Numerical Methods for Compressible Flow - Finite Difference, Element And Volume Techniques*, 1986. ASME Publication AMD 78.

[20] A. Jameson. Aerodynamic design via control theory. *Journal of Scientific Computing*, 3:233–260, 1988.

[21] A. Jameson. Automatic design of transonic airfoils to reduce the shock induced pressure drag. In *Proceedings of the 31st Israel Annual Conference on Aviation and Aeronautics, Tel Aviv*, pages 5–17, February 1990.

[22] A. Jameson. Computational algorithms for aerodynamic analysis and design. Technical report, INRIA 25th Anniversary Conference on Computer Science and Control, France, December 1992. To appear in *Applied Numerical Methods*.

[23] A. Jameson. Analysis and design of numerical schemes for gas dynamics 1, artificial diffusion, upwind biasing, limiters and their effect on multigrid convergence. *Int. J. of Comp. Fluid Dyn.*, 4:171–218, 1995.

[24] A. Jameson. Analysis and design of numerical schemes for gas dynamics 2, artificial diffusion and discrete shock structure. *Int. J. of Comp. Fluid Dyn.*, 5:1–38, 1995.

[25] A. Jameson. Optimum aerodynamic design using control theory. *Computational Fluid Dynamics Review*, pages 495–528, 1995.

[26] A. Jameson. A perspective on computational algorithms for aerodynamic analysis and design. *Progress in Aerospace Sciences*, 37:197–243, 2001.

[27] A. Jameson. Aerodynamic shape optimization using the adjoint method. 2002-2003 lecture series at the von karman institute, Von Karman Institute For Fluid Dynamics, Brussels, Belgium, Febuary 3-7 2003.

[28] A. Jameson and T.J. Baker. Solution of the Euler equations for complex configurations. *AIAA paper 83-1929*, AIAA 6th Computational Fluid Dynamics Conference, Danvers, MA, July 1983.

[29] A. Jameson, T.J. Baker, and N.P. Weatherill. Calculation of inviscid transonic flow over a complete aircraft. *AIAA paper 86-0103*, AIAA 24th Aerospace Sciences Meeting, Reno, Nevada, January 1986.

[30] A. Jameson and L. Martinelli. Aerodynamic shape optimization techniques based on control theory. Technical report, CIME (International Mathematical Summer Center), Martina Franca, Italy, 1999.

[31] A. Jameson, L. Martinelli, and N. A. Pierce. Optimum aerodynamic design using the Navier-Stokes equations. *Theoretical and Computational Fluid Dynamics*, 10:213–237, 1998.

[32] A. Jameson and D.J. Mavriplis. Multigrid solution of the Euler equations on unstructured and adaptive grids. In S. McCormick, editor, *Multigrid Methods, Theory, Applications and Supercomputing. Lecture Notes in Pure and Applied Mathematics*, volume 110, pages 413–430, April 1987.

[33] A. Jameson, W. Schmidt, and E. Turkel. Numerical solution of the Euler equations by finite volume methods using Runge-Kutta time stepping schemes. AIAA Paper 81-1259, 1981.

[34] A. Jameson and J. C. Vassberg. Studies of alternative numerical optimization methods applied to the brachistochrone problem. *Computational Fluid Dynamics Journal*, 9:281–296, 2000.

[35] S. Kim. *Design Optimization of High-Lift Configurations Using a Viscous Adjoint-Based Method. PhD Dissertation*, Stanford University, Stanford, CA, December 2001.

[36] S. Kim, J. J. Alonso, and A. Jameson. A gradient accuracy study for the adjoint-based navier-stokes design method. *AIAA paper 99-0299*, AIAA 37th Aerospace Sciences Meeting & Exhibit, Reno, NV, January 1999.

[37] I. Kroo. Aircraft design: Synthesis and analysis. http://adg.stanford.edu/aa241/AircraftDesign.html, January 2003.

[38] I.M. Kroo. Design and analysis of optimally-loaded lifting systems. *AIAA paper 1984-2507*, October 1984.

[39] M.H. Lallemand and A. Dervieux. A multigrid finite-element method for solving the two-dimensional Euler equations. In S.F. McCormick, editor, *Proceedings of the Third Copper Mountain Conference on Multigrid Methods, Lecture Notes in Pure and Applied Mathematics*, pages 337–363, Copper Mountain, April 1987.

[40] B. Van Leer. Towards the ultimate conservative difference scheme. II. Monotonicity and conservation combined in a second order scheme. *J. Comp. Phys.*, 14:361–370, 1974.

[41] K. Leoviriyakit and A. Jameson. Aero-structural wing planform optimization. *AIAA paper 2004-0029*, 42nd Aerospace Sciences Meeting & Exhibit, Reno, Nevada, January 2004.

[42] K. Leoviriyakit, S. Kim, and A. Jameson. Aero-structural wing planform optimization using the Navier-Stokes equations. *AIAA paper 2004-4479*, 10th AIAA/ISSMO Multidisciplinary Analysis and Optimization Conference, Albany, New York, August 30 - September 1 2004.

[43] R.H. Liebeck. Design of the blended-wing-body subsonic transport. *Journal of Aircraft*, 41 no.1:10–25, 2004. 0021-8669.

[44] M-S. Liou and C.J. Steffen. A new flux splitting scheme. *J. Comp. Phys.*, 107:23–39, 1993.

[45] E. Lund. *Finite Element Based Design Sensitivity Analysis and Optimization. PhD Dissertation*, Aalborg University, Denmark, 1994.

[46] F.T. Lynch. Transonic aerodynamics. volume 81 of *Progress in Astronautics and aeronautics*, chapter Commercial Transports - Aerodynamic Design for Cruise

Performance Efficiency, pages 81–144. AIAA, New York, 1982. (edited by D. Nixon).

[47] L. Martinelli. Calculations of viscous flows with a multigrid method. *Princeton University Thesis*, May 1987.

[48] L. Martinelli and A. Jameson. Validation of a multigrid method for the Reynolds averaged equations. *AIAA paper 88-0414*, 1988.

[49] J. R. R. A. Martins. *A Coupled-Adjoint Method for High-Fidelity Aero-Strucural Optimization. PhD Dissertation*, Stanford University, Stanford, CA, October 2002.

[50] K. Maute, M. Nikbay, and C. Farhat. Conceptual layout of aeroelastic wing structures by topology optimization. *AIAA paper 2002-1480*, AIAA Paper 2002-1480, 43rd AIAA/ASME/ASCE/AHS/ASC, 2002.

[51] T. McGeer. *Wing Design For Minimum Drag with Practical Constraints. PhD Dissertation*, Stanford University, Stanford, CA, December 1983.

[52] T. McGeer and R.S. Shevell. A method for estimating the compressibility drag of an airplane. *SUDAAR*, 535, 1983.

[53] M. Nemec and D. W. Zingg. Towards efficient aerodynamic shape optimization based on the navier-stokes equations. *AIAA paper 2001-2532*, 15th AIAA Computational Fluid Dynamics Conference, Anaheim, CA, June 11-14 2001.

[54] R.H. Ni. A multiple grid scheme for solving the Euler equations. *AIAA Journal*, 20:1565–1571, 1982.

[55] L.M. Nicolai. *Fundamentals of Aircraft Design*. METS Inc., University of Dayton, Dayton, Ohio, 1976.

[56] M. C.Y. Niu. *Airframe Stress Analysis and Sizing*. Hong Kong Conmilit Press Ltd., England, 1999. ISBN: 9627128082.

[57] P. Piperni, M. Abdo, and F. Fafyeke. The application of multi-disciplinary optimization technologies to the design of a business jet. *AIAA paper 2004-4370*, 10th AIAA/ISSMO Multidisciplinary Analysis and Optimization Conference, Albany, New York, August 30 - September 1 2004.

[58] O. Pironneau. *Optimal Shape Design for Elliptic Systems*. Springer-Verlag, New York, 1984.

[59] L. Prandtl. Aerofoil lift and drag in theory. *Jb. Wiss. Ges. Luftfahrt*, V, 1920.

[60] L. Prandtl and O.G. Tietjens. *Applied Hydro- and Aeromechanics*. Dover Publications, Inc., New York, 1971. Translated by J.P. Den Hartog.

[61] Daniel P. Raymer. *Aircraft Design: A Conceptual Approach, Third Edition*. AIAA Education Series, Wright-Patterson Air Force Base, Ohio, 1990.

[62] J. Reuther and A. Jameson. Aerodynamic shape optimization of wing and wing-body configurations using control theory. *AIAA paper 95-0213*, 33rd Aerospace Sciences Meeting and Exibit, Reno, Nevada, January 1995.

[63] J.J. Reuther. *Aerodynamic Shape Optimization Using Control Theory. PhD Dissertation*, University of California Davis, Davis, CA, 1996.

[64] A. Rizzi and L.E. Eriksson. Computation of flow around wings based on the Euler equations. *J. Fluid Mech.*, 148:45–71, 1984.

[65] P.L. Roe. Fluctuations and signals - a framework for numerical evolution prolems. In K.W. Morton and M.J. Baines, editors, *Proceedings of IMA Conference on Numerical Methods in Fluid Dynamics*, pages 219–257, Reading, 1981.

[66] Sriram. *Numerical analysis and design of upwind sails. PhD Dissertation*, Stanford University, Stanford, CA, December 2002.

[67] K. Szema, Z. Liu, S. Ramakrishnan, and C. Rowell. Automated unstructured-grid cfd tool for aerodynamic design optimization of airfoils and wings. *AIAA paper 2005-452*, AIAA 43rd Aerospace Sciences Meeting, Reno, Nevada, January 2005.

[68] S. Tatsumi, L. Martinelli, and A. Jameson. Design, implementation, and validation of flux limited schemes for the solution of the compressible Navier-Stokes equations. *AIAA paper 94-0647*, AIAA 32nd Aerospace Sciences Meeting, Reno, Nevada, January 1994.

[69] S. Tatsumi, L. Martinelli, and A. Jameson. A new high resolution scheme for compressible viscous flows with shocks. *AIAA paper 95-0466*, AIAA 33nd Aerospace Sciences Meeting, Reno, Nevada, January 1995.

[70] E. Torenbeek. *Synthesis of subsonic airplane design.* Delft University Press, 1977. with a foreword by H. Wittenberg.

[71] Y. Wada and M-S. Liou. A flux splitting scheme with high-resolution and robustness for discontinuities. *AIAA paper 94-0083*, AIAA 32nd Aerospace Sciences Meeting, Reno, Nevada, January 1994.

[72] S. Wakayama. Blended-wing-body optimization problem setup. *AIAA paper 2000-4740*, 8th AIAA/USAF/NASA/ISSMO Symposium on Multidisciplinary Analysis and Optimization, Long Beach, CA, September 2000.

[73] S.R. Wakayama. *Lifting Surface Design Using Multidisciplinary Optimization. PhD Dissertation*, Stanford University, Stanford, CA, December 1994.

[74] S.R. Wakayama and I.M. Kroo. A method for lifting surface design using nonlinear optimization. Dayton, OH, Sept. 1990. AIAA Paper 90-3120. AIAA/AHS/ASEE Aircraft Design Systems and Operations Conference.

[75] R.T. Whitcomb. Review of NASA supercritical airfoils. ICAS 74-10, NASA, 1974.

[76] R.T. Whitcomb. Transonic airfoil development. AGARD-R 712, 1983.